FACULDADE DE ENGENHARIA DA UNIVERSIDADE DO PORTO

Machine vision processing of deep space images

João Francisco Sengo Guimarães

Mestrado em Engenharia Eletrotécnica e de Computadores

Supervisor: Prof. Paulo Jorge Valente Garcia

Co-Supervisor: Prof. Andry Maykol Gomes Pinto

June 30, 2023

Resumo

A engenharia espacial concentra-se no projeto, construção e operação de foguetões e satélites e outras tecnologias usadas no espaço , abrangendo uma ampla gama de disciplinas, incluindo a engenharia electroténica e de computadores. As imagens espaciais desempenham um papel crucial na engenharia espacial, e a busca de observações da mais alta qualidade é de suma importância. Ao capturar e analisar imagens de objetos e fenómenos celestes, os engenheiros podem calcular a atitude dos satélites com star trackers, monitorizar as órbitas dos satélites a partir do solo, estudar o lixo espacial e obter informações sobre objetos celestes. A mais alta qualidade de observação garante que os dados coletados sejam exatos, precisos e confiáveis, permitindo que os engenheiros tomem decisões informadas ao projetar e operar sistemas e tecnologias baseados no espaço. O conhecimento preciso de objetos astronômicos, suas posições, composições e movimentos permite navegação, posicionamento de espaçonaves e comunicação mais precisos, minimizando riscos e maximizando o sucesso da missão.

No contexto dos telescópios terrestres, a aquisição de imagens do espaço profundo apresenta desafios substanciais devido aos efeitos induzidos pela atmosfera da Terra. Esses efeitos manifestam-se como distorções, aberrações e fenómenos de cintilação. Esta dissertação visa investigar e comparar abordagens inovadoras utilizando técnicas de visão computacional para mitigar esses problemas sistemáticos de forma eficaz. O documento começa com uma introdução sucinta, fornecendo uma visão geral do problema em questão, os objetivos subjacentes e a organização estrutural do documento. Em seguida, uma exploração abrangente de várias técnicas é realizada para abordar diversas dificuldades que podem surgir ao considerar cenários de telescópio único e multi-telescópio, culminando na criação de uma imagem mestre. Além disso, é apresentada uma análise meticulosa do instrumento de imagem empregado na aquisição do conjunto de dados para esta dissertação, juntamente com um exame abrangente dos distintos efeitos sistemáticos que afetam o conjunto de dados. Posteriormente, quatro metodologias distintas são empregadas para fundir várias imagens adquiridas por um único telescópio, reduzindo efetivamente os efeitos atmosféricos e gerando uma imagem com maior precisão a realidade. Além disso, é investigada a fusão de imagens obtidas dos quatro telescópios que compõem o sistema GRAVITY, com o objetivo de produzir uma imagem mestre que se aproxime da realidade observada. Finalmente, é realizada uma análise dos resultados obtidos com base nessas técnicas, facilitando uma avaliação robusta da sua eficácia e implicações.

Abstract

Space engineering focuses on the design, construction, and operation of spacecraft and other technology used in outer space, comprising a wide range of disciplines, including electrical engineering. Space imagery plays a crucial role in space engineering, and the pursuit of the highest quality observations is of paramount importance. By capturing and analysing images of celestial objects and phenomena, engineers can compute satellite atitude with star trackers, monitor the orbits of satellites from the ground, study space debris as well as obtain information on celestial objects. The highest quality of observation ensures that the data collected is accurate, precise, and reliable, enabling engineers to make informed decisions in designing and operating space-based systems and technologies. Precise knowledge of astronomical objects, their positions, compositions, and movements allows for more accurate navigation, spacecraft positioning, and communication, minimising risks and maximising mission success.

In the context of ground-based telescopes, the acquisition of images of deep space presents substantial challenges owing to the systematic effects induced by the Earth's atmosphere. These effects manifest as distortions, blurring, and the twinkling phenomenon encountered during celestial observations. The present dissertation aims to investigate and compare innovative approaches utilising computer vision techniques to mitigate these systematic issues effectively. The document commences with a succinct introduction, providing an overview of the problem at hand, the underlying objectives, and the structural organisation of the document. Following this, a comprehensive exploration of various techniques is undertaken to address diverse complications that may arise when considering both single-telescope and multi-telescope scenarios, culminating in the creation of a master image. Furthermore, a meticulous analysis of the imaging instrument employed in acquiring the dataset for this dissertation is presented, along with a comprehensive examination of the distinct systematic effects impacting the dataset. Subsequently, four distinct methodologies are employed to fuse multiple frames acquired by a single telescope, effectively nullifying atmospheric effects and generating an image that accurately represents reality. Furthermore, the fusion of images obtained from the four telescopes comprising the GRAVITY system is investigated, aiming to produce a master image approximating the observed reality. Finally, a comprehensive analysis of the obtained results based on these techniques is conducted, facilitating a robust evaluation of their effectiveness and implications.

Agradecimentos

Após aproximadamente 17 longos anos de estudo, dou por completo o meu percurso académico com esta dissertação, pelo que fico grato a todos aqueles que fizeram parte do meu percurso.

Para começar, quero agradecer à FEUP, onde tenho muito orgulho de ter estudado. Esta instituição foi sem dúvida onde mais desenvolvi o meu conhecimento, tendo-me proporcionado muitos momentos de felicidade (e 'stress'), onde pude realizar sonhos que tinha desde pequeno, como me tornar engenheiro Electrotécnico e de Computadores e a realização de ERASMUS, a qual deve ter sido das melhores experiências da minha vida. Além disso, gostava de agradecer às Senhoras do bar da biblioteca, pela sua gentileza e simpatia ao longo da minha estadia nesta faculdade.

A seguir, quero dar um agradecimento especial aos meus orientadores. Primeiramente, o Prof. Dr. Paulo Garcia, o qual me acompanhou ao longo do desenvolvimento desta dissertação, tendo os meus melhores interesses em consideração e por estar sempre disponível para discutir ideias, criticar os meus resultados e ajudar a orientar o curso deste trabalho. De seguida, gostava de estender a minha gratidão ao Prof. Dr. Andry Pinto, que para além de me ter acompanhado nesta dissertação, foi um professor muito presente no meu percurso nesta faculdade.

Um obrigado a todos os meus amigos, com um carinho especial para a FakeFeup, Guilherme, Pita e Costa, que me aturaram nos meus momentos mais stressantes e estiveram presentes nos meus momentos mais felizes. Certamente serão amigos que levarei para o resto da minha vida com muito carinho e gratidão.

Por fim, mas não menos importante, também gostava de agradecer à minha família, desde os meus tios, primos e avós, dedicando todo o meu trabalho aos meus pais, que sempre quiseram o melhor de mim e que fosse feliz, fazendo de tudo para que eu pudesse alcançar esse objetivo. Sem vocês não estaria nesta posição.

Francisco Sengo

“I love those who can smile in trouble, who can gather strength from distress, and grow brave by reflection.
’Tis the business of little minds to shrink, but they whose heart is firm, and whose conscience approves their conduct, will pursue their principles unto death.”

Leonardo da Vinci

Contents

List of Figures

List of Tables

Abbreviations

AO	Adaptive Optics
CCD	Charge-Coupled Device
CMOS	Complementary Metal–Oxide–Semiconductors
CNN	Convolutional Neural Network
DFT	Discrete Fourier Transform
DLT	Direct Linear Transform
DM	Deformable Mirror
DoG	Difference of Gaussians
ESO	European Southern Observatory
FITS	Flexible Image Transport System
FWHM	Full-Width at Half-Maximum
HDoG	Higher Order Laplacian of Gaussian
HLoG	Higher Order Laplacian of Gaussian
HR	High Resolution
HST	Hubble Space Telescope
LF	Lucky Fourier
LGS	Laser Guide Star
LI	Lucky Imaging
LM	Levenberg-Marquardt
LoG	Laplacian of Gaussian
LR	Low Resolution
MFSR	Multi-Frame Super-Resolution
MSE	Mean Squared Error
NGS	Natural Guide Star
NN	Neural Network
ORB	Oriented Fast and Rotated BRIEF
PSF	Point Spread Function
PSNR	Peak Signal to Noise Ratio
RMSE	Root Mean Squared Error
Sgr A*	Sagittarius A*
SIFT	Scale-Invariant Feature Transform
STScI	Space Telescope Science Institute
VLTI	Very Large Telescope Interferometer
WFS	Wavefront Sensing

Chapter 1

Introduction

1.1 Context

Deep space images are important in space engineering for a variety of reasons. First and foremost, they provide valuable information about the objects and phenomena being observed, which can help engineers design and build better spacecraft and other technology for exploring and studying these objects. For example, images of distant planets and asteroids can help engineers to understand the surface conditions and other characteristics of these objects, which can inform the design of landers and other spacecraft that will be used to explore them. Deep space images can also provide valuable data about the structure and behaviour of celestial objects, such as stars and galaxies, which can help engineers to develop new technologies for studying and observing these objects. Additionally, deep space images can be used to test and validate the performance of existing spacecraft and other space-based technology and can help engineers to identify and troubleshoot any issues that may arise.

The telescope, an instrument that dates back to the 17th century, has been the most important piece of equipment in space exploration since Galileo Galilei (1564-1642) made his first observation of celestial bodies, allowing him to study and depict what he saw. Since then, a wide variety of equipment and techniques have been developed that can detect various portions of the electromagnetic spectrum. A telescope is the first element in any space imaging system, collecting and focusing light, producing images which allow us to look further into deep space. Techniques have been developed to improve the quality of the observations in order to give the scientists who examine these images better data. These images contain a number of systematic effects that prevent a straightforward approach of simply stacking these images together to create a final image.

This dissertation aims to develop novel approaches to deal with systematics using machine vision techniques.

1.2 Statement of the problem

Compared to space-based telescopes, a ground-based instrument like GRAVITY is much less expensive and simpler to maintain. However, because the telescope must see through the Earth's atmosphere, there are some drawbacks. The atmosphere, a layer of gases that surrounds certain planets, shields humanity from harmful radiation by absorbing part of the electromagnetic spectrum. Although beneficial to humans, some of the wavelengths are blocked, degrading images captured by ground-based telescopes. Due to time-variable optical distortions, the data acquired by this type of telescope is faulty. Therefore, all celestial objects appear to blur and change position over time. As was previously mentioned, in order to provide better data to the scientists that study these images, methods have been devised to enhance the quality of the observations, but they prove to be a labour-intensive procedure that needs both human resources and a variety of tools to provide effective results. Based on what was previously stated, this dissertation suggests processing these images using machine vision techniques, with the aim to try and produce a master image that has improved quality, counteracting the preceding effects described.

1.3 Objectives

This dissertation aims to use machine vision techniques and other methods to create a novel approach to producing a master image from the observations made by GRAVITY. Therefore this project has the following goals:

1. Identify the systematic effects of the atmosphere and other artefacts on the images acquired by GRAVITY.
2. Analysis of techniques for both the single-telescope and multi-telescope image stitching challenges.
3. Compare machine vision-based approaches to stitch the different images into a master image.
4. Evaluation of the quality and performance of the proposed methods.

1.4 Structure of this Document

There are six chapters in this document. The first chapter is the current introduction, which provided a context and definition of the problem, as well as the main goals of this work. Chapter 2 contains an analysis of some state-of-the-art methods to problems that may arise when finding a solution to combining both the frames from a single telescope and the final images from the telescopes into a master image. In Chapter 3 contains a review of the instrumentation used to acquire the data. Additionally, an acquisition of different features of both stars and frames is performed in order to provide an analysis on the atmospheric effects on the dataset used in this dissertation. In

Chapter 4, the methodology used for techniques chosen to combine the different frames from an individual telescope into one single image is described, as well as a traditional image stitching algorithm to combine the different images from the telescope into a final image. In Chapter 5 of this document, a comprehensive assessment is conducted on the generated images obtained through the multi-frame super-resolution techniques, alongside the master image derived from the conventional image stitching algorithm, for each of the aforementioned methods. Finally, Chapter 6 contains the final conclusions about the results obtained through the performed study, in addition to listing future work and possible modifications to the methodologies chosen.

Chapter 2

State of the Art

This chapter of the dissertation aims to address the challenges involved in developing a novel approach for producing a master image from observations affected by atmospheric effects. The research explores potential solutions to overcome these challenges by employing machine vision techniques and other methodologies. The analysis encompasses various aspects, including the investigation of super-resolution techniques for multi-frame super-resolution and image stitching techniques applicable to both single and multi-telescope image stitching. Additionally, it delves into the integration of machine learning-based solutions. As will be clear later, machine learning solutions were not addressed as we can obtain very good results with classical approaches. However, from a state-of-the-art survey perspective, it is addressed and along the present chapter. By thoroughly exploring these avenues, the dissertation strives to establish a robust framework for effectively generating high-quality master images from observations under the influence of atmospheric effects.

2.1 Image Stitching Techniques

Image stitching plays a vital role in various applications in machine vision due to its inherent advantages. One of the key benefits is its ability to combine images acquired from different sensors or modalities. By fusing information from multiple sources, such as visible and infrared imagery or multi-spectral data, image fusion enables the creation of a unified representation that encompasses a broader range of information [1]. This capability finds applications in fields like remote sensing, medical imaging, robotics and space images, where the fusion of complementary data sources enhances visual information's accuracy, reliability, and interpretability.

2.1.1 Overview of Feature Detection

Feature detection is a fundamental task in machine vision aimed at identifying distinctive patterns or structures in an image that can be used for various applications such as object recognition, tracking, and matching. Overall, feature detection techniques such as Laplacian of Gaussian (LoG), Difference of Gaussians (DoG), Scale-Invariant Feature Transform (SIFT), and Oriented

Fast and Rotated BRIEF (ORB) play a critical role in identifying and analysing blob features, such as star features in space images, allowing space engineers and researchers to detect and track stars automatically.

The Laplacian of Gaussian method [2] is based on the second derivative of the Gaussian function, which measures the curvature of a function. The process starts by convolving the image with a Gaussian filter, resulting in a smoothed version of the image. Next, the Laplacian operator is applied to the smoothed image to detect the edges of the blobs. The Laplacian of Gaussian method is robust to noise and can detect different sizes of blobs. However, its main drawback is its computational expense due to the Gaussian convolution.

The Gaussian function used in this technique is defined as [2]:

$$G(x,y;\sigma) = \frac{1}{\sqrt{2\pi\sigma^2}} \exp\left(-\frac{x^2+y^2}{2\sigma^2}\right) \tag{2.1}$$

where σ represents the standard deviation. The Gaussian scale-space representation $L(x,y;\sigma)$ of an image $f(x,y)$ is obtained by convolving the image with the Gaussian function [2, 3]:

$$L(x,y;\sigma) = f(x,y) * G(x,y;\sigma) \tag{2.2}$$

The Laplacian operator, denoted as ∇^2, is then applied to the Gaussian scale-space representation, or equivalently, the LoG operator is computed first and then convolved with the image to create the LoG scale-space representation [2]:

$$\nabla^2 \mathrm{G}(x,y) = \frac{x^2+y^2-2\sigma^2}{\pi\sigma^4} \exp\left(-\frac{x^2+y^2}{2\sigma^2}\right) \tag{2.3}$$

The Gaussian smoothing aims to reduce noise, while the Laplacian operator highlights regions of rapid intensity change, making it suitable for edge detection. As the scale σ of the LoG increases, blob-like structures converge to local extrema at a specific scale, making the LoG filter an excellent option for blob detection [2].

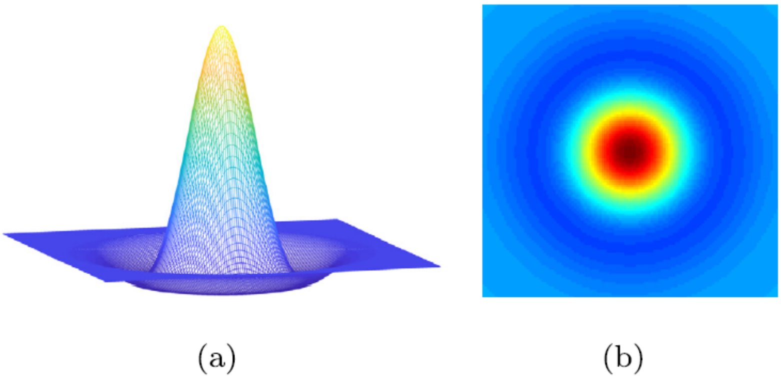
(a) (b)

Figure 2.1: Illustration of a second-order Gaussian kernel. (a) Three-dimensional visualisation; (b) Planar visualization. From [4].

On the other hand, the Difference of Gaussians method is based on the difference between two Gaussian functions of different scales. This method is faster than the LoG approach and can also detect blobs of various sizes [2]. The DoG method involves subtracting the image convolved with a Gaussian kernel of a smaller scale from the image convolved with a Gaussian kernel of a larger scale. The resulting image highlights the blobs whose sizes fall within the range of the two scales used. However, the DoG method may miss small blobs and is sensitive to the selection of scales [2, 3].

The DoG method produces the scale space by convolving the image with Gaussian kernels of different standard deviations (σ). The difference in Gaussian images (DoG) is then obtained by subtracting the convolved images at different scales. The DoG function is defined as:

$$D(x,y,\sigma) = (G(x,y,k\sigma) - G(x,y,\sigma)) * I(x,y) = L(x,y,k\sigma) - L(x,y,\sigma) \tag{2.4}$$

where k represents the scale factor. The DoG feature detector identifies local extrema in the DoG images, which serve as potential blob centres. The scale and shape factors at each centre are determined by comparing the responses of neighbouring pixels. Thresholding techniques are commonly applied to reduce false positives and improve the accuracy of blob detection [2, 3].

Both the LoG and DoG methods have been widely utilised for blob detection in various applications, particularly for objects with characteristic scales, such as cells in biological images or stars in space images. The choice between the two methods depends on the application's specific requirements, considering factors like accuracy and computational efficiency.

Cho et al. [5] presents a novel method for keypoint detection called Higher Order Laplacian of Gaussian (HLoG). The HLoG approach exhibits superior performance to the conventional DoG technique, particularly in image retrieval. The development of Higher Order Difference of Gaussians (HDoG) stemmed from the observation that DoG solely utilises the first-order derivative of the scale-space (G) with respect to scale (σ). In contrast, HDoG harnesses the power of higher-order scale-space derivatives. By disregarding the leading coefficient of the Gaussian equation given in Equation 2.1, the author of the paper compares the similarities of the second, third, and fourth derivatives with respect to σ in relation to the derivatives with respect to x and y up to the 8^{th} degree for even orders, respectively. This allows the author to establish the relationships between the higher-order scale-space derivatives and the spatial derivatives as such [5]:

$$\frac{\partial^2 G}{\partial \sigma^2} \approx \sigma^2 \nabla^4 G \tag{2.5}$$

$$\frac{\partial^3 G}{\partial \sigma^3} \approx \sigma^3 \nabla^6 G \tag{2.6}$$

$$\frac{\partial^4 G}{\partial \sigma^4} \approx \sigma^4 \nabla^8 G \tag{2.7}$$

These equations demonstrate that the σ-normalised HLoG approximates the Higher Order Difference of Gaussians (HDoG) in the same way that Difference of Gaussians approximates the

Laplacian of Gaussian, as it is well established in [5]:

$$\partial G/\partial \sigma \approx \sigma \nabla^2 G \tag{2.8}$$

It is worth noting that the effectiveness of HDoG has already been experimentally validated, which provides further confidence in the potential of HLoG for keypoint detection. One advantage of the HLoG method is its ability to capture high-frequency signals more effectively as the order increases. The filters employed in HLoG become more intricate, enabling better detection of complex shapes and patterns. In contrast, HDoG suffers from a drawback in parallel processing due to the sequential inter-scale subtraction operations required to obtain higher-order DoG spaces. However, with HLoG, the filter kernels can be prepared and applied to the input image in parallel. Consequently, higher-order HLoG spaces simultaneously can be obtained, significantly enhancing the parallel processing capability. This parallel processing advantage sets HLoG apart from HDoG and facilitates efficient and scalable keypoint detection in various applications.

In addition to the aforementioned methods, there exist other popular feature detection techniques that are extensively employed in the field of machine vision. Among these methods, the Scale Invariant Feature Transform (SIFT), Oriented FAST, and Rotated BRIEF (ORB) stand out as widely recognised approaches for keypoint detection and descriptor construction. Over the years, SIFT has established itself as a prominent technique, while ORB offers a compelling alternative with its faster processing speed and comparable performance.

SIFT, proposed by David Lowe in 1999 [6], employs a scale-space representation and the DoG operator for keypoint detection. The DoG pyramid detects local extrema, which are considered as potential key points. The extrema are further refined using a 3D quadratic function to approximate the interpolated locations. To eliminate key points with strong edge responses and ensure sub-pixel localisation, SIFT employs a measurement function computed from the trace and determinant of the Hessian matrix [7]. The key points detected by SIFT are characterised by their descriptors, which encode information about the local gradient orientation and magnitude around each key point. These descriptors enable image comparison based on the number of similar key points between images, thus determining their similarity. The SIFT algorithm consists of four stages: scale-space extrema detection, keypoint localisation, orientation assignment, and keypoint descriptor computation. The extrema detection involves constructing an image pyramid using Gaussian convolutions and subtracting adjacent Gaussian images to create a DoG pyramid. The key points are then identified as local maxima and minima in the DoG pyramid by comparing pixels to their neighbours at multiple scales. Orientation assignment assigns one or more orientations to each key point based on local gradient directions. Finally, the descriptors are computed by calculating gradient magnitudes and orientations at sample points around the keypoint areas [8, 5].

Although deep learning-based methods are gaining popularity, traditional methods like SIFT remain relevant and important to study [5]. SIFT has demonstrated its effectiveness in various applications, including image stitching, where it is considered the most widely used feature descriptor. The robustness of SIFT to lighting and viewpoint changes makes it reliable for feature extraction, and its feature matching capabilities contribute to its wide adoption [9, 8].

On the other hand, ORB [9] is a feature extraction technique developed in OpenCV. It utilises the FAST keypoint detector and binary BRIEF descriptor. Compared to SIFT, ORB exhibits faster computation and is less sensitive to noise while still providing good feature extraction results. ORB first applies the FAST keypoint detector to identify a large number of key points and then employs a Harris corner detector to select high-quality features among those key points. The centroid of the image can be calculated using the patch moment in ORB, and the orientation of corners is determined using the intensity centroid of image patches.

Convolutional Neural Networks

In recent years, deep learning techniques have revolutionised the field of machine vision, enabling unprecedented performance in tasks such as object detection, image classification, and segmentation. Among the various deep learning architectures, Convolutional Neural Networks (CNN) have emerged as the state-of-the-art for feature detection and extraction in images.

Neural Networks (NN) mimic the signals between neurons to simulate how a human brain works. These neurons consist of input data, weights and a bias in order to calculate an output. These outputs are then fed to another layer, where they serve as inputs for the next set of neurons. The outputs described above are calculated through the use of activation functions, which add a non-linear component to the neural network. This method requires training data to learn and improve their accuracy over time. Since the objective of the training stage aims to minimise a loss function, a method called back-propagation aims to fine-tune the weights of the neural network, taking into account the error rate obtained in the precious epoch [10].

Unlike traditional NNs, which operate on fully connected layers, CNNs employ a hierarchical approach that mimics the organization of the human visual cortex. By using convolutional and pooling layers, CNNs are able to learn increasingly complex representations of the input data while also reducing the dimensionality of the feature maps. This makes CNNs particularly effective for tasks where local features and spatial relationships are important, such as image classification and object detection.

CNNs are usually composed by three types of layers [10, 11]:

Convolutional Layers: where a CNN uses different kernels to convolve both the final feature maps and the entire image, producing different feature maps.

Pooling Layers: are responsible for reducing the input spatial dimensions for the following convolutional layer. In this layer, the operation performed can also be called subsampling or downsampling, which causes a loss of information. However, this loss is advantageous for the network since it reduces the computational burden on the incoming layers of the network and prevents overfitting. The most often employed techniques are average pooling and maximum pooling.

Fully Connected Layers: These layers are used in the neural network's high-level reasoning after numerous convolutional and pooling layers. The 2D feature maps are subsequently transformed into a 1D feature vector, where the generated vector could be used as a feature vector for additional processing or placed into a set of categories for classification.

Loss Function: The output layer, which is the last layer of the CNN model, uses a few loss functions to determine the predicted error produced over the training samples. The discrepancy between the actual output and the projected one is shown by this error. It will then be improved using CNN's learning method.

Stitching images directly using deep learning is very difficult because it integrates the tasks of feature detection, feature matching, homography estimation, image registration, and image stitching into CNNs. Consequently, a pre-trained homography estimation network is crucial to liberate CNNs from difficult tasks [12].

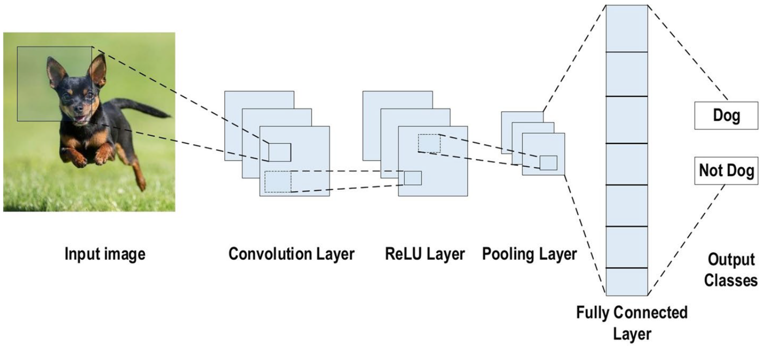

Figure 2.2: An example of CNN architecture for image classification. From [13].

2.1.2 Homography Estimation

Homography estimation is a technique used in image processing and machine vision to estimate the transformation between two images that are related by a perspective transformation. A perspective transformation, commonly referred to as homography, keeps the image's straight lines while shifting the objects' relative locations. It may be used to register or align two pictures, such as registering an image taken at a different time or from a different perspective with a reference image to identify changes. Additionally, it may be used to change an image's coordinate system or rectify distortion.

The Direct Linear Transform (DLT) [14] algorithm lies at the core of homography estimation and is widely recognised as the most commonly used approach for this purpose. It is a straightforward and computationally efficient method that operates by solving a system of linear equations. In the context of working with homogeneous coordinates, the relationship between two corresponding points x and x0 can be expressed as follows [14]:

$$c\begin{pmatrix} u \\ v \\ 1 \end{pmatrix} = H\begin{pmatrix} x \\ y \\ 1 \end{pmatrix} \tag{2.9}$$

In equation 2.9, c represents any non-zero constant, $\begin{pmatrix} u & v & 1 \end{pmatrix}^T$ denotes $\mathbf{x}'$, $\begin{pmatrix} x & y & 1 \end{pmatrix}^T$ denotes $\mathbf{x}$, and $H = \begin{pmatrix} h_1 & h_2 & h_3 \\ h_4 & h_5 & h_6 \\ h_7 & h_8 & h_9 \end{pmatrix}$.

Dividing the first and second rows of equation 2.9 by the third row results in the following two equations [14]:

$$-h_1x - h_2y - h_3 + (h_7x + h_8y + h_9)\,u = 0 \tag{2.10}$$

$$-h_4x - h_5y - h_6 + (h_7x + h_8y + h_9)\,u = 0 \tag{2.11}$$

Equations 2.10 and 2.11 can be expressed in matrix form as [14]:

$$A_i\mathbf{h} = \mathbf{0}$$

here, $A_i = \begin{pmatrix} -x & -y & -1 & 0 & 0 & 0 & ux & uy & u \\ 0 & 0 & 0 & -x & -y & -1 & vx & vy & v \end{pmatrix}$
and $\mathbf{h} = \begin{pmatrix} h_1 & h_2 & h_3 & h_4 & h_5 & h_6 & h_7 & h_8 & h_9 \end{pmatrix}^T$.

To determine the homography matrix H, having a set of 4-point correspondences is sufficient, although more correspondences usually mean a more robust solution, as each correspondence provides two equations. However, it is important to note that no three points can be collinear; they must be in a "general position". Stacking four 2×9 A_i matrices (one per point correspondence) can obtain a single 8×9 matrix A. The null space of A, which represents the solution space for **h**, is one-dimensional [14]. Regardless of the number of point correspondences utilised, if all correspondences are exact, matrix A will have a rank of 8, resulting in a single homogeneous solution. However, in practice, an exact solution may not be achievable due to uncertainties and approximate points. In such situations, the objective is to find a vector **h** that minimises an appropriate cost function [14]. Homography estimation is a very important stage of stitching an image, and deep homography may be seen as a crucial stage in deep image stitching. This approach was first suggested by DeTone in [15], where the network architecture employed is reminiscent of Oxford's VGG Net and operates by taking two grayscale images, stacking them together, and passing them through 8 convolutional layers with subsequent max pooling. Following this, the processed data flows into two fully connected layers, while dropout regularisation is implemented to mitigate overfitting. Within this architecture, the regression network serves to predict 8 real-valued numbers directly, whereas the classification network utilises a quantisation scheme to generate confidence values for each corner prediction. This performed better than conventional methods in scenarios with large overlap rates, which is the case in this dissertation.

Nie et al. [12], proposes a homography estimation network structure as is represented in Figure 2.3:

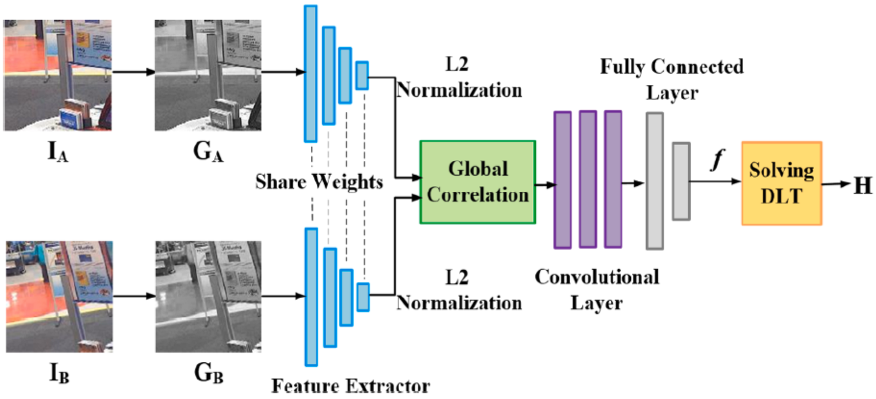

Figure 2.3: Network structure for homography estimation for the first method analysed. From [12].

This network has two input images that are converted to grayscale. Since the images concerning this dissertation consist of point spread functions, they can be treated as grayscale images and input, skipping this first stage. Following this, an extractor with shared weights is employed to learn feature representations. This also reduces the dimension of the feature maps in the Feature Extractor in Figure. 2.3. In this blue area, each small block includes two convolutional layers and a max-pooling layer. After this stage, a normalisation is applied to the feature maps and followed by a global correlation layer to learn to which features match between the two feature maps. These feature-wise global similarities are give to us by [12], with F_A^l and F_B^l being the features and x_A^l and x_B^l being the 2D spatial location of said features:

$$CV^l\left(x_1, x_2\right) = \frac{< F_A^l\left(x_1\right), F_B^l\left(x_2\right) >}{\left|F_A^l\left(x_1\right)\right| \left|F_B^l\left(x_2\right)\right|}, \quad x_1, x_2 \in \mathbb{Z}^2 \tag{2.12}$$

After processing CV, a regression network with three convolutional layers and two fully connected layers is used to predict offsets that can match the homography exactly. Finally, using the DLT approach, a convertion of expected offsets into the matching homography H in the tensor is made. The estimated global homography gives global alignment data that the next stage of structure stitching may use.

The second approach [16], proposes a multi-scale deep homography network that integrates feature pyramid with feature correlation. The architecture of the network is as follows:

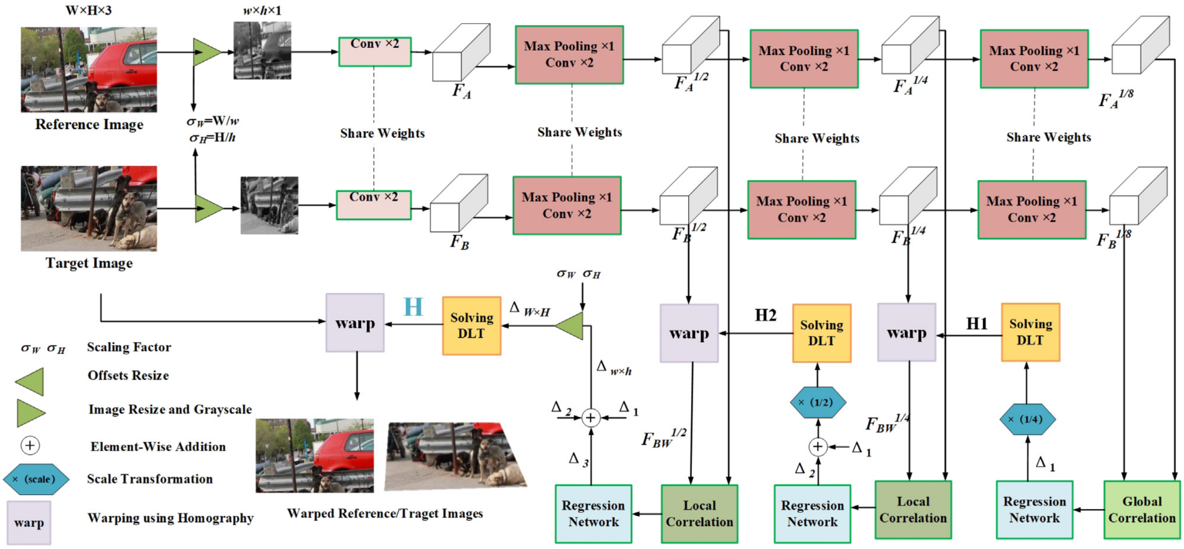

Figure 2.4: Network structure for homography estimation for the second method analysed. From [16].

Images are initially processed by eight convolutional layers when they enter the network. Each layer has 64, 64, 128, 128, 256, 256, 512, and 512 filters, respectively. A max-pooling layer is adopted every two convolutional layers to represent multi-scale features as F, $F^{1/2}$, $F^{1/4}$ and $F^{1/8}$, the latter three are chosen in order to form a three-layer feature pyramid. The features acquired in each layer of the pyramid are used to estimate the homography, transmitting the estimated homography of the upper layer to the lower layer to enhance the prediction accuracy progressively.

In addition, three of the four scales' features will be employed in the subsequent homography regression, greatly increasing the use of the features. Consistent with [12], a correlation layer is proposed, being the correlation between the two feature maps given to us by the equation 2.12. This layer objective is to strengthen feature matching, allowing for an increase in the receptive fields of the network.

A regression network is then applied, incorporating three convolutional layers and two fully connected layers, to predict eight vertices' offsets of the target image that can uniquely determine a homography. Every feature correlation in the pyramid is only calculated between the warped target feature and the reference feature, allowing each layer in the pyramid only to learn to predict the residual homography offsets instead of the complete offsets. This residual offsets, Δ_i, i = 1,2,3 are given by:

$$\Delta_i = H_{4pt}\left\{F_A^{1/2^{4-i}}, W\left\langle F_B^{1/2^{4-i}}, DLT\left(\sum_{n=0}^{i-1}\Delta_n\right)\right\rangle\right\} \tag{2.13}$$

where H_{4pt} is the operation of estimating the residual offsets. W warps the target feature map using the homography and DLT converts the offsets of the corresponding homography, with the final predicted offset calculated by:

$$\Delta_{w\times h} = \Delta_1 + \Delta_2 + \Delta_3. \tag{2.14}$$

After that, image registration can be implemented by solving the homography and warping the input images.

2.1.3 Image Fusion

Image fusion is a crucial process in machine vision that involves generating an enhanced image surpassing the quality of the original image. It leverages a specialised application that considers multiple image features within the same scene, utilising redundant and complementary information in the image data [17]. This technique aims to produce a fused image that integrates the most salient and valuable details from each input image, thereby enhancing the overall perceptual quality and extracting meaningful information. Pixel-based and pixel-domain image fusion methods have also been widely applied in the field of space image processing. These techniques have proven valuable in enhancing space images' quality and information content, enabling researchers to extract more accurate and detailed insights from the vast amount of data collected by telescopes and other space instruments.

Several techniques can be employed to fuse images with relatively straightforward approaches [1]. One such method is the averaging strategy, which involves computing the average value of corresponding pixels from input images to generate the final fused image. While this technique is simple to implement, it often suffers from a blurring effect that adversely affects image contrast.

Another commonly used method is the Select Maximum approach, where the pixel values with the highest intensity are selected, thus emphasising the most distinguishing features of the image. This method determines the optimal pixel values by comparing the corresponding pixels from each input image and assigning the highest value to the output image. Similarly, the Select Minimum method follows the same principle as the Select Maximum approach but with a minor distinction. In this case, it considers pixel values with the least intensity, discarding all other values. This strategy either fully incorporates the information from the source images or discards it completely without striking a balance. Consequently, both the Select Minimum method and Select Maximum methods, like the averaging, also suffer from blurring effects and reduced image contrast.

Due to the limitations of simpler techniques and in order to achieve superior fusion results, more complex methods were developed. One such approach is the Pyramid Transformation method [17], which utilises the Laplacian Pyramid. This method measures the activity level of each component by the absolute value of its decomposition coefficient, and the fusion coefficient is determined using the choose-max rule. The fusion efficiency of this method is high while retaining sufficient original information. However, the choice of decomposition method and the number of decomposition layers significantly impact the final fusion result, as a higher number of layers may lead to blurred boundaries in the fused image. Another group proposed the use of a Gradient Pyramid model [18], which employed directional filtering and calculated the local energy of a coefficient. An adaptive local similarity-based fusion rule was used, where a weighted average rule was applied for high local similarity and the maximum selection rule for low similarity. This fusion strategy gained widespread use in subsequent image fusion studies.

Wavelet transforms [17] is an alternative method that decomposes the original image into high and low-frequency coefficients, including vertical, horizontal, and diagonal information. It generally achieves better fusion results compared to the pyramid transform. However, wavelet transform is not displacement invariant, affecting fusion quality in poor image registration. To overcome this limitation, several improved wavelet transform methods have been proposed. One of those is the Multiscale Singular Value Decomposition method [17], which, while it can extract more accurate feature information and yield better fusion results, often requires a significant computational overhead due to the large amount of decomposition information involved.

In the context of space image fusion, pixel-based methods offer the advantage of obtaining precise pixel-wise weight maps, which are crucial for combining multiple images captured by different instruments or at different wavelengths. By comparing focus values obtained from different source images, these methods generate decision maps, enabling the classification of each pixel as focused or defocused [17]. The fusion rules employed in these methods, such as maximum selection and weighted average, facilitate the integration of information from multiple images, resulting in a fused image that retains the important details from each source image [18]. Similarly, pixel-domain methods play a significant role in space image fusion, particularly in cases where accurate estimation of optimal weights for different pixels is essential. By calculating the weighted average of corresponding pixels from input images, these methods effectively combine the information contained in each pixel, enhancing the overall image quality [19]. In the domain of space engineering, this approach can be particularly useful for merging images obtained from different telescopes or sensors, facilitating the analysis of celestial objects across various wavelengths and capturing a more comprehensive view of the universe. Pixel-based methods have their advantages and challenges when applied to space images. The spatial context information and accurate weight estimation provided by these methods can greatly enhance the visibility of celestial objects, improve the detection of faint features, and enable more precise measurements. However, as emphasised in the literature [19], the accurate estimation of optimal weights remains a critical factor in ensuring the success of the fusion process in space applications.

The evaluation of image fusion performance can be carried out through subjective and objective measures. However, subjective evaluation has limitations due to the need for observers with relevant expertise and the potential influence of environmental factors. It is also time-consuming and labour-intensive to organise evaluation meetings for accuracy assessment. On the other hand, objective evaluation involves the use of algorithms to calculate image quality, providing quantitative evaluation criteria. Researchers have employed various objective metrics to measure the performance of image fusion. Two commonly used metrics are Root Mean Squared Error (RMSE) and Peak Signal to Noise Ratio (PSNR) [1, 20].

RMSE is utilised to quantify the diversity between the reference and fused images. A lower RMSE value indicates that the fused image closely resembles the reference images. The RMSE calculation is defined by the following equation [1, 20]:

$$\mathrm{RMSE} = \sqrt{\frac{1}{mn}\sum_{i=0}^{m-1}\sum_{j=0}^{n-1}[I(i,j) - K(i,j)]^2} \tag{2.15}$$

where m and n represent the number of rows and columns in the image, respectively. The term $I(i,j)$ denotes the pixel value at position (i,j) in the reference image, while $K(i,j)$ represents the pixel value at position (i,j) in the fused image.

PSNR is another metric researchers use to measure image quality, considering image values and properties. It quantifies the recognised errors in the fused image by comparing them to the reference images. A higher PSNR value indicates a greater similarity between fused and reference images. The calculation for PSNR is given as follows [1, 20]:

$$\mathrm{PSNR} = 10 \times \log_{10}\left(\frac{f_{\max}^2}{\mathrm{MSE}}\right) \tag{2.16}$$

where $f_{\max}$ corresponds to the maximum possible pixel value in the image. The Mean Squared Error (MSE) measures the average squared difference between the pixels of the fused image and the reference images [1, 20]. These objective metrics provide quantitative measures for assessing the performance of image fusion algorithms, complementing the subjective evaluation process.

In recent years, deep learning methods have rapidly advanced with remarkable applications. Deep learning models leverage the network's learnability to extract features from multi-focus images and separate focused and defocused regions, ultimately generating full-focus fusion images [17]. This approach has demonstrated promising results in image fusion tasks, leveraging the power of neural networks to effectively learn and represent complex patterns and relationships in the data. As for the first proposed machine learning-based method in [12], it is composed by three stages, which are respectively: homography estimation stage, structure stitching stage and content revision stage. The latter two stages of the network are shown in Figure 2.5.

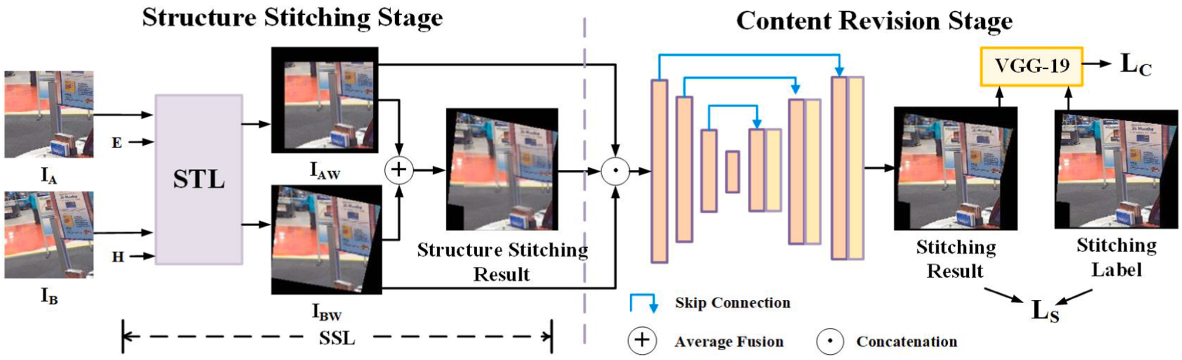

Figure 2.5: Network structure for image fusion and content revision, for the first method analysed. From [12].

The objective of dividing these two stages is due to the troublesome task of training a stitching network from scratch since it requires the cooperation of these stages to work simultaneously. A Structure Stitching Layer is introduced to acquire the structure information of stitched images. This layer first generates a grid, the same size as the stitching label, for each input image, with each element representing a 2D spatial location (u,v). Following this, the original coordinates of both images are calculated by:

$$\begin{bmatrix} x \\ y \\ z \end{bmatrix} = H^{-1} \begin{bmatrix} u \\ v \\ 1 \end{bmatrix} \tag{2.17}$$

where H is the projective transformation from the perspective I_B to I_A and (x,y,z) are the homogeneous coordinates of the original images. Afterwards, the smooth warped images are obtained using the bilinear interpolation, passing through a final stage of fusion, where the pixel value of an overlapping area results in the sum of the pixel of both images weighted by 0.5. To finalise, a Content Revision stage that consists of an encoder-decoder network is required to remove artefacts from overlapping regions while preventing severe distortion to the content of the non-overlapping parts. The method suggested is applied to three-channel RGB images, which differs from our one-channel data, meaning it's not worth a deeper analysis.

Nie proposes in [16] the use of a two-branch network to fuse the image. Due to the single-channel nature of our data, as previously mentioned, only the Edge Deformation Branch will be analysed in this document. The edge map E for a grayscale image G is given to us by the difference between adjacent pixels, as such:

$$E_{i,j} = \left|G_{i,j} - G_{i-1,j}\right| + \left|G_{i,j} - G_{i,j-1}\right| \tag{2.18}$$

After applying this formula, a convolutional layer with fixed kernels is used to extract edges, finalising by clipping $E_{i,j}$ between 0 and 1. This edge map serves as an input for the edge deformation branch, which adopts an encoder-decoder architecture.

In this branch, the number of convolutional kernels is set to 64, 64, 128, 128, 256, 256, 512, 512, 256, 128, 128, 64, 64, and 1, respectively, with a maxpooling layer adopted every two convolutional layers. Except for the last convolutional layer, all of these convolutional layers' kernel sizes are set to $3x3$ and their activation functions to ReLU. The activation function is set to Sigmoid and the kernel size to $1x1$ in the final layer to create the stitched edge. It's also worth noting, and consistent with the first method Content Review stage, skip connections were added between the low-level and high-level features with the same resolution to avoid a gradient vanishing problem and information imbalance in each layer.

2.1.4 Loss Functions

Deep homography networks are essentially regression tasks for the eight homography-related parameters. Homography must be anticipated first before computing the unsupervised loss function, even in unsupervised estimating techniques. A simple but effective way to do this is minimising the distance L_2 between the predicted offsets, $\widehat{f}$, and the ground truth f, as such [12]:

$$L_H(\widehat{f}, f) = \frac{1}{N} \|\widehat{f} - f\|_2^2, \tag{2.19}$$

where N defines the number of components in offsets $\widehat{f}$.

In both methods and in the context of image fusion, the same loss functions are applied with different purposes, although the equations are the same.

For the stitching loss function, L_1 loss is employed at corresponding positions between outputs and labels to limit the structure of stitching images to resemble that of labels as closely as possible:

$$L_{\text{edge}}(\widehat{I}, I) = \frac{1}{W \times H \times C} \|\widehat{I} - I\|_1, \tag{2.20}$$

where W, H and C are, respectively, width, height and channel number of stitching result. In [12], $\widehat{I}$ and I correspond to the stitching result and stitching label, being used in the Structure Stitching stage, where in [16], C is always equal to 1 and $\widehat{I}$ and I are denoted as the ground truth edge and edge labels from the Edge Deformation Branch.

Although the content revision from the first and second method was skipped in this document, since the solutions proposed are for images with 3 or more channels, it's still worth addressing the content loss function, which can greatly minimise the drastic changes in image features due to artefacts and image seams. The suggested approach is inspired in the VGG-19, with ψ_j being the feature map of the j-th convolutional layer:

$$L_{\text{content}}(\widehat{I}, I) = \frac{1}{W_j \times H_j \times C_j} \left\| \psi_j(\widehat{I}) - \psi_j(I) \right\|_2^2, \tag{2.21}$$

where W_j, H_j and C_j denote the feature map's width, height, and channel number, respectively.

While both L_S and L_C are used to constrain stitching results to be as close to the ground truth as possible in [16], the use of the 9th convolutional layer of VGG-19 is specified, using both outputs of the two loss functions described above to calculate an objective function:

$$L_O = \lambda_e L_{\text{edge}} + \lambda_c L_{\text{content}} \tag{2.22}$$

where λ_e and λ_c are the balance factors of edge loss and content loss, respectively.

Given the two analysed methods, the first one seems to be more effective in the context of this dissertation since it achieved almost 100% of artefact elimination in overlapping areas and is robust with reducing ghosting effects, focusing on data with a bigger overlap rate, which is the case with our data. The second article on the other hand, discusses an approach to deep stitching in low overlap rates while also preserving edges.

2.2 Super Resolution

In the realm of space engineering, our understanding of the universe is greatly enhanced by the quality and clarity of the images captured by telescopes. However, when it comes to observing deep-space objects, ground-based telescopes face numerous challenges that hinder their ability to produce high-resolution images.

The importance of super-resolution in space imaging cannot be overstated. While offering the advantage of large apertures and long exposure times, ground-based telescopes are significantly impacted by atmospheric turbulence. This turbulence introduces distortions and blurring in the captured images, resulting in reduced resolution and limited visibility of intricate details. Besides this, other noises due to Charge-Coupled Devices' (CCD) or Complementary Metal-Oxide Semiconductor (CMOS) limitations, reflections and transmission errors have to be handled [21]. Super Resolution techniques aim to mitigate these effects and restore the true structure and clarity of the observed objects.

2.2.1 Adaptive Optics

One of the most widely used techniques for correcting atmospheric turbulence is Adaptive Optics [22] (AO). Adaptive Optics systems employ real-time measurements of atmospheric distortions and make precise adjustments to the telescope's optics. By dynamically correcting the distortions, AO compensates for the blurring effects, thereby enhancing the resolution of the acquired images. This technique has revolutionised ground-based astronomy, enabling observations with unprecedented sharpness and clarity.

The Fried parameter (r_0) indicates the size of the aperture with an average of one radian of root mean square (rms) phase aberration. Achieving a moderate Strehl ratio, which is a measure of the quality of optical image formation, in an AO system requires correction on spatial scales of r_0. Interestingly, r_0 also corresponds to the aperture that produces a full-width at half-maximum (FWHM) image resolution similar to that of a diffraction-limited aperture without turbulence. It

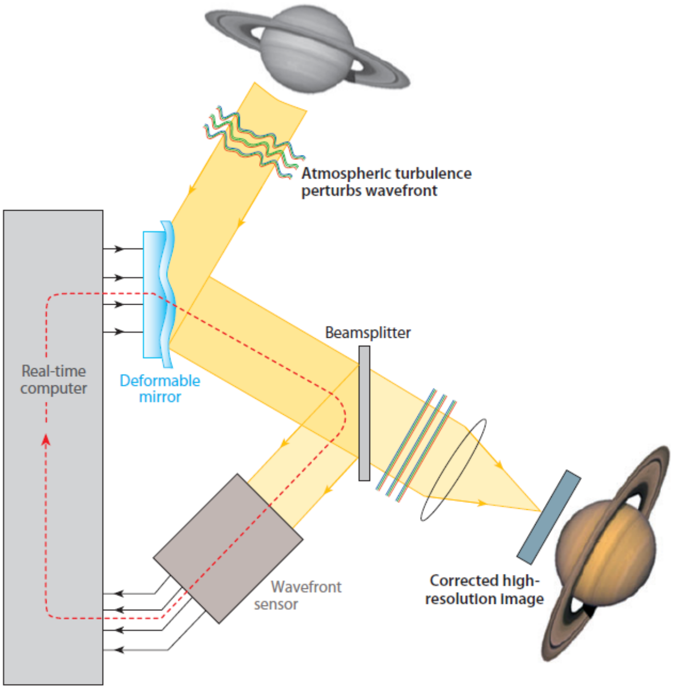

Figure 2.6: Working principle of Adaptive Optics. From [22].

decreases with increasing zenith angle (γ) and refractive index variations, while it increases with the wavelength raised to the power of 6/5. Typically, for visible wavelengths under 1-arcsec seeing conditions, r_0 is around 10 cm. The isoplanatic angle (θ_0) describes the angular extent within which optical path variations deviate by less than one-radian rms phase aberration. It represents the maximum angular radius from a correction direction where reasonably good correction can be achieved. The value of θ_0 is usually a few arcseconds for visible wavelengths and strongly depends on the distribution of turbulent layers' heights. The coherence time (τ_0) defines the time interval during which optical path variations deviate by less than one-radian rms phase aberration. It characterises the required temporal correction bandwidth for AO. The coherence time is typically a few milliseconds for visible wavelengths and is inversely proportional to r_0 divided by the average wind speed (v).

Another important parameter is the outer scale (L_0), which is typically a few tens of meters but can be larger. A wavefront that has propagated through the atmosphere does not decorrelate any further on size scales greater than L_0. The outer scale directly influences the performance of an AO system, especially when L_0 is comparable to the size of the telescope aperture. Wavefront sensing (WFS) is a critical component of AO systems as it accurately estimates the shape of the wavefront. Commonly used WFSs include the Pyramid WFS, Shack-Hartmann WFS, and Curvature WFS. Each WFS has its advantages and disadvantages in terms of sensitivity at different spatial frequencies. Recent on-sky results support the Pyramid WFS as the preferred choice for modern AO systems.

Wavefront reconstruction calculates a correction vector based on WFS measurements. It involves solving a linear system, typically using modal decomposition, filtering, and weighting techniques. Advanced control methods, such as linear-quadratic-Gaussian or Kalman filter-based methods, can further improve wavefront reconstruction and control. These methods can also incorporate telescope vibrations for efficient correction.

The deformable mirror (DM) plays a vital role in AO systems as it corrects for optical path differences caused by atmospheric turbulence. DMs come in different technologies, such as adaptive secondary mirrors, piezo DMs, and micro-optical-electrical-mechanical systems. Each technology has its advantages and limitations. Choosing the appropriate DM parameters, such as stroke, response time, spacing, and the number of actuators, is crucial to align with the Fried parameter (r_0) and the coherence time (τ_0) requirements. Combining DMs with different stroke capabilities can further optimise the correction performance.

To overcome the limitations of natural guide stars (NGS) in achieving reasonable correction performance, laser guide stars (LGS) have been introduced. LGSs are artificial guide stars created using lasers. They significantly increase the sky coverage of AO systems by providing brighter guide stars within a certain angular distance of the target.

With AO techniques already implemented in telescopes and continuously evolving, their impact on space observations cannot be overstated. However, as space engineers continually pursue greater precision and accuracy in their observations, it becomes increasingly vital to incorporate additional super-resolution methods into the imaging pipeline. These methods, which encompass advanced image processing algorithms and computational techniques, work in synergy with AO to further augment the quality of acquired images. By integrating a comprehensive suite of super-resolution techniques, engineers can ensure that the results of their observations meet or exceed the high standards required for scientific analysis, enabling breakthrough discoveries and a deeper understanding of the cosmos.

2.2.2 Frequency-based approach

One of the pioneering SR algorithms in the frequency domain is the method proposed by Tsai and Huang [23, 24]. This algorithm was designed to work with low-resolution (LR) images obtained from the Landsat 4 satellite. The LR images are related to the high-resolution (HR) scene through global translations, which are accounted for using the shifting property of the Fourier transform. By transforming the LR images into the frequency domain, Tsai and Huang combined them based on the relationship between the aliased discrete Fourier transform (DFT) coefficients of the observed LR images and those of the unknown HR image. This approach allows for extrapolating high-frequency information from the LR images to enhance the details in the HR reconstruction. The discrete Fourier transform of the LR images, denoted as $G_k(m,n)$, and their continuous Fourier transform, denoted as $F_{gk}(m,n)$, are related as follows [24]:

$$G_k(m,n) = \frac{1}{T_m}\frac{1}{T_n}\sum_{p_1=-\infty}^{\infty}\sum_{p_2=-\infty}^{\infty} F_{gk}\left(\frac{m}{MT_m}+\frac{p_1}{T_m}, \frac{n}{NT_n}+\frac{p_2}{T_n}\right) \tag{2.23}$$

, where T_m and T_n are the sampling periods along the dimensions of the LR image, and M and N, are the maximum values of the LR image dimensions. This equation accounts for the discrete sampling of the LR images from the continuous scene. The relationship between the LR images in the frequency domain and the HR scene can be expressed as [24]:

$$G = \Phi F_f \tag{2.24}$$

where G represents the discrete Fourier transform of the LR images, F_f represents the continuous Fourier transform of the HR scene, and Φ is the transformation matrix that relates the two domains. Tsai and Huang utilised a least squares algorithm to estimate the Fourier coefficients of the HR scene. The least squares algorithm aims to minimise the error between the observed LR images and the transformed HR image. Kim proposed an iterative algorithm to minimise this error, resulting in the following equation [24]:

$$|E|^2 = (G - \Phi\dot{F}_f)^{\dagger}(G - \Phi\dot{F}_f) \tag{2.25}$$

where $\dot{F}_f$ is an approximation of F_f that minimises the calculated error, and † represents the conjugate transpose. This iterative approach allows for progressively refining the estimation of the HR scene's Fourier coefficients. Incorporating a priori knowledge about the LR observations into the SR reconstruction can further improve the results. This can be achieved using a recursive weighted least squares algorithm, where the LR images with higher signal-to-noise ratio are assigned greater weights.

While the Fourier transform-based SR methods, including Tsai and Huang's algorithm, provide an intuitive way to enhance the details of LR images and have low computational complexity, they are limited in handling real-world applications that involve complex displacements and non-linear blur [23, 24]. To address these challenges, researchers have explored the use of wavelet transforms for SR [23]. Wavelet transform provides a powerful and efficient multi-scale representation of images, which is beneficial for recovering high-frequency information lost or degraded during the image acquisition process . Wavelet-based SR approaches typically treat the observed LR images as low-pass filtered subbands of the unknown wavelet-transformed HR image. The HR image can be reconstructed by estimating the finer scale subband coefficients and applying the inverse wavelet transform. Researchers have proposed various wavelet-based SR algorithms to improve upon the limitations of the Fourier transform-based methods. Ei-Khamy [23] introduced a wavelet SR approach that incorporates registration in the wavelet domain, followed by fusion of the registered wavelet coefficients and interpolation to obtain a higher-resolution image. Ji and Fermuller [23] proposed a robust wavelet SR approach that addresses errors in both registration and blur identification computations. Chappalli and Bose [23] incorporated a denoising stage into the wavelet-domain SR framework, developing a simultaneous denoising and SR reconstruction approach. These advancements in wavelet-based SR techniques demonstrate the potential for handling real-world challenges and improving the quality of HR image reconstructions. However, further research is necessary to explore hybrid approaches and novel algorithms that can effectively address the complexities introduced by factors such as noise, blur, and non-linear distortions in practical SR applications [23, 24].

2.2.3 Lucky Imaging

In the quest to obtain high-resolution images of space objects, researchers have explored various techniques to mitigate the adverse effects of atmospheric turbulence. Lucky Imaging (LI) is one such method that has gained considerable attention for its ability to enhance the resolution of space images. By capitalising on brief moments of improved atmospheric conditions, lucky imaging selectively combines frames to produce sharper and more detailed images. At its core, LI involves carefully selecting and combining frames from a rapid sequence of captured images. These frames are acquired using high-speed imaging cameras, which enable the capture of a large number of frames in a short period. However, it is worth noting that (LI) is not limited to specific camera types, as it can be implemented with any high-speed imaging camera, making it versatile in practice [25].

The frame selection process in lucky imaging is critical for achieving superior results. Each frame is assessed based on its image quality, with factors such as sharpness and fidelity taken into account. One common metric used to quantify the quality of a frame is the fraction of light concentrated in the brightest pixel of the Point Spread Function (PSF) [26]. Frames with a higher fraction of light in the brightest pixel indicate better image quality. The selection of frames is based on their quality factors, with a fraction of frames chosen to optimise the trade-off between resolution enhancement and the desired signal-to-noise ratio. The selected frames are then shifted and added, aligning their brightest speckle positions. This alignment process eliminates the contribution of tip-tilt errors caused by atmospheric turbulence or telescope pointing errors [25].

A reference star is selected as a guide for aligning the frames to exploit the turbulence-induced blurring present in each frame. By sinc-resampling the guide star image in each frame, a sub-pixel estimate of the position of the brightest speckle is obtained. This sub-pixel accuracy allows for precise alignment of the frames, compensating for atmospheric distortions [26].

One intriguing aspect of lucky imaging is its ability to yield higher resolution even when only a fraction of the frames are selected for the final image. The fortunate frames chosen possess the sharpest PSFs, resulting in improved angular resolution. It is worth noting that lucky imaging's resolution enhancement capability can be particularly advantageous when dealing with objects that exhibit slightly smeared images in one direction while maintaining full resolution in the orthogonal direction [25]. Moreover, lucky imaging can be complemented with Fourier analysis to enhance the resolution of space images further. By exploring the amplitude of complex elements in the Fourier plane, frames are selected in Fourier space. This approach offers an alternative perspective, considering the components of the image rather than the full image itself. The Fourier components are combined to generate the final output image [25].

A recent development in Lucky imaging is given to us by Wang et al. [27], where a novel approach is proposed that overcomes the limitations of conventional Lucky Imaging and Lucky

Fourier (LF) algorithms, hybridising both methods. The LI algorithm operates in the spatial domain and selects good images based on a specific selection rate, typically those with a high Strehl ratio, to enhance image quality. This approach consumes less memory but may not utilise available information effectively. In contrast, using a specific selection rate, the LF algorithm operates in the frequency domain and selects good complex data at each spatial frequency. It combines the selected complex data from multiple images based on Fourier image amplitudes to generate a composite representation, effectively enhancing image quality. However, the LF algorithm requires higher computational resources and memory consumption compared to the LI algorithm. Both algorithms rely on selection rates to control data selection and superposition processes, which directly influence the outcome of the lucky imaging technique. Different selection rates can lead to variations in the effective information contained within the results.

The goal is to extract maximum effective high-resolution information from short-exposure images and generate a resultant image with improved resolution. To achieve this, the proposed algorithm combines the selection rates from the original one-dimensional point sets in both the space domain and frequency domain into a two-dimensional point set on a plane. This integration allows for the extraction of effective information using the frequency-domain lucky imaging rule.

The algorithm follows a specific implementation method consisting of several steps. Four parameters define the initial value and increment of the space-domain and frequency-domain selection rates. These parameters control the variation of the selection rates during the iterative process. The process starts with the initial selection rates and continues until reaching a terminal value of 1. Good images are selected based on the instantaneous Strehl ratio and transformed into corresponding Fourier images using the Fast Fourier Transform (FFT) for each selection rate in the space-domain. In the frequency domain, good complex data is selected and superposed according to the index of maximum amplitude, known as the amplitude rule. This involves combining the selected complex data from multiple images to create a composite representation. The algorithm performs a second frequency-domain fusion from the Fourier images obtained by selecting the complex data with the largest amplitude at each spatial frequency. This step effectively enhances the utilisation of information from the original short-exposure images. Finally, the Inverse Fast Fourier Transform (IFFT) is applied to the fused Fourier image to obtain the final high-resolution reconstructed image.

The algorithm introduces novel image selection and storage schemes to reduce memory usage while ensuring the best images and complex data selection. In the image selection and storage scheme for the LI algorithm, the peak value of the current input image replaces the minimum peak among the selected peaks found through comparison. Similarly, the current clipped image replaces the clipped image corresponding to the minimum peak in the image storage area. This approach ensures the selection of a specific number of images with the highest peaks at a given space-domain selection rate. The new complex data selection and storage scheme replaces the conventional comparison-based approach for the LF algorithm. The current Fourier amplitude corresponding to each spatial frequency replaces the minimum amplitude found through comparison, and the current complex data is written to the complex data unit corresponding to the minimum amplitude. A hybrid lucky imaging algorithm is formed by incorporating these image selection and storage schemes. The hybrid algorithm leverages the strengths of both algorithms while providing flexibility in adaptation based on the specific selection rates chosen.

The proposed hybrid lucky imaging algorithm offers a versatile and powerful solution for extracting high-resolution information from short-exposure images. By seamlessly integrating the space-domain and frequency-domain processing, optimising memory usage, and overcoming the limitations of specific selection rates, the algorithm provides improved resolution and independence from the selection rate.

2.2.4 Drizzle Algorithm

The Drizzle algorithm serves as the foundation for precise alignment and combination of multiple images in the field of space engineering. This algorithm ensures that the resulting image is a single, high-resolution composition by effectively mitigating noise and artefacts. Its remarkable capabilities are achieved through the utilisation of a sophisticated sampling and weighting technique. Building upon the Drizzle algorithm, DrizzlePac emerges as a powerful software package developed by the Space Telescope Science Institute (STScI). Originally designed for the Hubble Space Telescope (HST) calibration pipeline, DrizzlePac has expanded its reach and is now widely employed across ground-based and space-based observatories. Its primary objective is to enhance the resolution and quality of space images, thus becoming an indispensable tool in the field.

This software package combines the Drizzle algorithm with a user-friendly interface and an implementation in Python. It allows space engineers and researchers to interact with the software through both interactive and command-line modes, further enhancing its accessibility and usability.

The Drizzle algorithm, developed by Fruchter and Hook [28], is an improved method for combining dithered images to enhance resolution and reduce correlated noise. It allows for the creation of a higher-resolution output image by smoothly varying between interlacing and shift-and-add techniques. Drizzle operates by mapping pixels from the original input images to the subsampled output image, considering shifts, rotations, and camera distortions. However, to avoid additional blurring caused by the convolution with the pixel shape, Drizzle introduces the parameter *pixfrac*. This parameter controls the shrinking of the pixel, or "drop," before it is averaged into the output image. The drop size, defined as the ratio of the linear size of the drop to the input pixel, is controlled by *pixfrac*.

To determine the values and weights of the output pixels, the Drizzle algorithm uses the following equations [28]:

$$W'_{x_o y_o} = a_{x_i y_i x_o y_o} w_{x_i y_i} + W_{x_o y_o} \tag{2.26}$$

$$I'_{x_o y_o} = \frac{d_{x_i y_i} a_{x_i y_i x_o y_o} w_{x_i y_i} s^2 + I_{x_o y_o} W_{x_o y_o}}{W'_{x_o y_o}} \tag{2.27}$$

where $W'_{x_oy_o}$ and $I'_{x_oy_o}$ represent the resulting values and weights of the same pixel, and s is the scale parameter controlling the degree of subsampling of the output. The iterative application of the Drizzle algorithm to the input data, pixel-by-pixel, image-by-image, produces usable output images and weights I and W after each input image is processed.

The final output images, obtained after processing all the input images, are given by [28]:

$$W_{x_oy_o} = a_{x_iy_ix_oy_o} w_{x_iy_i} \tag{2.28}$$

$$I_{x_oy_o} = \frac{d_{x_iy_i} a_{x_iy_ix_oy_o} w_{x_iy_i} s^2}{W_{x_oy_o}} \tag{2.29}$$

where the Einstein convention is used for summation over repeated indices, and the input indices x_i and y_i extend over all input images.

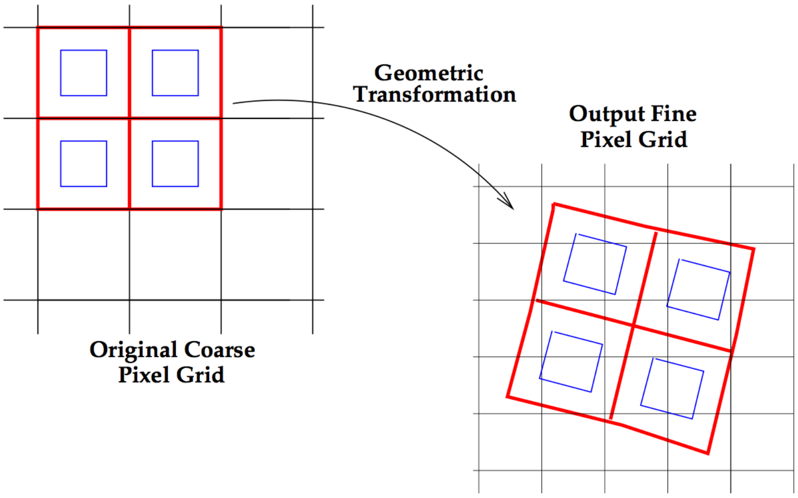

Figure 2.7: Representation of how drizzle maps input pixels onto the output image. From [28].

The behaviour of the Drizzle algorithm is influenced by the parameter pixfrac, which can be set between 0 and 1. A value of 0 corresponds to pure interlacing, while higher values introduce additional broadening of the output point spread function (PSF) by convolving the original PSF with non-zero size pixels. Setting pixfrac to 1 is equivalent to shift-and-add, where the output image PSF is smeared by convolution with the full size of the original input pixels [29]. The degree to which the Drizzle algorithm departs from interlacing and moves towards shift-and-add depends on how well the point spread function (PSF) is subsampled by the shifts in the input images [29].

The Drizzle algorithm effectively recovers high spatial frequency information and enhances image resolution by combining subpixel dithered images. It overcomes the limitations of simple linear techniques like interlacing and shift-and-add, offering improved results in terms of resolution and correlated noise reduction [29].

A more recent method developed is called DrizzlePac described in [29]. This Python package extends the capabilities of the Drizzle algorithm, providing additional tasks for image alignment, distortion corrections, and coordinate transformations. These enhancements improve the alignment and combination of HST images, enabling more accurate and precise results for various space applications. One of the key components of DrizzlePac is the TweakReg task, which is specifically designed for precise image alignment. TweakReg employs advanced algorithms to determine the necessary shifts and rotations required to achieve sub-pixel alignment of input images. The alignment process begins by generating source catalogues that contain positional information of detected objects within the images. Various techniques such as centroiding and model fitting are utilised to accurately identify and extract sources from the images.

To calculate the optimal transformations for image alignment, TweakReg utilises different alignment methods. These methods include centroid-based alignment, cross-correlation alignment, and pattern-matching algorithms. By comparing the detected sources with catalogued sources, TweakReg obtains precise positional information and performs the necessary adjustments to align the images. It also takes into account any geometric distortions present in the images and applies calibration or correction procedures to mitigate these distortions during the alignment process. DrizzlePac incorporates distortion corrections to improve the accuracy of image registration and combination. The implementation of distortion corrections follows a step-by-step process [29]:

1. Apply the detector pixel-grid irregularities (D2IMFILE) to correct the raw pixel values of the image.
2. Apply the SIP (Simple Imaging Polynomial) coefficients to further correct the pixel values after the detector correction.
3. Combine the filter-dependent part of the distortion using a look-up table correction (NPOLFILE) in conjunction with the D2IMFILE and SIP-corrected pixel values.
4. Apply the World Coordinate System (WCS) transformation, represented by the CD matrix, to obtain intermediate world coordinates.
5. Add the Right Ascension and Declination position at the reference pixel (CRVAL1 and CRVAL2) to the transformed positions, yielding positions on the tangent plate.
6. Apply the inverse projection from the tangent plane to the celestial sphere, resulting in the true world coordinates.

These distortion corrections improve the accuracy of image registration and alignment, providing more reliable coordinate transformations for subsequent analysis and processing. In addition to image alignment and distortion corrections, DrizzlePac offers tasks for coordinate transformations. These tasks allow users to convert positions between different coordinate systems, facilitating accurate astrometric measurements and analysis. Coordinate transformations in DrizzlePac are performed using a combination of WCS information, CD matrix, distortion corrections, and polynomial distortion models. The transformed positions on the celestial sphere are obtained by applying the appropriate corrections and transformations to the intermediate world coordinates.

Overall, the Drizzle algorithm and DrizzlePac have significantly advanced the field of space engineering and astronomy by providing researchers and astronomers with powerful tools for precise image alignment, combination, distortion correction, and coordinate transformations. These advancements have led to improved resolution, reduced correlated noise, and more accurate and reliable results, enabling enhanced precision and quality in various space applications.

2.2.5 Machine Learning Algorithms

Machine learning methods for super-resolution, such as the proposed multi-frame super-resolution (MFSR) method, offer several advantages. They can leverage the additional signal information present in multiple LR images to generate higher-quality outputs compared to single-image super-resolution approaches [30]. In the case of MFSR, if the input images have sub-pixel shifts due to camera motion, they provide different LR samplings of the scene, allowing for more accurate reconstruction. In this subsection, two distinct methods for MFSR will be explored.

Bhat et al. [30] proposes a methodology aimed at introducing a novel technique for MFSR that directly operates on noisy RAW bursts obtained from a handheld camera. The primary objective of their approach is to generate an output consisting of a denoised, demosaicked, and super-resolved image. In order to accomplish this, the authors have developed an innovative attention-based fusion module that has the capability to selectively merge an arbitrary number of input frames, resulting in a high-quality output. Unlike previous methods that are constrained to handling simple motion patterns such as translation or homography, the authors employ the estimation of dense pixel-wise optical flow. This optical flow estimation enables the alignment of deep feature encodings for each input frame at a pixel level. As a result, the proposed alignment process facilitates the adaptive selection of reliable and informative content from each image while simultaneously discarding misaligned regions.

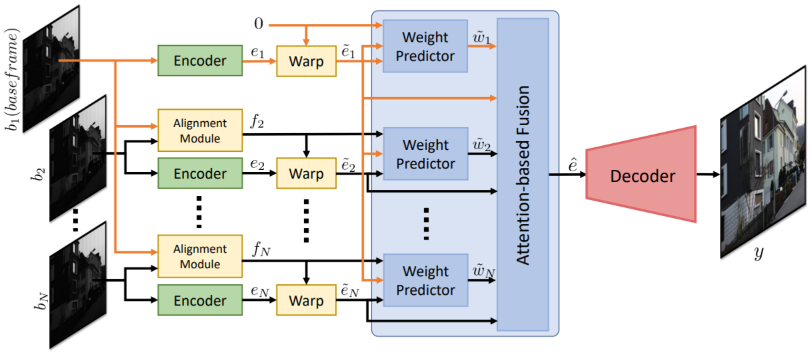

Figure 2.8: Overview of the architecture of the burst super-resolution network. From [30].

The architecture of the burst super-resolution network is illustrated in Figure 2.8, and it consists of three main modules: the encoder, alignment module, and fusion module, followed by the decoder [30]:

1. **Encoder Module**: The encoder module maps each input burst image to a deep feature representation. To achieve translational invariance, the raw Bayer pattern of each image is first packed into a 4-channel image at half the initial resolution. This low-resolution image is then processed by the encoder, which consists of an initial convolutional layer followed by a series of residual blocks. The final output is a high-dimensional encoding that allows effective fusion of multiple frames.

2. **Alignment Module**: To align the frames, dense pixel-wise optical flow is computed between each burst image and a reference image. The estimated flow vectors are used to warp the feature maps of each frame to the reference frame. This alignment process ensures that the deep feature encoding of each frame is properly aligned. While the author says that "any state-of-the-art optical flow network can be employed as a flow estimator", Bhat specifies the use of the PWC-Net [31] due to the ability to operate on RGB images, discarding one of the two green channels in $\tilde{b}_i$ to generate input RGB images. Between every burst image $\tilde{b}_i$ and the reference image $\tilde{b}_1$, pixel-wise flow captures both global camera motion and object motion in the scene. The estimated flow vectors f_i are used to warp the feature maps e_i to the base frame using a bilinear kernel [30]:

$$\tilde{e}_i = \phi(e_i, f_i), \quad f_i = F(\tilde{b}_i, \tilde{b}_1) \tag{2.30}$$

   Here, ϕ represents the warping operation, F is the flow estimator, and $\tilde{e}i$ is the resulting warped feature map. The warped feature maps $\tilde{e}^N i = 1$, as well as the computed flow vectors f_i^N, are then passed to the fusion module. Additionally, the flow vector f_1 for the base frame is set to 0.

3. **Fusion Module**: The fusion module adaptively merges the aligned feature maps using an attention-based fusion approach. It predicts element-wise fusion weights using a weight predictor network based on the aligned feature maps and flow vectors and enhances computational efficiency by projecting the feature maps to a lower dimension and utilising flow vectors for weight estimation. These fusion weights determine the contribution of each frame to the merged feature map. The merged feature map ê is obtained through a weighted sum of the aligned feature maps using the fusion weights:

$$\hat{e} = \sum_{i=1}^{N} w_i \cdot e_i, \quad w_i = \frac{e^{\tilde{w}_i}}{\sum_j e^{\tilde{w}_j}}, \quad \tilde{w}_i = W\left(\tilde{e}_1, r_i, \hat{f}_i\right) \tag{2.31}$$

   Here, $\cdot$ denotes element-wise multiplication. The merged feature map $\hat{e}$ is then passed to the decoder module to generate the final output.

4. **Decoder Module**: The decoder module takes the merged feature map as input and generates the final output HR image. It consists of residual blocks and sub-pixel convolution layers. The sub-pixel convolution is used to effectively decode the sub-pixel information encoded in different feature channels, resulting in a higher-resolution feature map. Finally, the feature map is processed by additional residual blocks and a convolutional layer to obtain the high-resolution RGB image.

The second proposed method for MFSR is presented in [32], called HighRes-net, is a neural network designed for multi-frame super-resolution. It operates on grayscale images within a single spectral band. HighRes-net employs joint co-registration and fusion of multiple low-resolution views in an end-to-end learning framework. It consists of an encoder-decoder architecture and is trained using high-resolution ground truth images as supervision.

The methodology of HighRes-net can be divided into three main steps: encoding, fusion, and decoding. In the encoding step, the network learns relevant features associated with each low-resolution view. To overcome the redundant low-frequency information present in multiple views, a reference image is computed as a shared representation for all views. This reference image helps highlight differences across the views and allows the network to focus on difficult high-frequency features during super-resolution. This mechanism is referred to as implicit co-registration. HighRes-net's embedding layer, shared across all views, consists of a convolutional layer and two residual blocks with PReLu activation's.

In the fusion step, the embedded hidden states from different views are recursively fused. The number of low-resolution states is halved at each fusion step. The fusion process involves aligning the representations and merging them using shared fusion and residual blocks. This fusion is performed iteratively until the final low-resolution encoded state contains information from all input views.

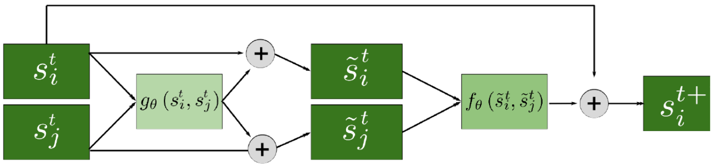

Figure 2.9: HighRes-net's global fusion overview. From [32].

After the fusion step, the final low-resolution encoded state is upsampled using a deconvolutional layer to a higher-resolution space. The hidden high-resolution encoded state is then convolved with a 1x12D kernel to produce the final super-resolved image.

Co-registration plays a crucial role in the fusion step. HighRes-net learns to implicitly co-register the multiple low-resolution views and fuse them into a single super-resolved image. It is important to note that the co-registration scheme does not assume that the differences in low-resolution images are solely due to translation motion. The network can handle other types of motion as well. To improve registration and super-resolution, HighRes-net is trained in cooperation with ShiftNet-Lanczos, another neural network. ShiftNet-Lanczos predicts sub-pixel shifts between pairs of high-resolution images and applies them using Lanczos interpolation. The networks are trained together in an end-to-end manner, minimising a joint loss function.

The methodology of the proposed method was designed based on its performance in the ESA competition, where the leaderboard ranking is based on the clear Peak Signal-to-Noise Ratio score. The final joint objective function combines the reconstruction loss between the super-resolved image and the ground truth high-resolution image, along with a regularisation term for the predicted sub-pixel shifts.

In the context of deep space images, both methods provide valuable contributions. Bhat's approach is particularly well-suited for handling handheld camera bursts, addressing challenges related to noise and motion, such as the effects caused by the atmosphere. Alternatively, Deudon's HighRes-net, with its focus on grayscale images and joint co-registration, offers a robust framework for enhancing the quality of deep space images in a single spectral band, such is the case with the dataset of this dissertation.

2.3 Critical analysis

In this chapter, a comprehensive analysis of various techniques has been conducted, encompassing image stitching techniques, multi-frame super-resolution methodologies, and machine learning algorithms.

The exploration began with a detailed examination of image stitching techniques, considering options such as feature detection, homography estimation, and image fusion methods. These algorithms are applicable to both single and multi-telescope image stitching. A notable aspect of feature detection is the iterative Laplacian of Gaussian (iLoG) method, which proves useful in improving accuracy of blob type features, such as stars in space imagery. By employing the iLoG, the performance of shift-and-add operations in matching the centroids of different stars is expected to be significantly enhanced, thereby ensuring the proper alignment of various features and increasing the robustness of the algorithms. Consequently, the selection of an appropriate fusion method is crucial in achieving optimal results for both super-resolution techniques and multi-telescope image stitching, where techniques such as the Laplacian Pyramid and Wavelet transform are worth investigating further due to their ability to capture and represent image details at multiple scales, providing a multi-resolution analysis that allows for the selective fusion of specific scales while preserving fine structures and textures, as well as extracting localised features based on frequency content. Continuing the analysis, various super-resolution methodologies were investigated, with an allusion to adaptive optics and its importance in the field, followed by different methodologies that can prove effective in the context of this dissertation. In light of this study, the drizzle algorithm and lucky imaging methodologies emerge as promising techniques to employ, offering effective solutions for fusing multiple frames into a single high-resolution image. These methodologies have demonstrated their effectiveness in enhancing spatial resolution, minimising distortions caused by optical aberrations and atmospheric turbulence, and improving the overall quality and clarity of the final images.

Moreover, the study considered the incorporation of machine learning algorithms in these domains. In cases where both single and multi-telescope techniques fail to yield the desired outcomes, machine learning-based methods offer potential solutions. These methodologies incorporate diverse elements and demonstrate promise for inspiring future research. By leveraging machine learning algorithms, further advancements can be made to enhance the performance and effectiveness of image stitching and super-resolution techniques in the field of deep-space images. As it will be shown later in the thesis, classical approaches yielded very good results and therefore there was no need to implement machine learning solutions in the research work.

Chapter 3

Dataset

3.1 Data Acquisition

3.1.1 GRAVITY

The dataset employed in this dissertation is acquired by a leading-edge instrument called GRAVITY. The GRAVITY design aims to provide a largely self-contained instrument for precise narrow-angle astrometry and phase-referenced imaging of faint targets in K-band (wavelength range of 2.0-2.4 μm) [33]. This instrument is a four-telescope beam combiner for the European Southern Observatory Very Large Telescope Interferometer, able to achieve spatial resolutions equivalent to that of a telescope of approximately 130 metres in diameter with an accuracy of a few ten-microarcseconds. Additionally, GRAVITY features an interference fringe tracking system that employs adaptive optics to account for atmospheric turbulence in order to resolve small and dim celestial objects [34, 35].

The Sagittarius A* (Sgr A*) supermassive black hole at the heart of our galaxy serves as the primary scientific driver for GRAVITY and provides answers to various important physics and astrophysics-related questions. One of the stars with the closest known peri-centre distance to Sgr A* is the phase reference star S2 (IRS16C), which orbits Sgr A* once every 16 years [33].

The SgrA* data acquired by GRAVITY can then be downloaded in the European Southern Observatory Raw Data archive as files in the Flexible Image Transport System (FITS) format, which in turn is useful to store separated but related astronomical sets of data into one single file. The FITS file format also provides the storage of unlimited multidimensional arrays, allowing each array to be stored in distinct extensions, meaning each array has its own header [36].

3.1.2 Imaging through turbulence

The acquisition camera images are collected by telescopes on the ground affected by atmospheric turbulence. Here we shortly refer to the factors limiting the optical image quality of the camera.

The optical quality of an image from an optical system is described by the impulse function of that system. In optics, this is called the point spread function (PSF). The PSF determines

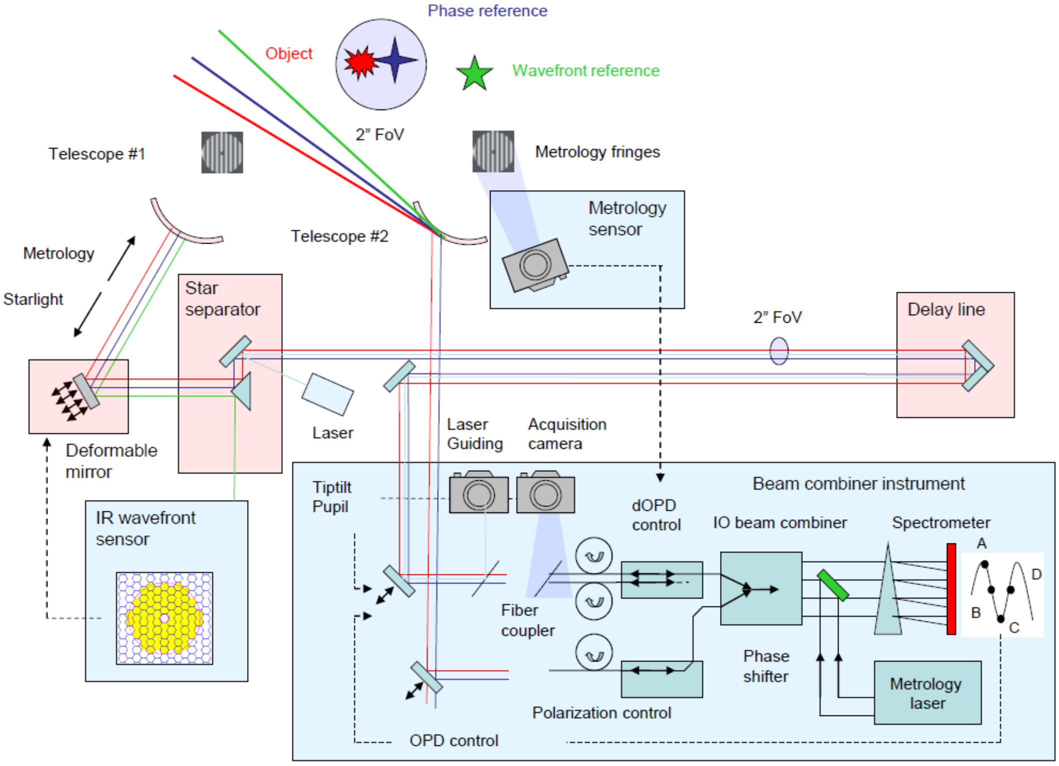

Figure 3.1: Overview and working principle of GRAVITY. From [33].

the resolution of the instrument, which is the smallest angular separation that the instrument can distinguish between two sources 3.2. To perform flux measurements, the captured data is fitted to a PSF template, allowing the extraction of parameters of the observed point-like sources accurately. These PSFs comprise several points (pixels) with varying intensities in relation to the photons detected by the detector during the exposure [38, 39]. However, the PSF of a telescope is further degraded by two effects. The main in ground-based observations is atmospheric turbulence which significantly degrades the PSF for telescopes larger than a few tens of cm. Another effect is instrument noise and sampling. Hence, space engineers must carefully calibrate their instruments to ensure that they obtain accurate measurements and high-resolution images. This calibration process involves measuring the PSF and modelling its contribution to the overall system PSF, allowing for more accurate measurements of the observed sources [37, 39].

Atmospheric Effects

As mentioned before, ground-based observatories have a major disadvantage compared to space-based ones, this being the light diffraction caused by the Earth's atmosphere. This turbulence has a major impact on the quality of the images captured by these telescopes and can be seen by the naked eye. An example of this is the twinkling of starlight, called scintillation.

What impact does the atmosphere have on the quality of the images? Since only a very small portion of the spherical wave, radiated from a far-off, point-like source, gets intercepted by the

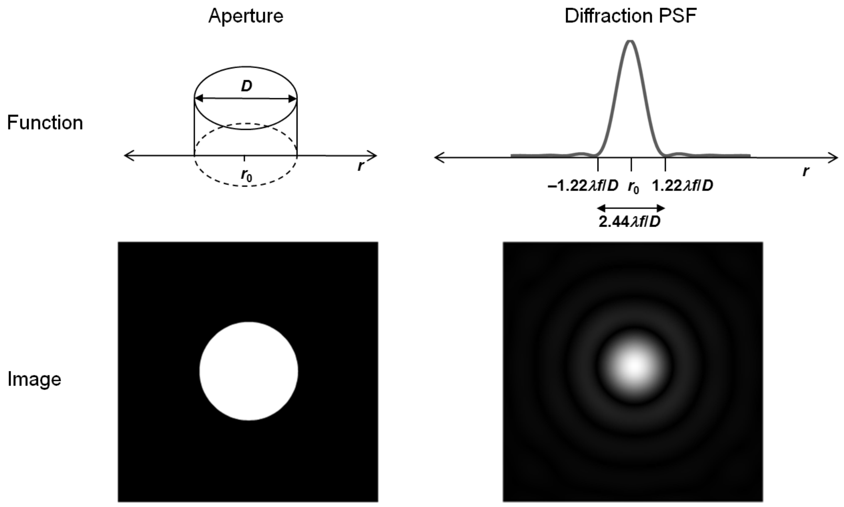

Figure 3.2: The diffraction PSF from an unobstructed circular aperture is the Airy disk. From [37].

Earth. These waves' wavefronts are flat and parallel when they reach the Earth. Fluctuations in density, which in turn result mostly from temperature variations in a developed turbulent atmosphere, affect the refractive index of air molecules. These molecules, each with a slightly varying index of refraction, randomly deform these planar wavefronts, acting like lenses, bending the incoming rays [22, 40]. As a result, the light rays that enter the telescope are no longer parallel, and the wavefront is no longer flat. Consequently, the prerequisites for producing an image that is simply restricted by diffraction are not met [38]. Therefore, due to the exposition required by CCDs, the images acquired suffer from two major effects over time:

- The observed light sources appear to be hazed.
- The observed light sources appear to change positions.

Depending on whether long- or short-exposure images are taken into account, a large ground-based telescope's intensity point-spread function (PSF) can assume one of two distinct shapes. In the long-exposure case, the intensity distribution is smooth as a result of the natural averaging that takes place. For the short-exposure case, the intensity distribution takes the form of a random speckle pattern. Although, through the use of a perfect drive mechanism, a long-exposure image can be acquired by adding a series of short-exposed images, with both the ensemble-average short-exposure PSF being almost identical to the long-exposure PSF, having a smooth distribution owing to averaging [41, 42]

3.1.3 Acquisition Camera

The acquisition camera images have different optical functions. Of interest to this dissertation is the imaging of the SgrA* field function. As previously mentioned, telescopes capture light in order to produce an image, and once the light has been collected and corrected by the adaptive optics system, it then goes through an instrument to a detector. All space instruments have a detector at their core that transforms electromagnetic radiation into an electrical signal. This small device collects light over time to create a much clearer and brighter image. The two detector types used most frequently nowadays are Complementary Metal–Oxide–Semiconductors (CMOS) and charged coupled devices (CCD). The acquisition camera detector is a HAWAII 2RG CMOS detector

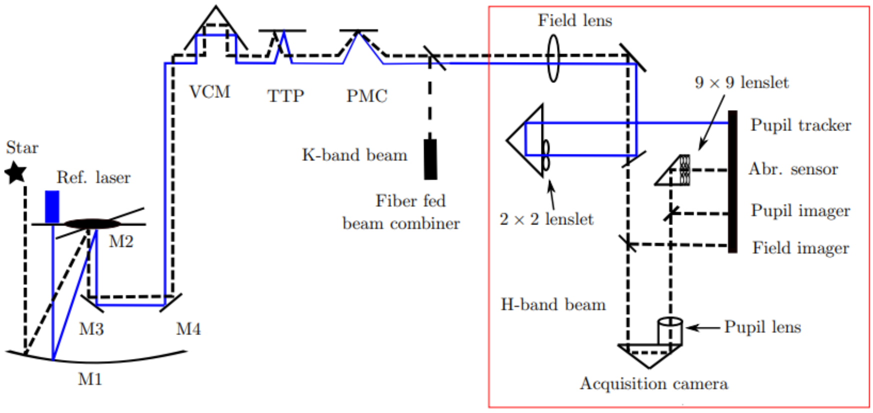

Figure 3.3: The acquisition camera working principle and optical layout (only one beam case). From [43].

The HAWAII 2RG detector, based on Complementary Metal-Oxide-Semiconductor (CMOS) technology, offers numerous benefits, making it an exceptional imaging device in space engineering. This advanced detector demonstrates remarkable sensitivity across a wide range of wavelengths and provides excellent performance in handling light intensities with a linear response. The accurate and reliable measurement of photon-generated signals is ensured by the CMOS technology. Furthermore, CMOS sensors are known for their low-power consumption, making them energy-efficient devices. Due to its CMOS-based architecture, the HAWAII 2RG detector benefits from reduced power requirements, enabling extended observation periods in astronomical applications. Additionally, the utilisation of silicon-based manufacturing processes in CMOS sensors helps reduce production costs, making them more affordable and accessible to a wider range of applications [44].

In comparison [44, 45] to CCDs, CMOS sensors, including the HAWAII 2RG, offer distinct advantages. CMOS sensors often provide higher pixel counts within a single sensor, eliminating the need for complex multi-CCD mosaics. This characteristic simplifies the design and packaging of the imaging system. Functionally, CCDs operate similarly to CMOS sensors, where each pixel in the sensor array absorbs incident photons, converting their energy into electrical charge. However, CMOS sensors employ an active pixel architecture, integrating individual amplifiers within each pixel. This design enables faster readout rates and reduced electronic noise when compared to CCDs. Another significant advantage of CMOS sensors is their faster charge transfer rate. This attribute allows for shorter exposure times, even when dealing with faint astronomical sources.

Unlike CCDs, CMOS sensors do not require total darkness during the charge removal phase, significantly reducing the risk of smear caused by extraneous light. Leveraging this faster charge transfer rate, the HAWAII 2RG detector efficiently captures high-resolution images of celestial objects.

The acquisition camera of the GRAVITY telescope plays a critical role in compensating for various distortions that can affect the quality of observations. The camera works in the H-band (wavelength range of 1.4-1.8 μm) and analyses laser guiding beams to trace tip-tilt and pupil motion, which are then corrected using internal sensors and actuators [33, 35]. The camera provides field and pupil images, a Shack-Hartmann wavefront sensor image, and a pupil tracker image for all four telescopes. It measures high-frequency image motions caused by air turbulence in the optical train of the VLTI, which are not detected by wavefront sensors located in the coudé rooms of the telescopes. The pupil tracker measures both lateral and longitudinal pupil motion and sends corresponding corrections to the instrument's internal pupil actuator and the VLTI main delay line variable curvature mirror [33].

The acquisition camera and the science spectrometer are equipped with a Teledyne 2048x2048 pixel, HAWAII2RG detectors controlled with the ESO New General detector Controller [33]. The detectors are operated in non-destructive mode, using its 32 100 kHz analogue outputs. The quantum efficiency at a wavelength of 2 μm, which represents the percentage of photons detected by a detector at this specific wavelength, is around 80%

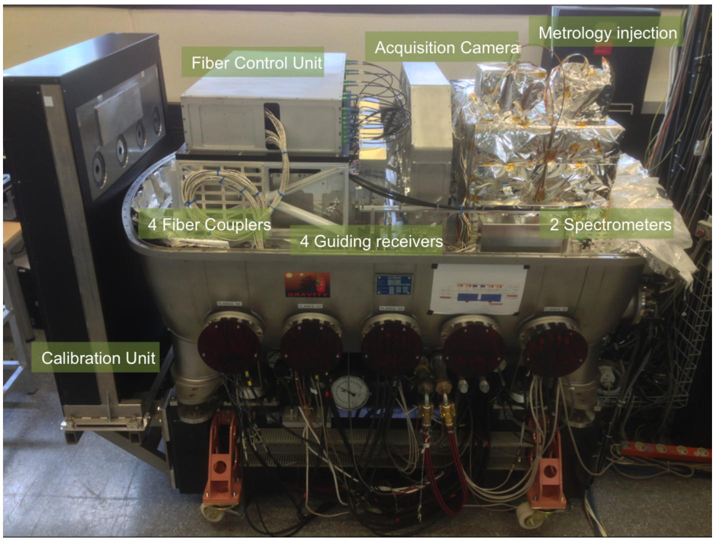

Figure 3.4: Overview of the beam combiner instrument including the acquisition camera. From [35].

3.2 General Statistics of the Dataset

The background in deep space images can be a challenging issue in astronomical research, as it can contain various noise sources and signals unrelated to the observed object. Other artefacts from characteristics inherent to imaging devices, including astronomical cameras, are the presence of broken pixels and random reflections. These possess the peculiarity of being non-responsive to incident light or exhibiting irregular behaviour, consequently resulting in localised image artefacts. Understanding and mitigating these factors' impact is paramount in ensuring accurate analysis and interpretation of astronomical images.

The dataset of this dissertation includes 21 observations of the same cluster of stars, which are characterised by two different orientations and a number of frames. It consists of sixteen observations with 246 frames each, while the remaining five observations contain 94 frames. Irrespective of the observation, each frame has been exposed for an identical duration of 0.7 seconds. This standardised exposure time ensures uniformity in the duration of light capture throughout the dataset, minimising potential variations arising from exposure changes.

Table 3.1: File Information

File	**Date**	**Number of Frames**
GRAVI.2020-03-06T07_58_46.121	06/03/2020	94
GRAVI.2020-03-06T08_07_58.143	06/03/2020	94
GRAVI.2020-03-06T08_31_31.203	06/03/2020	246
GRAVI.2020-03-06T08_39_25.223	06/03/2020	246
GRAVI.2020-03-06T08_45_55.240	06/03/2020	246
GRAVI.2020-03-06T08_52_19.256	06/03/2020	246
GRAVI.2020-03-06T08_58_43.272	06/03/2020	246
GRAVI.2020-03-06T09_05_25.288	06/03/2020	246
GRAVI.2020-03-06T09_13_19.309	06/03/2020	246
GRAVI.2020-03-06T09_19_46.325	06/03/2020	246
GRAVI.2020-03-06T09_26_16.341	06/03/2020	246
GRAVI.2020-03-06T09_39_43.375	06/03/2020	246
GRAVI.2020-03-06T09_46_13.392	06/03/2020	246
GRAVI.2020-03-06T09_52_34.408	06/03/2020	246
GRAVI.2020-03-07T07_46_09.234	07/03/2020	94
GRAVI.2020-03-09T07_35_28.155	09/03/2020	246
GRAVI.2020-03-09T09_51_10.497	09/03/2020	246
GRAVI.2020-03-12T07_02_55.661	12/03/2020	94
GRAVI.2020-03-12T07_12_13.684	12/03/2020	94
GRAVI.2020-03-12T07_26_07.719	12/03/2020	246
GRAVI.2020-03-12T09_55_32.096	12/03/2020	246

The dataset's statistical analysis focuses on several key parameters derived from the images. These parameters include:

1. Centroid of the Star: The centroid represents the star's centre of brightness position. Precise determination of the centroid allows for accurate tracking and measurement of the star's position over time. In the context of space engineering, the centroid of a star can be used to calculate the star's location in relation to other celestial bodies.

2. Maximum Amplitude: The maximum amplitude refers to the highest intensity value attained by the star's brightness within each image frame. This parameter provides insights into the star's intrinsic luminosity and potential variability through the frames.

3. Sigma: represents the standard deviation of pixel values within an image frame. It quantifies the spread or dispersion of the star's brightness distribution, providing an estimate of its fluctuation through the frames.

4. Distance between the Two Brightest Stars: This parameter measures the spatial separation between the two brightest stars present in each image frame. It offers insights into the relative positions and potential interactions of these stars.

5. Distance between the two most distant stars: This parameter quantifies the spatial separation between the two most distant stars visible within each image frame. It provides information on the distribution and clustering of stars in the observed field.

Furthermore, the angles associated with the distances between the brightest stars and the most distant stars are recorded. These angles provide supplementary geometric information, enabling a comprehensive analysis of the dataset.

3.2.1 Analysis of atmospheric effects on the dataset

Centroid

Firstly, for observations with better quality, the centroid exhibits a relatively low variation of approximately $< \pm 1$ pixel, while for lesser quality observations, it fluctuates more, reaching around $> \pm 2$ pixels. This indicates that the precision of the centroid estimation is more reliable in frames with better quality. Furthermore, the variations in centroid positions appear to be random between frames, lacking any discernible pattern caused by the atmospheric effects on the observations. Additionally, when analysing the histogram of the centroid positions, it is observed that most observations follow a normal distribution. This implies that the distribution of centroid values conforms to the expected behaviour, with a peak around the likely true centroid position. Moreover, the fact that there are four telescopes in the observation setup introduces an interesting aspect. The centroids of the main (reference) star differ across all telescopes but follow the same variation, meaning the atmospheric distortion effect is somewhat equal between all telescopes.

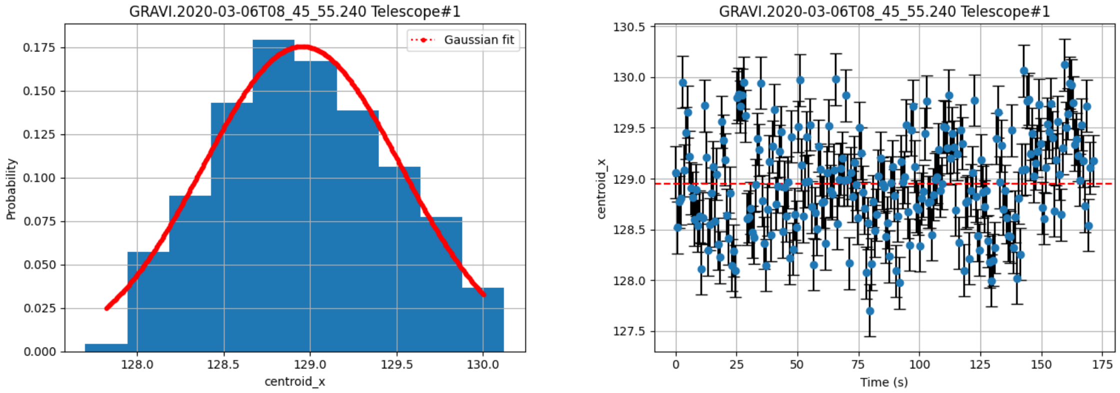

(a) Histogram distribution for Telescope 1 (b) Centroid position over time for Telescope 1

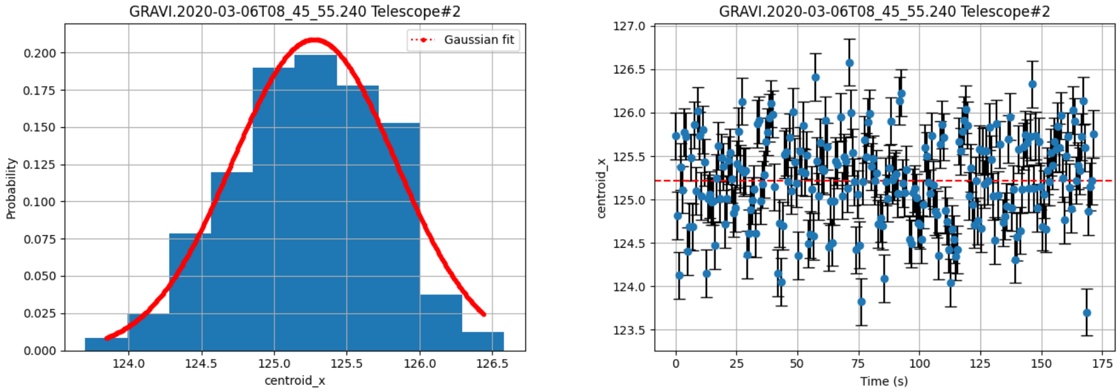

(c) Histogram distribution for Telescope 2 (d) Centroid position over time for Telescope 2

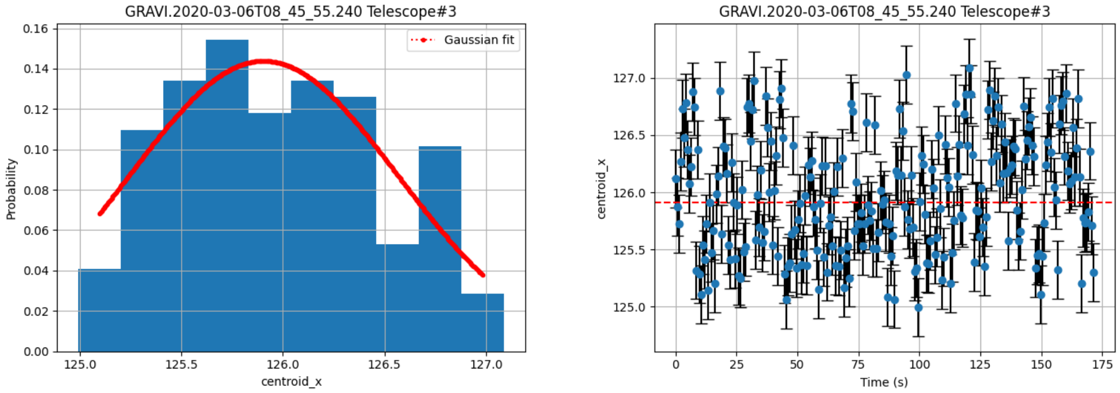

(e) Histogram distribution for Telescope 3 (f) Centroid position over time for Telescope 3

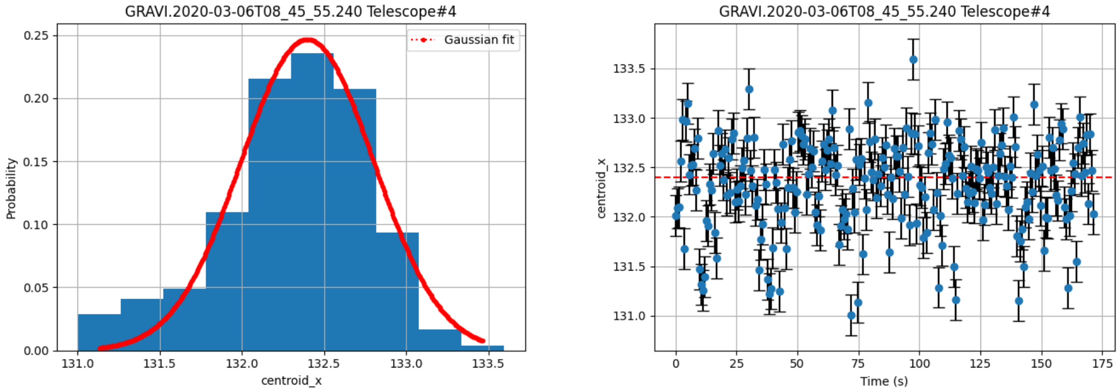

(g) Histogram distribution for Telescope 4 (h) Centroid position over time for Telescope 4

Figure 3.5: Centroid of the main star in x axis for observation 06T08_45_55.240

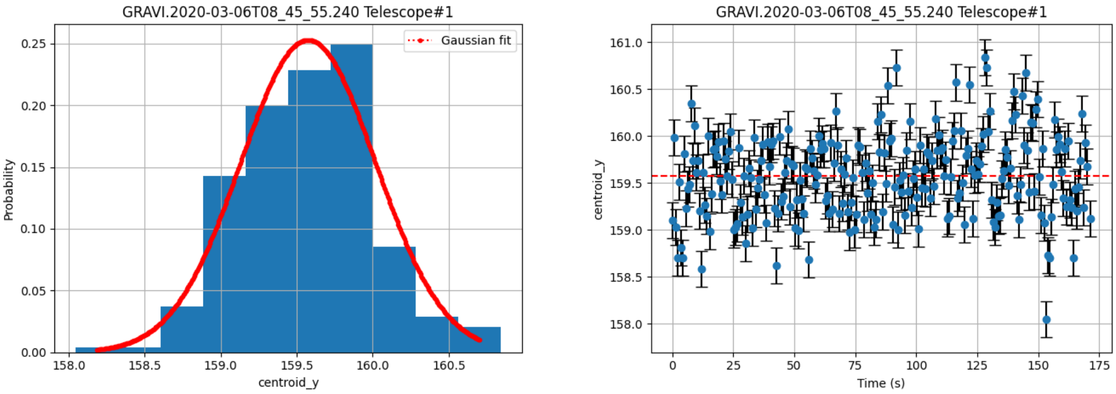

(a) Histogram distribution for Telescope 1 (b) Centroid position over time for Telescope 1

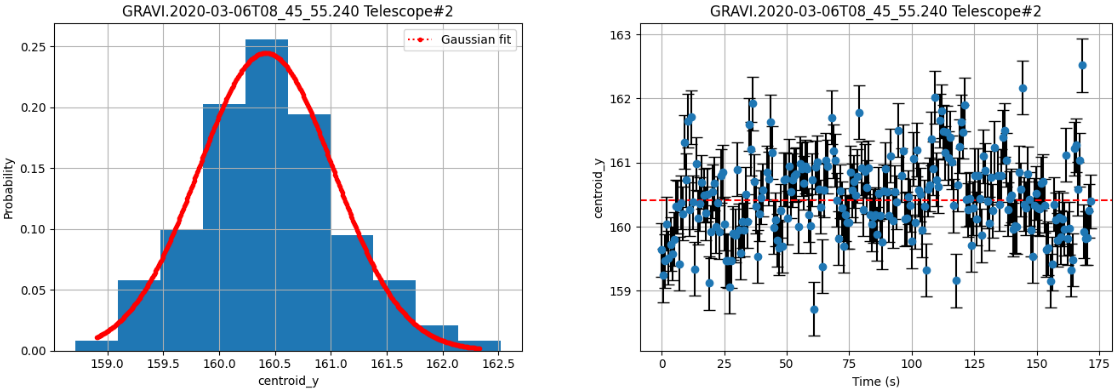

(c) Histogram distribution for Telescope 2 (d) Centroid position over time for Telescope 2

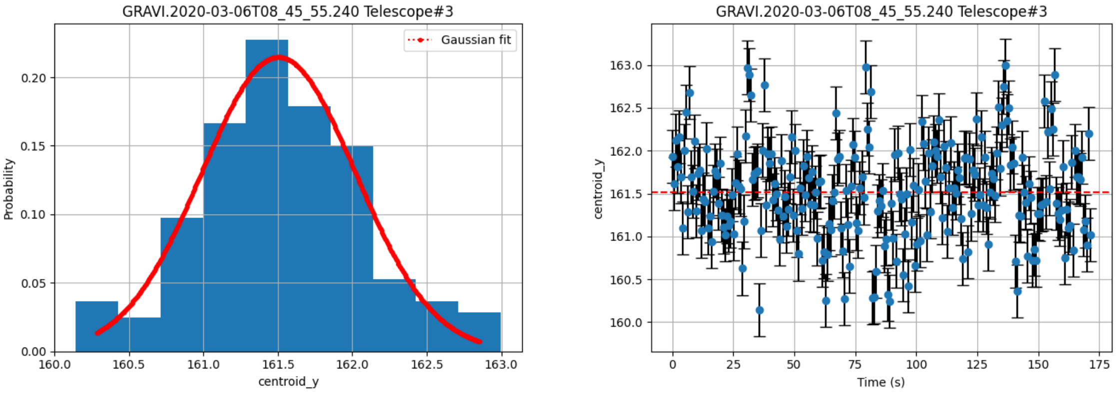

(e) Histogram distribution for Telescope 3 (f) Centroid position over time for Telescope 3

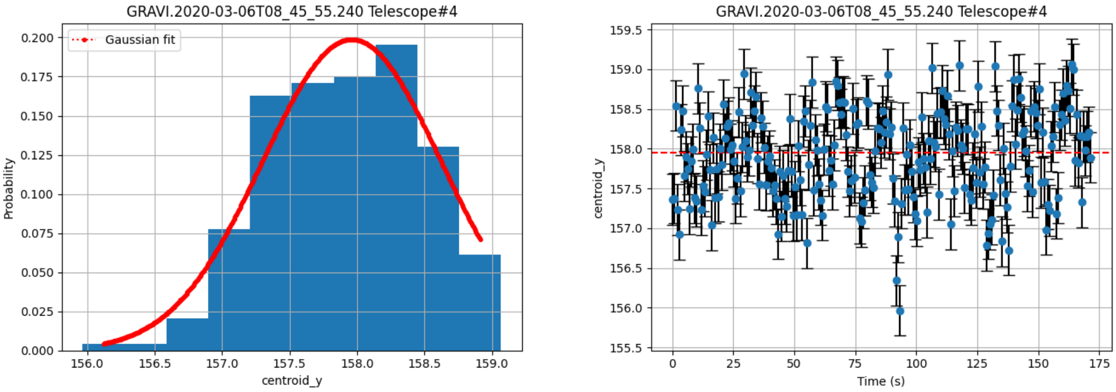

(g) Histogram distribution for Telescope 4 (h) Centroid position over time for Telescope 4

Figure 3.6: Centroid of the main star in y axis for observation 06T08_45_55.240

Maximum Amplitude and Sigma

The parameters of sigma and maximum amplitude provide valuable insights into the quality and clarity of the observed star images. The analysis shows that as the maximum amplitude of the star's intensity profile increases, the corresponding sigma value decreases. This inverse relationship indicates that frames with a larger amplitude tend to have a better-defined star, which can serve as a quality metric for frame selection for multi-frame super-resolution methods. These findings can be utilised to select suitable reference frames or differentiate between good and bad in various image processing techniques. Furthermore, the sigma and maximum amplitude values vary across the four telescopes. Among them, Telescope 1 emerges as a potential candidate to be the reference telescope when fusing the observations from all four telescopes to generate a final image. This selection is based on the lower sigma values and better-defined star profiles observed in Telescope 1. Additionally, sigma and maximum amplitude can be employed as metrics to calculate weights, enabling an optimised fusion process.

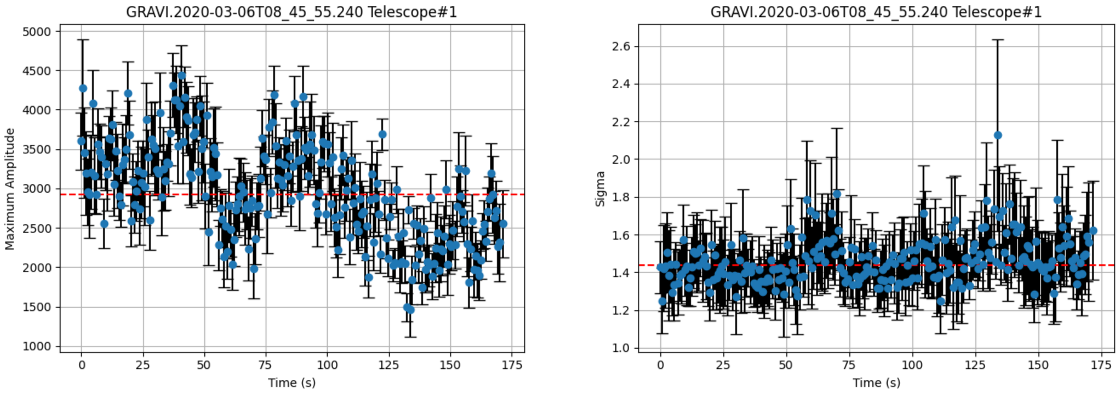

(a) Maximum Amplitude over time for Telescope 1

(b) Sigma over time for Telescope 1

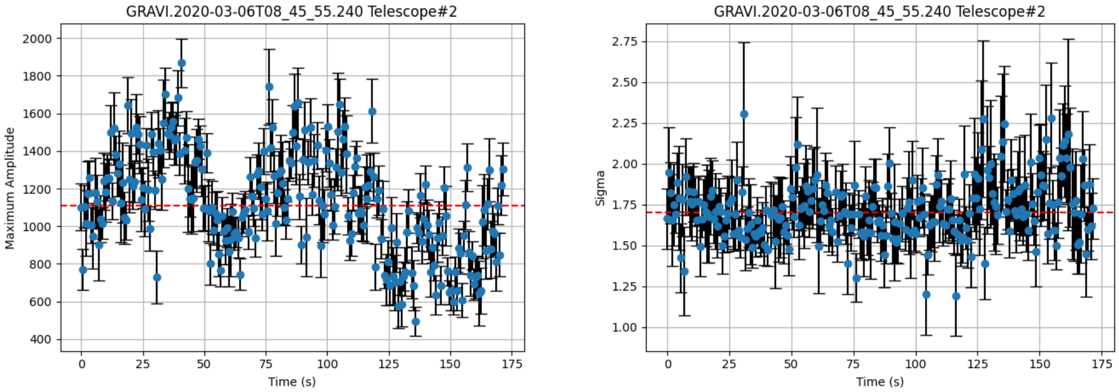

(c) Maximum Amplitude over time for Telescope 2

(d) Sigma over time for Telescope 2

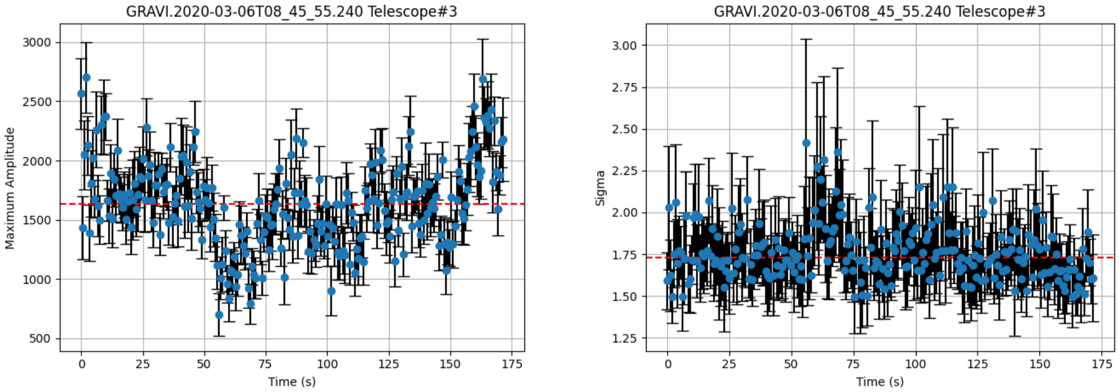

(e) Maximum Amplitude over time for Telescope 3

(f) Sigma over time for Telescope 3

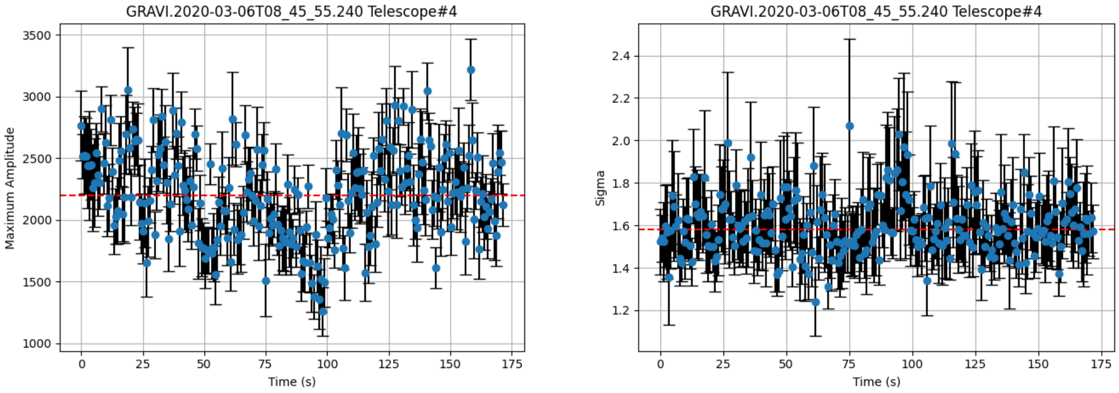

(g) Maximum Amplitude over time for Telescope 4

(h) Sigma over time for Telescope 4

Figure 3.7: Maximum Amplitude and Sigma of the main star for observation 06T08_45_55.240

Distances and Angles

Analysing the distances and angles between the two brightest stars in the observed frames provides valuable information regarding their relative positions and the atmospheric effects on the whole image. Similar to the centroid analysis, the histogram of these measurements follows a normal distribution, reinforcing the idea that the atmospheric effects are the same throughout the entire image. Furthermore, the dataset exhibits a consistent mean for both distances and angles, indicating a stable configuration of the two brightest stars across the observations. However, in a subset of 94 frames, the orientation of the field of view differs, resulting in a change in the position of the second brightest star. Consequently, this subset's angle between the two brightest stars also varies. Additionally, the third brightest star either becomes dimmer or may not be visible at all in this altered orientation.

The distance between the second and third brightest stars shows greater variation between observations compared to the distances between the two brightest stars, but the mean of the angle is somewhat constant across the dataset. This increased variability can be attributed to the lower quality or diminished visibility of the third brightest star. Furthermore, the distance distribution between these stars varies more between observations, but the distances for each observation obey a normal distribution.

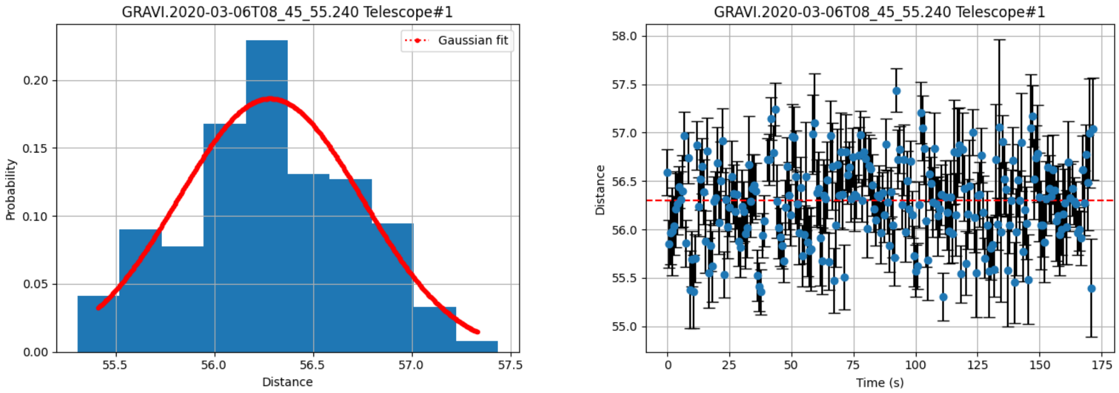

(a) Histogram distribution for Telescope 1 (b) Distance over time for Telescope 1

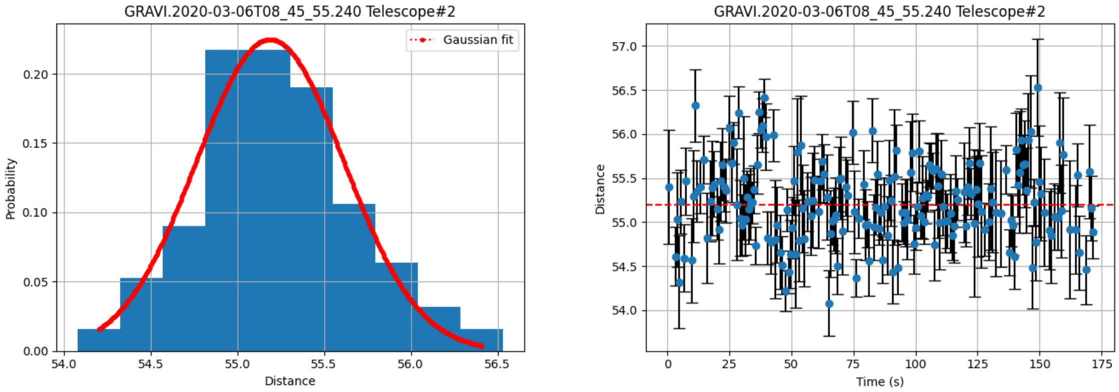

(c) Histogram distribution for Telescope 2 (d) Distance over time for Telescope 2

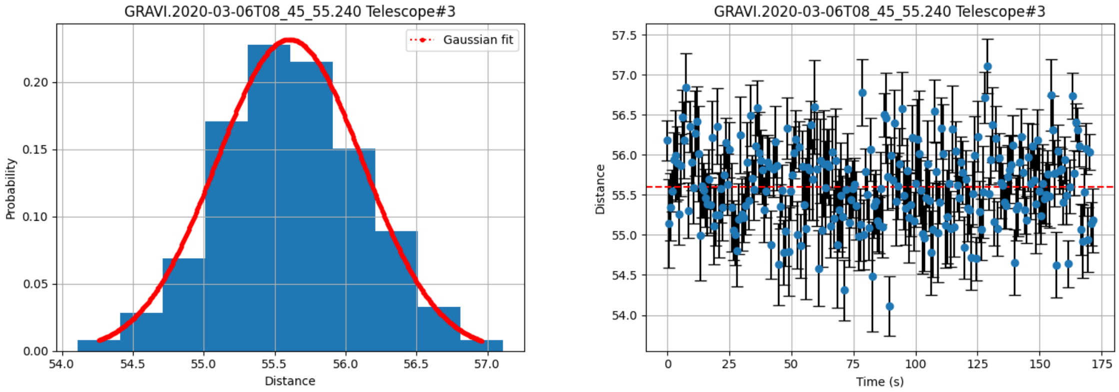

(e) Histogram distribution for Telescope 3 (f) Distance over time for Telescope 3

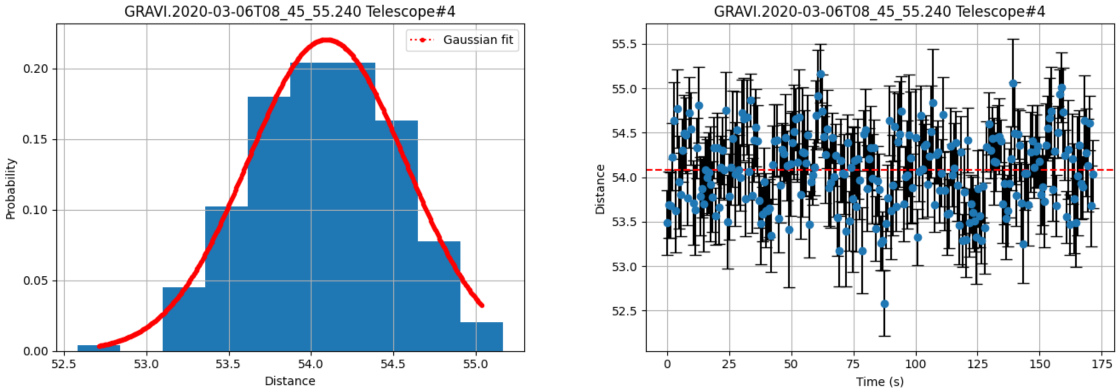

(g) Histogram distribution for Telescope 4 (h) Distance over time for Telescope 4

Figure 3.8: Distance between the two brightest stars for observation 06T08_45_55.240

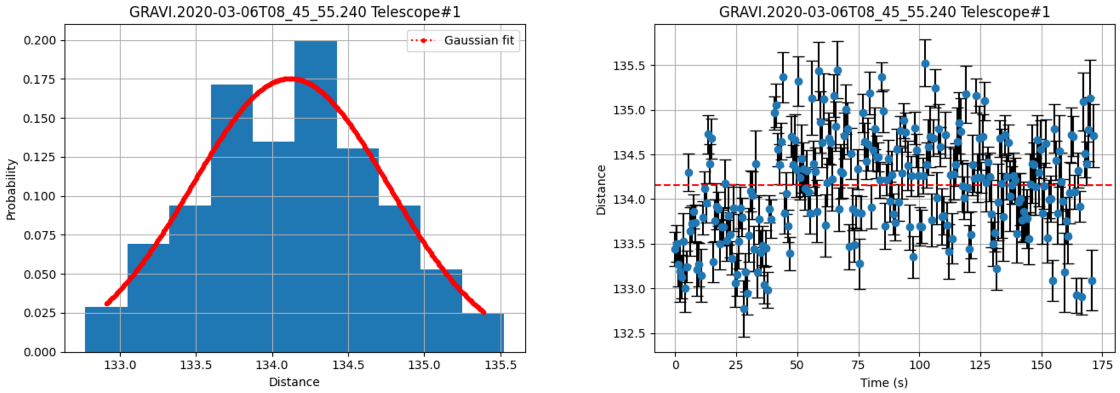

(a) Histogram distribution for Telescope 1

(b) Distance over time for Telescope 1

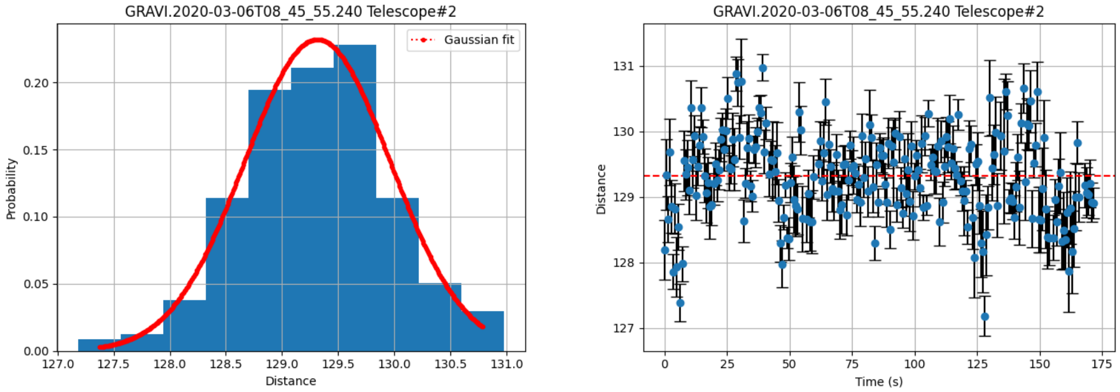

(c) Histogram distribution for Telescope 2

(d) Distance over time for Telescope 2

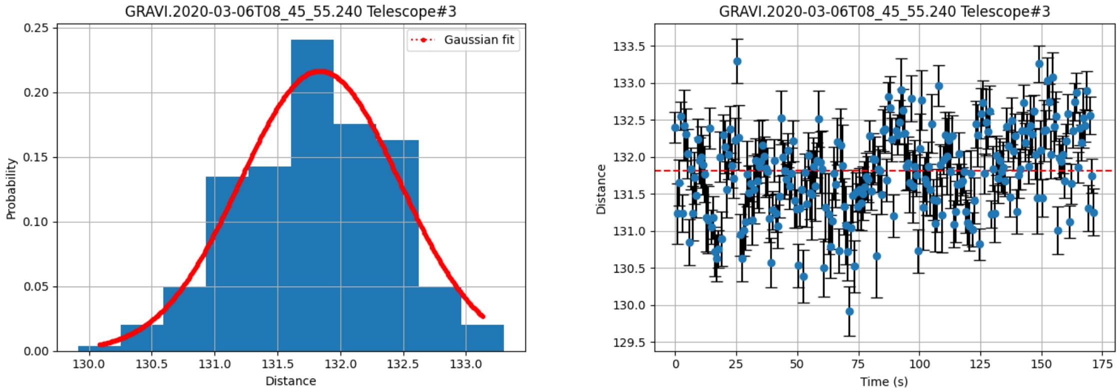

(e) Histogram distribution for Telescope 3

(f) Distance over time for Telescope 3

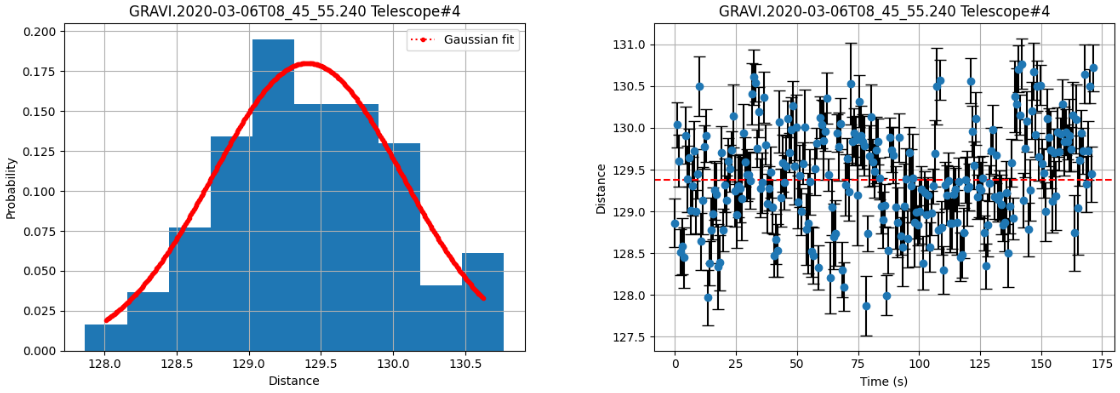

(g) Histogram distribution for Telescope 4

(h) Distance over time for Telescope 4

Figure 3.9: Distance between the 2^{nd} and 3^{rd} brightest stars for observation 06T08_45_55.240

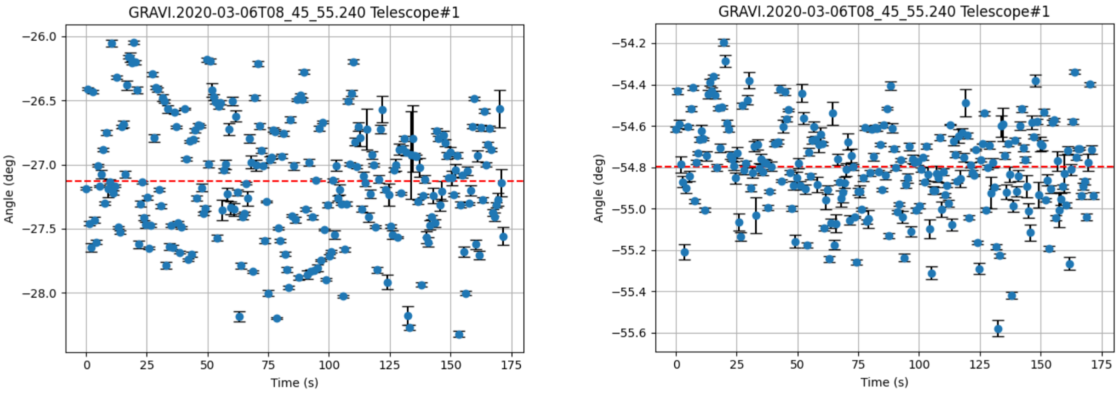

(a) Angle of the two brightest stars for Telescope 1 (b) Angle of the 2^{nd} and 3^{rd} brightest stars

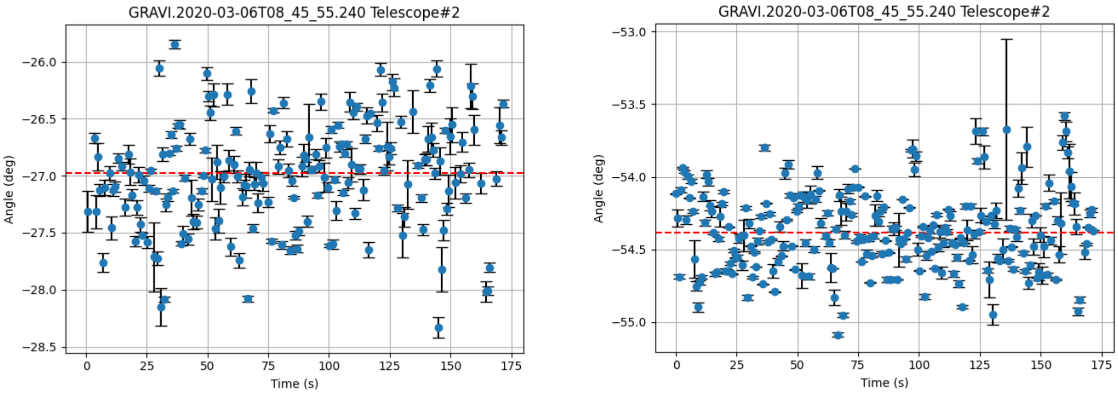

(c) Angle of the two brightest stars (d) Angle of the 2^{nd} and 3^{rd} brightest stars

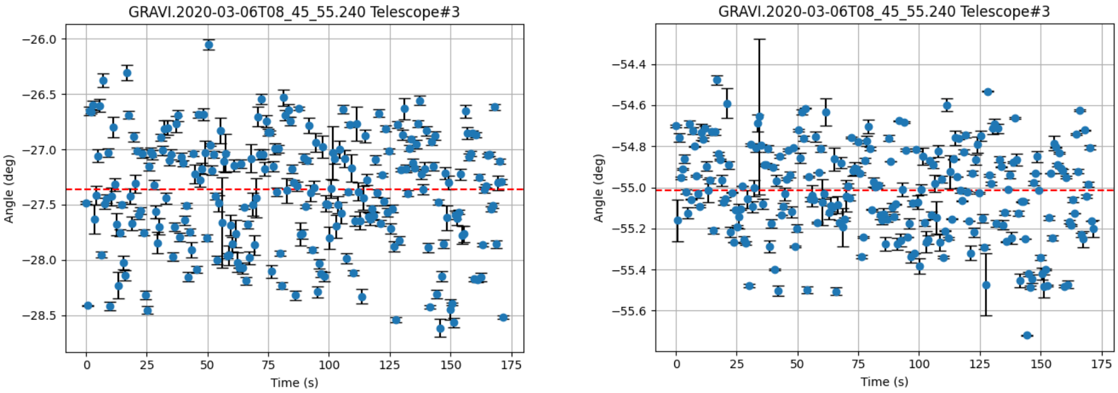

(e) Angle of the two brightest stars (f) Angle of the 2^{nd} and 3^{rd} brightest stars

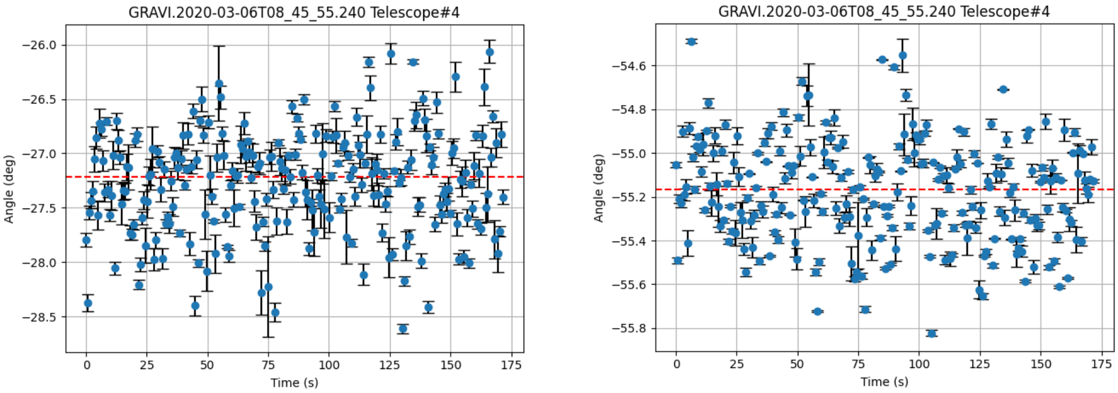

(g) Angle of the two brightest stars (h) Angle of the 2^{nd} and 3^{rd} brightest stars

Figure 3.10: Angles acquired for observation 06T08_45_55.240

3.2.2 Conclusions

In conclusion, the analysis of the centroid positions, histogram distributions, sigma values, maximum amplitudes, distances, and angles in the observed frames provides valuable insights into the quality of the images and the atmospheric effects on the observations. The precision of the centroid estimation is more reliable in frames with better quality, while lesser quality frames exhibit greater fluctuations. The random variations in centroid positions suggest the influence of atmospheric effects on the observations.

The histogram distributions of centroid positions follow a normal distribution, indicating that the centroid values conform to the expected behaviour with a peak around the likely true centroid position. The consistency in the variation of centroids across all telescopes suggests that the atmospheric distortion effect is relatively equal between them.

The inverse relationship between the maximum amplitude and sigma values implies that frames with larger amplitudes, likely due to a better exposition, tend to have better-defined stars, serving as a quality metric for frame selection. Telescope 1 stands out as a potential reference telescope for image fusion due to its lower sigma values and better-defined star profiles. The sigma and maximum amplitude values can also be used as metrics to calculate weights, optimising the fusion process.

Analysing the distances and angles between the two brightest stars reveals information about their relative positions and the atmospheric effects on the image. The normal distribution observed in the histogram reinforces the idea that atmospheric effects are consistent throughout the image. The consistent mean in distances and angles indicates a stable configuration of the two brightest stars, except in a subset of frames with altered orientations. The variability in the distance between the second and third brightest stars can be attributed to the lower quality or diminished visibility of the third brightest star.

Chapter 4

Methodology

This chapter outlines the methodology employed in this dissertation to conduct the analysis and achieve the desired results. The chapter consists of three sections, each focusing on a specific step in the research process.

Firstly, the background and foundation of the study are established by providing an overview of the DAOPHOT source detection algorithm and the Levenberg-Marquardt algorithm for Gaussian fitting. These algorithms are commonly used in the field of astronomy for the detection and characterisation of point sources in images. Understanding the principles and capabilities of these algorithms is essential for comprehending the subsequent methodology employed in this study.

Secondly, each telescope's methodology for performing multi-frame image reconstruction is presented. This process involves several key steps. To begin with, the calculation and application of weights to individual frames is shown and explained. Subsequently, three distinct methods and their respective variations are discussed for multi-frame image reconstruction. Each method offers different techniques and approaches to enhance the quality and fidelity of the reconstructed images. The variations in these methods allow for a comprehensive analysis of their advantages and trade-offs.

Finally, the chapter delves into a method used to combine all the final images from multiple telescopes into a single master image. Accurate image alignment is crucial for effectively merging data from various telescopes and obtaining a comprehensive view of celestial objects. This alignment method is presented in detail, outlining the necessary steps to align and register the images. By employing this alignment technique, the study ensures that the resulting master image faithfully represents the combined information from all the telescopes, facilitating a more comprehensive analysis.

4.1 Object Feature Acquisition

This section will provide a brief background on the DAOPHOT source detection algorithm and the Levenberg-Marquardt algorithm for gaussian fitting. Subsequently, the methodology used to acquire the previously-analysed features of stars in Section 3.2.

4.1.1 Star Detection

Developed by Peter Stetson in the 1980s, DAOPHOT [46, 47] is a powerful tool for accurately detecting and measuring the brightness of stars in astronomical images. It has become invaluable in studying various astrophysical phenomena such as variable stars, star clusters, and galaxies. DAOPHOT combines techniques like point-spread function (PSF) fitting, aperture photometry, and image subtraction to identify and measure star properties with high precision.

The author further delves into the functioning of DAOPHOT and breaks it down into four primary tasks. Firstly, it involves identifying a list of possible locations for stars. Secondly, it estimates the sky background. Thirdly, it develops a model of the point-spread function for the frame. Lastly, it obtains photometry for all stars in the image by using least-squares profile fits.

The star detection process begins by analysing each pixel in the image. For every pixel, a two-dimensional Gaussian approximation is used to model the point spread function created by a star. If a star is present at the centre of the pixel, the Gaussian approximation accurately represents it, and the height of the fitted curve indicates the star's brightness. However, if the pixel is located in an empty sky region or on the outskirts of another star, the height of the best-fitting Gaussian will be close to zero or negative. Therefore, the likelihood of a star's existence in a specific pixel is determined by the relative height of the most suitable Gaussian profile.

To estimate the sky background, DAOPHOT analyses a nearby area unaffected by the star's light. It uses a circular annulus centred on the star's location, with appropriate inner and outer radii. The sky brightness per pixel is then estimated as the mode of the pixel values within that region.

Accurate modelling of the point spread function (PSF) is essential for precise brightness and position measurements. DAOPHOT derives an empirical PSF model from a set of bright, isolated stars. The PSF image is created by averaging their images, and a bivariate Gaussian is fit to this PSF image to represent the PSF variation across the image.

To address crowding issues caused by nearby stars, DAOPHOT utilises PSF fitting. It models the PSF of each star in the image and subtracts the contributions of nearby stars, enabling accurate measurements of individual star properties. Additionally, the algorithm employs neighbour-subtracted photometry, which measures the brightness of each star twice: once with nearby star contributions included and once with the contributions subtracted using PSF fitting. The difference between these measurements provides an estimate of the star's brightness alone, improving measurement accuracy.

In this dissertation, a class from the package photutils.detection [48] called **DAOStarFinder**, which provides an implementation of the DAOFIND [46] algorithm is used for all feature detection tasks. This class searches images for local density maxima with a peak amplitude greater than a specified threshold and a size and shape similar to a defined 2D Gaussian kernel, generating a catalogue encompassing the detected stars within the image.

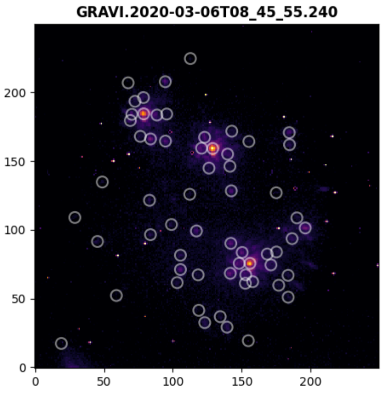

(a) All stars identified by DAOStarFinder

id	xcentroid	ycentroid	peak	flux	mag
43	128.978	159.157	2951	129.839	-5.283
19	156.058	75.629	2127	105.391	-5.057
55	78.844	184.373	1869	87.010	-4.848
47	83.827	166.098	376	14.588	-2.910
30	196.229	101.367	325	13.962	-2.862
16	141.787	68.378	283	9.477	-2.441
17	105.556	71.143	226	8.973	-2.382
60	94.539	207.737	208	8.842	-2.366
25	142.171	90.159	216	7.557	-2.195
46	94.667	164.544	170	6.772	-2.076
37	142.501	128.363	178	6.617	-2.051
49	123.103	167.302	193	6.263	-1.992
50	184.616	170.699	163	6.202	-1.981
23	150.411	83.574	161	6.138	-1.970
54	70.268	184.030	163	4.889	-1.723

(b) Table of identified stars.

4.1.2 Gaussian Fitting

The Levenberg-Marquardt (LM) algorithm [49] is an optimisation method commonly used for fitting mathematical models to data. It is particularly useful for nonlinear least squares problems, where the goal is to find the best set of parameters that minimise the sum of squared residuals between the model predictions and the observed data.

Using the LM algorithm, we start by defining the mathematical model that represents a Gaussian function to fit Gaussian profiles to stars in astronomical images. A Gaussian function is characterised by its amplitude (A), centre position (x_0, y_0), standard deviations (σ_x, σ_y) along the x and y directions, and an orientation angle (θ). The model function can be defined as follows:

$$f(x,y) = A \cdot \exp\left(-\frac{(x-x_0)^2}{2\sigma_x^2}\cos\theta - \frac{(y-y_0)^2}{2\sigma_y^2}\sin\theta\right) \tag{4.1}$$

Given a set of observed data points (x_i, y_i), the goal is to find the optimal set of parameters (A, x_0, y_0, σ_x, σ_y, θ) that minimise the sum of squared residuals between the model predictions and the observed data.

The LM algorithm iteratively updates the parameter estimates by solving a linearised least squares problem. At each iteration, it computes the Jacobian matrix, J, which represents the partial derivatives of the model function with respect to each parameter. The Jacobian matrix is evaluated at the current parameter estimates.

Using the Jacobian matrix, the algorithm constructs a linearised approximation of the problem and solves it to update the parameter estimates. The LM algorithm introduces a damping factor (λ) that balances between a Gauss-Newton-like step (more efficient but less stable) and a steepest descent-like step (less efficient but more stable).

The algorithm proceeds as follows:

1. Initialise the parameter estimates (A, x_0, y_0, σ_x, σ_y, θ) either with reasonable initial guesses or based on prior knowledge.

2. Compute the model predictions using the current parameter estimates.
3. Compute the residuals between the model predictions and the observed data.
4. Compute the Jacobian matrix, which represents the partial derivatives of the model function with respect to each parameter, evaluated at the current parameter estimates.
5. Compute the approximation of the Hessian matrix, which is a square matrix of second-order partial derivatives of the model function. The Hessian matrix is constructed by multiplying the transpose of the Jacobian matrix with the Jacobian matrix.
6. Adjust the diagonal elements of the Hessian matrix by adding the damping factor (λ) to ensure stability.
7. Solve the linearised least squares problem using the damped Hessian and Jacobian matrix. This step calculates the parameter update, that minimises the squared residuals.
8. Update the parameter estimates with the calculated update values.
9. Check the convergence criterion. If the parameter updates are sufficiently small or if the maximum number of iterations is reached, stop. Otherwise, go back to step 2.

Once convergence is reached, the final parameter estimates represent the best-fit Gaussian profiles to the stars in the astronomical image.

The LM algorithm is a widely used optimisation method because it handles nonlinear problems efficiently. In the context of fitting Gaussian profiles to stars in astronomical images, it can provide accurate estimates of the parameters that describe the shape and position of the star.

In this dissertation, the Gaussian fitting of stars is done as follows: Firstly, the star is isolated by creating a box around its catalogued centroid. A median filter is then applied, replacing the central pixel with the median of surrounding pixels, which works particularly well with salt-and-pepper noise, which includes broken pixels and the dark area. This is followed by an opening operation involving erosion and dilation using a specified kernel. The resulting mask enhances the star model's robustness, facilitating more accurate fitting. Finally, a function from astropy.modelling [50] called **LevMarLSQFitter**, which provides an implementation of the beforementioned Levenberg-Marquardt algorithm that outputs a modelled Gaussian, that should resemble a higher quality image of the captured star, is used for all star fitting tasks.

One of the outputs of the fitting function used is a covariance matrix, which is modelled as such:

$$cov\_matrix = \begin{bmatrix} \sigma_A^2 & cov(A,x) & cov(A,y) \\ cov(A,x) & \sigma_x^2 & cov(x,y) \\ cov(A,y) & cov(x,y) & \sigma_y^2 \end{bmatrix} \tag{4.2}$$

where σ_A represents the maximum amplitude standard deviation, σ_x represents the standard deviation in the x-axis, and σ_y represents the standard deviation in the y-axis.

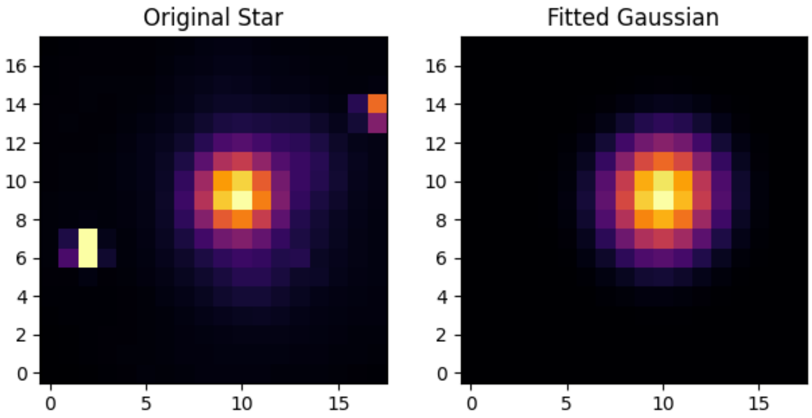

Figure 4.2: Example of a star and the respective fit.

4.1.3 Dataset Statistics Acquisition

Star Features

The approach used to acquire the features consists of several key steps to facilitate identifying and analysing stars within the image. Firstly, the stars are identified with a mask to where the star to be analysed is expected to be in the image to avoid miss-identifications. Secondly, the gaussian fitting is done as aforementioned in the previous subsection. If the fit is deemed good, the new centroid in the whole of the image can be calculated, and the sigma and maximum amplitude can be directly acquired from the fit.

Distances and Angles Calculation

Finally, to calculate the distances and respective angles between stars, the Euclidean distance formula is used, along with the formula for the angle between two points, which are, respectively:

$$d = \sqrt{(x_0 - x_1)^2 + (y_0 - y_1)^2} \tag{4.3}$$

$$\alpha = \arctan\left(\frac{y_0 - y_1}{x_0 - x_1}\right) \tag{4.4}$$

where (x_0, y_0) and (x_1, y_1) are the newly calculated centroids from the two respective stars.

Associated Uncertainties and Errors

Different observations are subjective to different conditions. Even for each observation, each frame's conditions vary. Due to this, the frame quality fluctuates, causing some stars not to be able to be fitted or even detected.

In order to separate the unsuitable fits from the images, a set of conditions has been established. When the resulting covariance matrix is determined to be equivalent to None, it indicates that the function failed to achieve a satisfactory fit. Additionally, there are instances where the function erroneously determines convergence, leading to false positives. A criterion is applied to mitigate such occurrences and exclude these erroneous convergences from the analysed data. Specifically, if the sigma or maximum amplitude is less than one, it is deemed that the fit is not suitable.

To ensure accurate data analysis, it is essential to identify and exclude any frames that can be categorised as outliers. Following the acquisition of the desired observation data, the centroids of all good fits are compared to the median centroid. Frames are considered outliers if the distance along the x or y axis exceeds a certain threshold value, indicating a significant deviation from the overall distribution of centroids. Additionally, specific conditions are applied to determine outliers in various aspects of the data. When examining object features, frames are excluded if the sigma value exceeds the expected FWHM or if the sigma error is greater than the sigma itself. Moreover, concerning distances and angles, frames exhibiting substantial deviations from the median values, both in terms of distance, angle and their respective errors, are considered outliers. Due to their significant deviations, such frames are excluded from the data to maintain a more rigorous and accurate analysis.

Calculating standard deviations and identifying propagation errors are critical steps in any rigorous analysis. By calculating standard deviations, we gain insights into the variability and dispersion of data, enabling us to understand the reliability and consistency of our findings. Progression errors, on the other hand, help us assess the accuracy and precision of measurements or predictions made over time [51, 52]. In this dissertation, we have calculated standard deviations and propagation errors as such:

Centroid To acquire the variance for the centroids of the dataset involved several steps. Firstly, a histogram of the dataset was computed to obtain the standard deviation (sigma) that would be used as a measure of variability for the centroids. The histogram values were then normalised. Subsequently, a Gaussian curve was fitted to the histogram using the optimised parameters, and the resulting plot visually demonstrated that the histogram followed a normal distribution. The optimised parameters, along with their associated uncertainties, were printed to provide further insight into the fitted Gaussian curve. This methodology allowed for the acquisition of the variance for the centroids, with the histogram analysis providing an indication of the normal distribution.

Sigma As depicted in Equation 4.2, in the positions [1,1] and [2,2], we can obtain the variance of both the x and y axis for the fitted Gaussian. From here, the standard deviation for the sigma is easily obtained by calculating the square root of the mean between the two axis.

Maximum Amplitude The standard deviation can be derived by calculating the square root of the variance, which can be obtained in the position [0,0] of the previously mentioned covariance matrix in 4.2.

Distance and Angles The formula for the propagation error is described at such [51, 52]:

$$\sigma_f^2 = \left(\frac{\partial f}{\partial x_0}\right)^2 \sigma_{x0}^2 + \left(\frac{\partial f}{\partial y_0}\right)^2 \sigma_{y0}^2 + \left(\frac{\partial f}{\partial x_1}\right)^2 \sigma_{x1}^2 + \left(\frac{\partial f}{\partial y_1}\right)^2 \sigma_{y1}^2 \tag{4.5}$$

where (x_0, y_0) and (x_1, y_1) are the new calculated centroids from two stars, and $(\sigma_{x0}^2, \sigma_{y0}^2)$ and $(\sigma_{x1}^2, \sigma_{y1}^2)$ are the respective variances. For the Euclidean Distance (in 4.3), the error can be calculated by:

$$\sigma_d = \frac{(x_0 - x_1)^2 \sigma_{x_0}^2 + (x_1 - x_0)^2 \sigma_{x_2}^2 + (y_1 - y_2)^2 \sigma_{y_1} + (y_2 - y_1)^2 \sigma_{y^2}}{(x_1 - x_2)^2 + (y_1 - y_2)^2} \tag{4.6}$$

and, for the angle, the resulting equation is:

$$\sigma_\alpha = \frac{2 \cdot \arctan\left(\frac{y_2 - y_1}{x_2 - x_1}\right)}{(y_2 - y_1)^2 + (x_2 - x_1)^2} \cdot \left((y_2 - y_1)(\sigma_{x_1} + \sigma_{x_2}) + (x_2 - x_1)(\sigma_{y_1} + \sigma_{y2})\right) \tag{4.7}$$

4.2 Single Telescope Image Reconstruction

As previously mentioned in Subsection 3.1.2, averaging various short exposures of the same scene wields results similar to a long exposure, making it an excellent candidate for a benchmark for the other algorithms. For this, the images were stacked together, and the result of the sum was divided by the number of frames of the observation.

4.2.1 Weighted Blending

When combining images, pixel weight refers to each pixel's relative importance or contribution in the final composition. It determines how much influence a particular pixel has on the resulting image. Exposure fusion involves the computational generation of an optimised image by selectively retaining the most desirable components within a series of multiple exposures. The procedure is guided by a collection of quality metrics synthesised into a weight map expressed as a scalar value. Perceiving the input sequence as a stack of individual images is conceptually beneficial. The ultimate image is then derived through the consolidation of the image stack via a process known as weighted blending. For each pixel, the various quality measures are consolidated into a scalar weight map by means of multiplication. The decision to employ a product operation as opposed to a linear combination is rooted in the objective of simultaneously upholding all quality attributes delineated by the measures [53].

In a paper by Mertens [53], three quality metrics are used to assess the weight of each pixel in an image: contrast, saturation and well-exposedness. In the context of grayscale images, the metrics of contrast and well-exposedness are still relevant for calculating weights in the Exposition Fusion method. However, since grayscale images lack colour information, the metric of saturation does not apply. Contrast refers to the difference in brightness between different parts of an image. It plays a crucial role in determining the visual impact and clarity of the image, regardless of whether it is in colour or grayscale. On the other hand, well-exposedness, also known as exposure, measures how evenly the brightness values are distributed across an image. It helps to ensure that the image is neither too dark nor too bright, and important details are visible.

The weights are calculated and applied as such[53]:

Contrast

Calculated by applying a Laplacian filter to the whole image and computing the absolute response. This yields a simple indicator C for contrast. It tends to assign a high weight to important elements such as edges and texture.

The kernel's size for both the laplacian filter and the median filter is chosen based on the expected FWHM and the quality of the observation. In the context of the Laplacian filter, a larger kernel size captures broader features, while smaller sizes focus on finer details. For the median filter, a larger kernel size results in more aggressive smoothing or blurring, while a smaller size preserves more details.

Well-exposedness

Raw intensities within a channel reflect pixel exposure quality. The aim is to retain intensities away from zero (underexposed) and one (overexposed). Each intensity denoted as 'i,' is weighted based on its proximity to 0.5 using a Gaussian curve [53]:

$$e^{-\frac{(i-0.5)^2}{2\sigma^2}}$$

here, a higher value of σ results in a wider and smoother curve, while a lower value of sigma produces a narrower and sharper curve.

Weight Calculation

Similar to the weighted terms of a linear combination, the influence of each measure can be controlled using a power function [53]:

$$W_{ij,k} = \left(C_{ij,k}\right)^{\omega_C} \times \left(S_{ij,k}\right)^{\omega_S} \times \left(E_{ij,k}\right)^{\omega_E} \tag{4.8}$$

where C, S, and E represent contrast, saturation, and well-exposedness. The corresponding "weighting" exponents are denoted as ω_C, ω_S, and ω_E. The subscript ij,k refers to pixel (i,j) in the k-th image. As previously mentioned, due to the absence of colour in the dataset, the saturation component is not calculated, resulting in the following:

$$W_{ij,k} = \left(C_{ij,k}\right)^{\omega_C} \times \left(E_{ij,k}\right)^{\omega_E} \tag{4.9}$$

Weighted Fusion

To compute the weighted average along each pixel to fuse the N images, the weights computed from the quality measures are used, and, to obtain a consistent result, the values of the N weight maps are normalised such that they sum to one at each pixel (i, j) [53]:

$$\hat{W}_{ij,k} = \left[\sum_{k'=1}^{N} W_{ij,k'}\right]^{-1} W_{ij,k} \tag{4.10}$$

The resulting image R can then be obtained by a weighted blending of the input images:

$$R_{ij} = \sum_{k=1}^{N} \hat{W}_{ij,k} I_{ij,k} \tag{4.11}$$

with I_k the k-th input image in the sequence.

4.2.2 Lucky Imaging

Lucky imaging consists of selecting the best images from observation and combining them to produce an image with improved quality. Besides this, the image can be warped and then combined in order for the centroid of the stars to match between frames. Firstly, all the frames must be evaluated for their quality. This is done by identifying the reference star in the image (4.1.1), fitting a Gaussian (4.1.2) and appending the index of the respective frame to a list. Following this, the list of the indexes is reordered based on the amplitude, where the best frame is the one with the highest maximum amplitude of the reference star. From here, the top 10% of frames are appended to a new list. The percentage of frames used usually floats between 5% to 10% [54].

Having the best frames acquired, the next step consists of a shift-and-add operation for all the frames, with the deemed best frame as a reference. This is done to counteract the atmosphere's distortions effects by correcting the star's centroid position and overlapping both stars. Primarily, the stars are detected in the reference and to-be-shifted frames. As it was previously studied in Section 3.2, for good observations, the centroid exhibits a relatively low variation of approximately $< \pm 1$ pixel, while for lesser quality observations, it fluctuates more, reaching around $> \pm 2$ pixels. Since the broken pixels and other artifacts (such as extra reflections) are static between frames, the only metric required to match stars is the coordinates themselves, so if the distance between two stars is less than around 3 pixels, we can assume the two stars match.

Subsequently, the DLT algorithm (as detailed in Section 2.1.2) is implemented to calculate the homography matrix between the centroids of the matched stars. This matrix is then utilised to enforce a warping transformation on the image, thereby aligning the stars from both frames.

Ultimately, the resulting images are blended together, yielding a final image specific to each telescope. During this stage, both the median averaging and weighted fusion methods were evaluated. The key disparity between these two approaches lies in calculating and applying weights to the frames after the selection phase. The feature detection and matching steps are performed on the original frames, while the warping and stacking phases are applied to the weighted frames.

4.2.3 Drizzle

In this dissertation, a python library [55] provided by the Space Telescope Science Institute (STScl) and derived from the DrizzlePac is employed.

The algorithm uses the exposition time and the World Coordinate System (WCS) information, which provides the necessary data to establish a mapping between the pixel coordinates in the image and their corresponding celestial coordinates on the sky, to align the pixels, as illustrated in Figure 2.7, providing customisation for flux blending with parameters like pixfrac and different kernels.

To employ this library, the WCS and exposition time information has to be acquired from the header of the original fits file containing the raw data and input in a Drizzle class. As for the alignment of stars, the same algorithm is used as in the Lucky Imaging methodology. The first step is to identify the stars in the image (4.1.1), match the centroids, and calculate and apply the homography transformation to the frame. Finally, to execute the drizzle algorithm, the warped frames are iteratively added to the Drizzle class, producing a final reconstructed image.

4.3 Multi Telescope Image Stitching

To combine the images from the four telescopes, a traditional image stitching algorithm is employed, which is similar to the shift and add operation.

Firstly, the features are acquired using the DAOPHOT implementation described in 4.1.1. Following this, the stars must be matched between telescopes. Due to the nature of the telescopes, all the telescopes exhibit discernible variations in image quality. This makes it so that we can't compare the other features when matching stars, having to rely only on the coordinates as the features to be matched. This is done by organising both the tables containing the features detected by photutils (similar to the one presented in 4.1.1) by flux, which is quantified by measuring the intensity of light received from the star within a certain region or aperture on the image, meaning the brightest the star in the image has a bigger flux. This is done because the order of stars between telescopes and frames remains fairly consistent when ordered by flux.

Consequently, the star centroids are matched between the two frames based on the distance between the two coordinates (if the distance is less than 5 pixels, then it is a match). When a star is successfully matched, its coordinates are altered to a NaN (Not a Number) value to prevent subsequent matches, assuring the same star has only one match across both telescopes' images'. Besides this, a limit of matches is implemented to prevent over-fitting in the homography estimation step. In conjecture with the previously mentioned flux ordering technique, it allows for the brightest of stars (which we are the most robust in the image) to guarantee a solid match, preventing miss-matches and improving the results substantially. It's worth noting that this feature is also implemented in both lucky imaging methodologies, but it's addressed here due to the paramount difference it had in this step of the pipeline.

As previously mentioned in the analysis made of the dataset, Telescope 1 is an excellent candidate for being the reference frame due to the overall smaller sigmas in the frames captured by it. Consequential to this, the homography, which translates the relation between the coordinates of the stars between the two images, must be calculated for the remaining telescopes. This is done by taking advantage of the DLT algorithm again, where the estimated matrix is used to transform the image into one where the stars between telescopes are overlapping with respect to the reference telescope.

Finally, the warped images are stacked with the reference image and an averaging, giving equal weight to all four telescopes and allowing for an even distribution of the enhanced features, wielding a master image where all the telescopes are combined.

Chapter 5

Results and Discussion

This chapter presents the results obtained from the methods employed in this dissertation, which encompasses two crucial aspects of this research: Single Telescope Super Resolution and Multiple Telescope Image Stitching. The main objective of this chapter is to showcase the outcomes of approaches and to analyse the implications of these results in the context of this dissertation. In order to assess the quality and effectiveness of the images produced, it is important to employ objective metrics as well as subjective evaluations. This Chapter focuses on the evaluation of final images in the context of two key metrics: subjective evaluation and the acquired statistics for the main star of the image.

5.1 Single Telescope Super Resolution

In this section, the goal is to visually inspect the quality of the images by analysing if there is an enhancement in resolution and details in the observed objects while not introducing additional noise, such as ghosting effects. Additionally, stars and image statistics are compared to the raw data observation. Finally, for a fair representation of the acquired data, the displayed example file is GRAVI.2020-03-06T08_45_55.240, in concurrence with the statistics displayed in Section 3.2.

5.1.1 Baseline Analysis

Upon conducting a visual examination of the images, it becomes evident that the final images exhibit an enhancement in image quality when juxtaposed with the individual frames. Nevertheless, a notable degree of blurriness persists in the vicinity of the stars, primarily attributable to the averaging of diverse atmospheric disturbances that impinge upon the observations. Correspondingly, the sigma value of the principal star has exhibited an increment in relation to the mean value derived from all frames across the various telescopes employed. Furthermore, the centroid exhibits a congruence with the histogram pertaining to the reference star's x and y coordinates. Moreover, the distances and angles exhibit a remarkable alignment with the mean values derived from the unprocessed frames, as one would anticipate from the amalgamation of all frames captured during an observation.

Table 5.1: Brightest star statistics for the averaging method for all telescopes

Telescope	Centroid (x)	Centroid (y)	Sigma	Maximum Amplitude
1	128.864 ± 0.174	159.104 ± 0.159	1.532 ± 0.167	2690.251 ± 306.716
2	125.432 ± 0.158	160.030 ± 0.177	1.809 ± 0.168	1041.622 ± 97.245
3	125.988 ± 0.201	161.099 ± 0.206	1.783 ± 0.204	1531.517 ± 143.926
4	132.634 ± 0.144	157.878 ± 0.178	1.623 ± 0.162	2089.625 ± 214.095

Table 5.2: Image statistics for the averaging method for all telescopes

Telescope	Dist (2 brightest)	Ang (2 brightest)	Dist (2nd and 3rd)	Ang (2nd and 3rd)
1	56.649 ± 0.277	−27.657 ± 0.016	134.796 ± 0.229	−54.847 ± 0.015
2	55.859 ± 0.289	−27.698 ± 0.031	129.519 ± 0.249	−54.288 ± 0.006
3	56.342 ± 0.330	−27.729 ± 0.029	132.253 ± 0.265	−54.853 ± 0.005
4	54.102 ± 0.382	−27.084 ± 0.059	129.678 ± 0.308	−55.324 ± 0.013

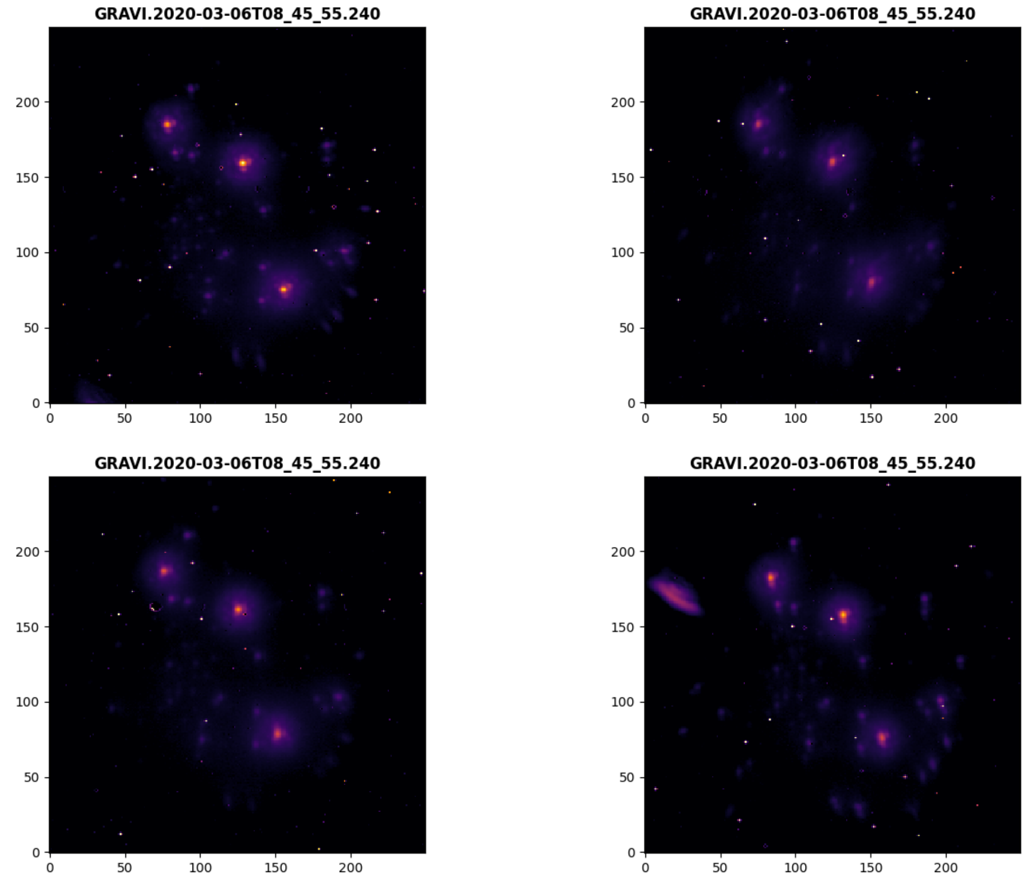

Figure 5.1: Combined images using averaging

5.1.2 Exposition Fusion

By employing the exposition fusion methodology, a noticeable refinement in the definition of stars becomes apparent when compared to the individual frames. Initially, the centroid of the main star of the produced image is coherent in both axis from what is to be expected to be the true positions of the final star. Unfortunately, the calculated distances and angles don't match the most likely values, likely due to the degradation of the quality of mid-brightness stars (2nd and 3rd stars).

Notably, while the maximum amplitude remains consistent with the mean maximum amplitude derived from all frames, a substantial decrease is observed in the sigma value. Initially, this reduction may appear favourable; however, upon closer examination of the final images, it becomes evident that the resulting stars exhibit diminished Gaussian characteristics. Consequently, two conclusions can be drawn. Firstly, the quality metrics and weight calculation employed have proven effective in enhancing crucial features within the image. Secondly, owing to atmospheric influences, the simple weight blending technique fails to mitigate distortions, resulting in stars that are excessively luminous but lack accuracy in their shapes.

A potential solution to this issue involves correcting the centroids between frames. This corrective measure ensures that the centres of the stars align, enabling the heavier features of the stars to correspond with one another across frames.

Table 5.3: Brightest star statistics for the exposition fusion method for all telescopes

Telescope	Centroid (x)	Centroid (y)	Sigma	Maximum Amplitude
1	128.766 ± 0.169	159.137 ± 0.145	1.159 ± 0.157	3944.889 ± 555.158
2	125.589 ± 0.164	160.421 ± 0.204	1.651 ± 0.185	1415.950 ± 157.214
3	125.717 ± 0.204	161.371 ± 0.263	1.346 ± 0.235	1839.318 ± 369.190
4	132.594 ± 0.152	157.727 ± 0.219	1.113 ± 0.189	2858.667 ± 506.046

Table 5.4: Image statistics for the exposition fusion method for all telescopes

Telescope	Dist (2 brightest)	Ang (2 brightest)	Dist (2nd and 3rd)	Ang (2nd and 3rd)
1	56.489 ± 0.574	-28.085 ± 0.011	134.714 ± 0.998	-54.922 ± 0.171
2	56.069 ± 0.648	-27.323 ± 0.118	129.724 ± 0.509	-54.394 ± 0.015
3	55.429 ± 0.643	-27.045 ± 0.081	132.291 ± 0.638	-54.738 ± 0.123
4	54.370 ± 1.089	-27.342 ± 0.341	129.349 ± 0.819	-54.888 ± 0.194

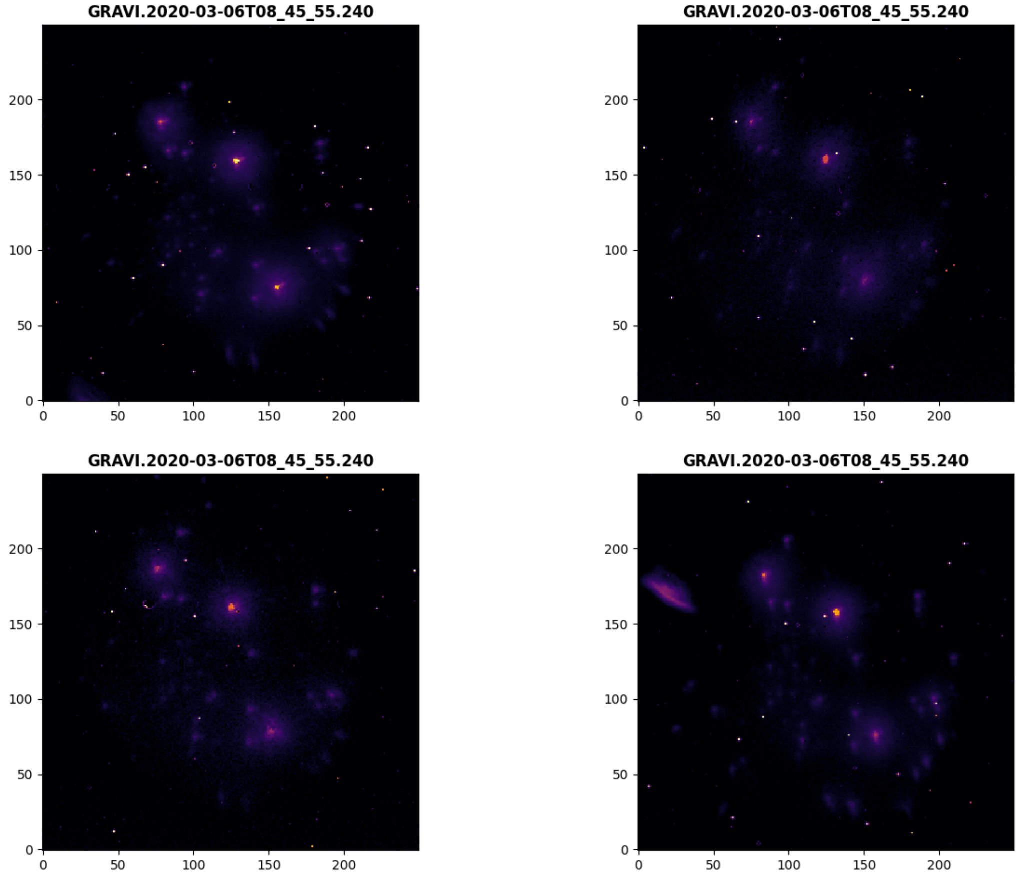

Figure 5.2: Combined images using exposition fusion

5.1.3 Lucky Imaging

Lucky imaging selects and combines only the sharpest frames, obtained during relatively stable atmospheric conditions.

Shift-and-Add

Upon initial visual inspection of the image, a distinct enhancement in resolution becomes evident. Compared to the baseline method of averaging, the previously observed blurring surrounding the stars has noticeably diminished, while the stars have retained their relative shape. From a statistical standpoint, although there are slight discrepancies in the amplitude values, they can be considered accurate in relative terms. Additionally, a discernible decrease in the sigma of the stars is observable, indicating an improvement in the overall quality of the stars. Regarding the positions of the stars, it is worth noting that while the x-axis does not align well with the histograms depicting the centroid positions, the y-axis exhibits a reasonable level of precision. Furthermore, both the distances and angles deviate from their respective means in relation to this observation. This can also be attributed to the shift-and-add operations, which use the frame with the deemed best exposure as reference, meaning that the resultant centroid-based statistics are influenced by their initial coordinates within the chosen frame.

Table 5.5: Brightest star statistics for the simple lucky imaging method for all telescopes

Telescope	Centroid (x)	Centroid (y)	Sigma	Maximum Amplitude
1	129.627 ± 0.115	159.914 ± 0.109	1.297 ± 0.112	184.746 ± 16.132
2	125.137 ± 0.094	160.586 ± 0.107	1.475 ± 0.101	77.880 ± 5.358
3	126.236 ± 0.150	161.833 ± 0.171	1.498 ± 0.161	112.618 ± 12.471
4	132.919 ± 0.103	157.428 ± 0.106	1.373 ± 0.105	134.123 ± 10.356

Table 5.6: Image statistics for the simple lucky imaging method for all telescopes

Telescope	Dist (2 brightest)	Ang (2 brightest)	Dist (2nd and 3rd)	Ang (2nd and 3rd)
1	56.695 ± 0.166	−26.543 ± 0.006	134.952 ± 0.193	−54.673 ± 0.009
2	54.872 ± 0.236	−27.264 ± 0.015	130.249 ± 0.175	−54.899 ± 0.004
3	55.639 ± 0.264	−26.621 ± 0.023	132.569 ± 0.192	−54.951 ± 0.007
4	54.973 ± 0.187	−27.350 ± 0.011	129.943 ± 0.158	−55.147 ± 0.001

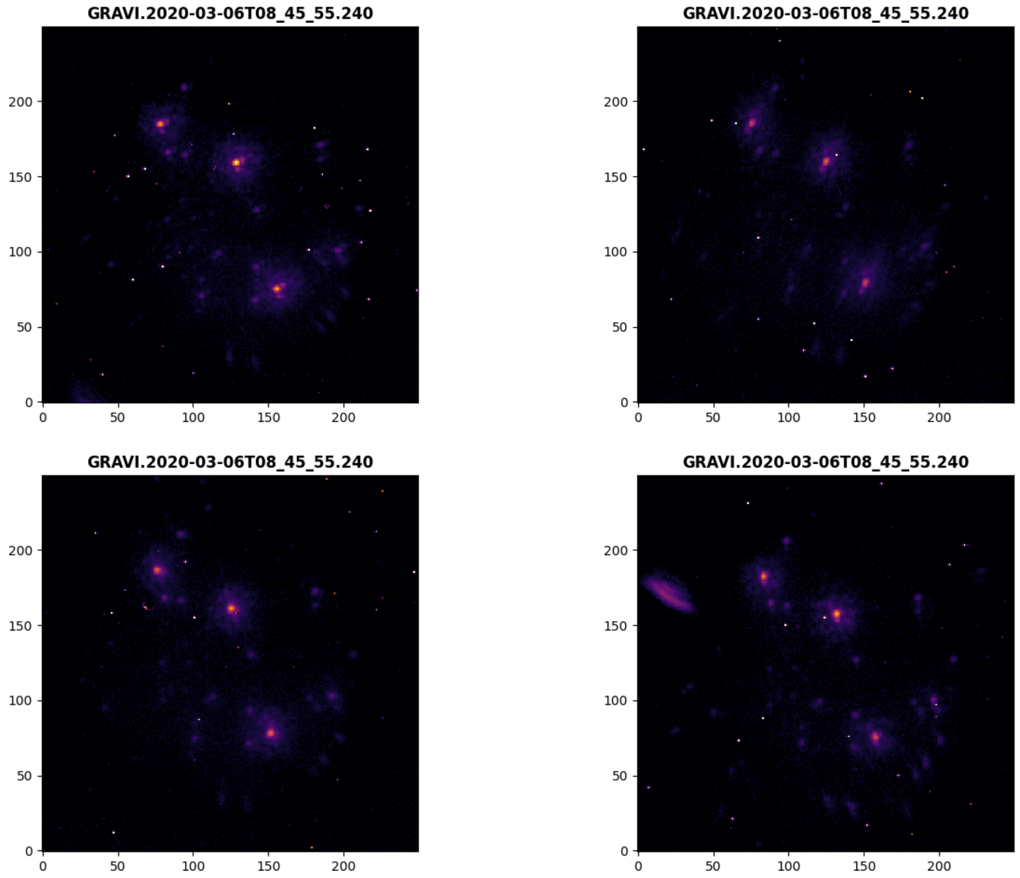

Figure 5.3: Combined images using simple Lucky Imaging

Weighted

In comparison to the previously analysed method, the final image exhibits an evident increase in resolution, resulting in reduced blurriness in the vicinity of the stars. When compared to alternative methodologies, a notable spike in the maximum amplitude is observed. This can be attributed to the concentration of heavier elements in the weight map centred on the star's centroid, which consequently leads to a decrease in sigma. Again, the dissimilarity between centroid-based statistics can be attributed, as addressed in the previous method, to the shift-and-add task, which uses a specific frame as a reference.

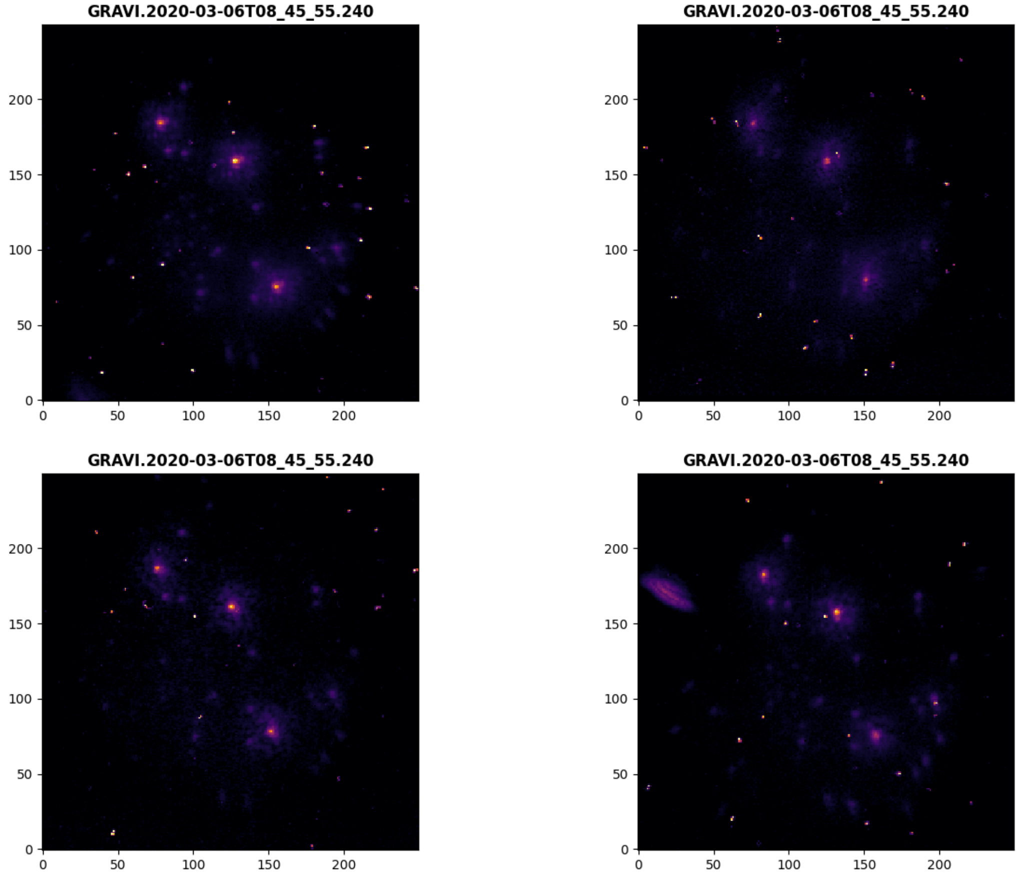

Figure 5.4: Combined images using weighted Lucky Imaging

Table 5.7: Brightest star statistics for the weighted lucky imaging method for all telescopes

Telescope	Centroid (x)	Centroid (y)	Sigma	Maximum Amplitude
1	129.792 ± 0.153	159.842 ± 0.142	1.149 ± 0.148	9269.929 ± 1199.837
2	125.247 ± 0.153	160.703 ± 0.173	1.420 ± 0.174	3536.878 ± 1199.837
3	126.322 ± 0.154	161.852 ± 0.161	1.367 ± 0.158	5765.614 ± 683.219
4	132.932 ± 0.127	157.438 ± 0.123	1.061 ± 0.125	8523.556 ± 1028.736

Table 5.8: Image statistics for the weighted lucky imaging method for all telescopes

Telescope	Dist (2 brightest)	Ang (2 brightest)	Dist (2nd and 3rd)	Ang (2nd and 3rd)
1	56.056 ± 0.288	-26.544 ± 0.012	133.856 ± 0.286	-55.031 ± 0.031
2	55.062 ± 0.437	-26.995 ± 0.058	130.221 ± 0.408	-54.421 ± 0.003
3	55.779 ± 0.315	-26.681 ± 0.021	133.163 ± 0.249	-54.842 ± 0.013
4	53.552 ± 0.356	-27.310 ± 0.037	130.213 ± 0.271	-55.245 ± 0.007

5.1.4 Drizzle

The implementation of the drizzle algorithm has yielded remarkable outcomes. Firstly, it has led to a noticeable enhancement in resolution, resulting in well-defined stars and minimal haziness in the vicinity of the main stars. Secondly, even the stars beyond the three brightest ones exhibit clear definitions, revealing some that appeared to be blended with others due to the proximity. From a statistical perspective, the sigma value of the stars has significantly decreased, further validating the sharpness and clarity of the stars in the final image. In terms of centroids, distances, and angles, the acquired values are fairly accurate to what is expected, although it uses the shift-and-add operation with the first frame of the observation as a reference.

It is worth highlighting that the amplitude values obtained through the drizzle algorithm differ considerably from other techniques employed in this dissertation. This disparity can be attributed to the resampling and combination of multiple images, a characteristic feature of the drizzle algorithm, which aims to augment the level of detail and sharpness. Consequently, such a process causes significant fluctuations in pixel values. This scaling approach is employed to optimise the visual representation of the image and strike a balance between detail and dynamic range.

Table 5.9: Brightest star statistics for the Drizzle method for all telescopes

Telescope	Centroid (x)	Centroid (y)	Sigma	Maximum Amplitude
1	128.975 ± 0.135	159.138 ± 0.113	1.248 ± 0.124	18.035 ± 1.923
2	125.743 ± 0.171	159.530 ± 0.206	1.533 ± 0.189	5.234 ± 0.660
3	126.022 ± 0.189	161.976 ± 0.178	1.443 ± 0.183	11.978 ± 1.705
4	132.938 ± 0.163	157.256 ± 0.148	1.155 ± 0.156	14.941 ± 2.022

Table 5.10: Image statistics for the Drizzle method for all telescopes

Telescope	Dist (2 brightest)	Ang (2 brightest)	Dist (2nd and 3rd)	Ang (2nd and 3rd)
1	56.603 ± 0.194	-27.217 ± 0.005	134.043 ± 0.169	-54.274 ± 0.011
2	54.967 ± 0.530	-26.631 ± 0.155	128.146 ± 0.361	-54.173 ± 0.013
3	56.159 ± 0.247	-27.494 ± 0.016	132.388 ± 0.207	-54.731 ± 0.009
4	54.420 ± 0.290	-27.344 ± 0.016	128.883 ± 0.252	-55.059 ± 0.002

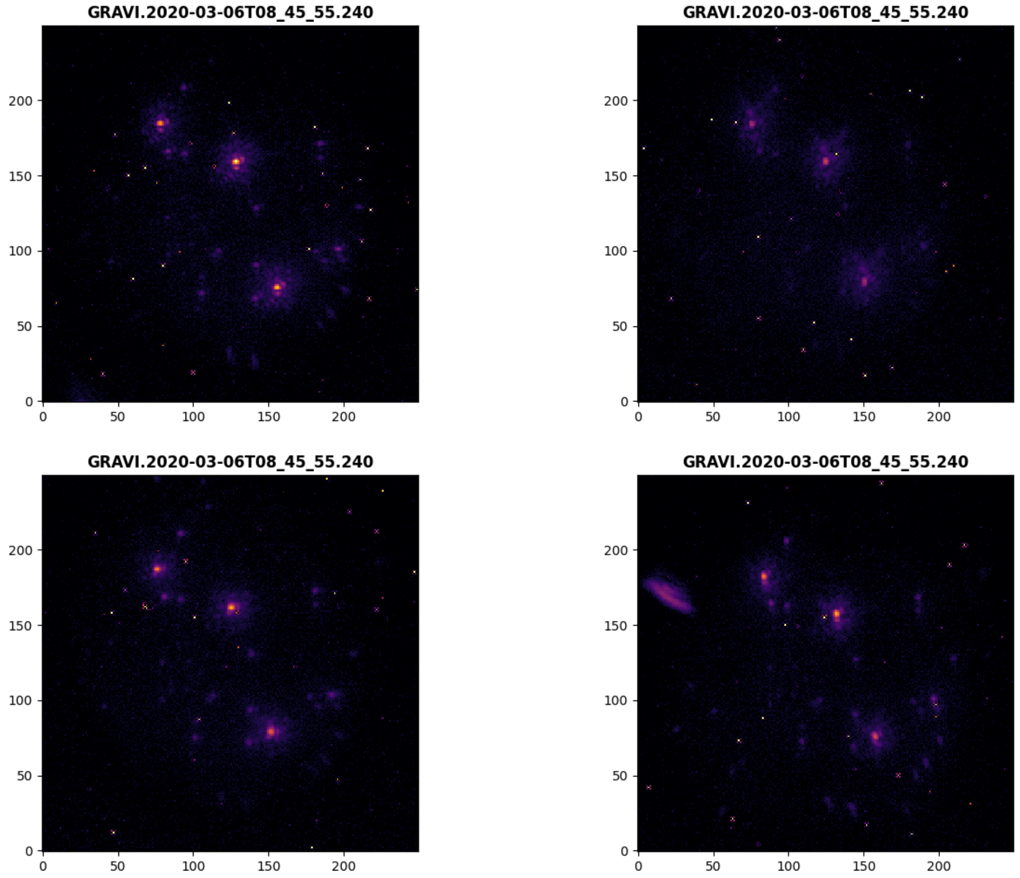

Figure 5.5: Combined images using the Drizzle algorithm

5.1.5 Discussion

The analysis of the results obtained from the various image enhancement methodologies provides valuable insights into their effectiveness and limitations in improving the resolution and quality of astronomical images. Each method demonstrated unique characteristics and exhibited varying degrees of success in mitigating atmospheric disturbances. The statistical analysis allows for a direct comparison between the different image enhancement methodologies. The centroid measurements provide insights into the accuracy of star alignment, while the sigma values reflect the degree of blurriness or definition of the stars. Additionally, the analysis of distances and angles offers information about the overall quality and fidelity of the enhanced images. The averaging and exposition fusion methodologies demonstrate precise alignment in centroid accuracy, as the centroids closely match the expected positions. However, the methodologies that employ the shift-and-add operation show a slight deviation in centroid measurements, except for the drizzle algorithm, which again achieves a high level of accuracy. This deviation from the other methodologies can be attributed to the choice of the reference frame for alignment. Regarding the sigma values, all methodologies except for averaging exhibit a reduction, indicating an improvement in star definition. The decrease in sigma suggests that the stars are better defined and exhibit less blurring. However, the averaging technique shows an increase in sigma, which can be attributed to the blurring observed in the resulting images. When considering the distances and angles between stars, both the drizzle and averaging methodologies align closely with the expected values. This indicates that the stars in the enhanced images maintain their relative positions accurately. However, both lucky imaging algorithms deviate slightly from the expected values, which again can be attributed to the choice of the reference frame. In contrast, the methodology of exposition fusion demonstrates a discernible disparity in relation to alternative methodologies in cases of deteriorated stars, such as the second and third stars, which exhibits diminished overall quality in comparison to its counterparts. This discrepancy suggests a deficiency in the augmentation of the second and third stars.

Finally, a subjective analysis was also done, starting with the baseline method of averaging shows a slight improvement in resolution compared to individual frames. However, the resulting images still suffer from blurriness, especially around the stars. Exposition fusion refines the definition of stars compared to individual frames but compromises the Gaussian characteristics. The resulting stars appear excessively luminous and have inaccuracies in their shapes. Simple lucky imaging demonstrates a notable enhancement in resolution and reduces blurring around the stars. The overall accuracy and quality of the stars improve. Weighted lucky imaging further increases resolution and reduces blurriness. By concentrating on heavier elements, the maximum amplitude of the stars increases. The implementation of the drizzle algorithm yields remarkable outcomes by enhancing resolution and producing well-defined stars with minimal haziness, with the overall sharpness and clarity of the stars significantly improving. The algorithm's approach to resampling and combining multiple images strikes a balance between detail and dynamic range, resulting in an optimised visual representation of the image.

The statistical analysis provides a quantitative basis for comparing the different image enhancement methodologies. The centroid measurements highlight the accuracy of star alignment, while the sigma values indicate the level of star definition. The analysis of distances and angles offers insights into the overall fidelity of the enhanced images. Based on these comparisons, the drizzle algorithm consistently demonstrates superior results in terms of centroid accuracy, sigma reduction, and maintaining accurate distances and angles between stars. Furthermore, it is the most effective in improving the resolution and quality of astronomical images. The other methodologies show certain enhancements but struggle to fully mitigate atmospheric disturbances and achieve optimal results, as evidenced by increased sigma values and discrepancies in star positions.

Table 5.11: Comparison of the reference star statistics for the different methods (Telescope 1)

Method	Centroid (x)	Centroid (y)	Sigma	Maximum Amplitude
Averaging	128.864 ± 0.174	159.104 ± 0.159	1.532 ± 0.167	2690.251 ± 306.716
EF	128.766 ± 0.169	159.137 ± 0.145	1.159 ± 0.157	3944.889 ± 555.158
Simple LI	129.627 ± 0.115	159.914 ± 0.109	1.297 ± 0.112	184.746 ± 16.132
Weighted LI	129.792 ± 0.153	159.842 ± 0.142	1.149 ± 0.148	9269.929 ± 1199.837
Drizzle	128.975 ± 0.135	159.138 ± 0.113	1.248 ± 0.124	18.035 ± 1.923

Table 5.12: Comparison of image statistics for the different methods (Telescope 1)

Method	Dist (2 brightest)	Ang (2 brightest)	Dist (2nd and 3rd)	Ang (2nd and 3rd)
Averaging	56.649 ± 0.277	-27.657 ± 0.016	134.796 ± 0.229	-54.847 ± 0.015
EF	56.489 ± 0.574	-28.085 ± 0.011	134.714 ± 0.998	-54.922 ± 0.171
Simple LI	56.695 ± 0.166	-26.543 ± 0.006	134.952 ± 0.193	-54.673 ± 0.009
Weighted LI	56.056 ± 0.288	-26.544 ± 0.012	133.856 ± 0.286	-55.031 ± 0.031
Drizzle	56.603 ± 0.194	-27.217 ± 0.005	134.043 ± 0.169	-54.274 ± 0.011

5.2 Multi Telescope Image Stitching

To conduct a comprehensive examination of the outcomes obtained from the ultimate image stitching procedure, like in the previous section, an examination of both the final image quality and statistics is performed. Here, the goal is for the statistics throughout the dataset to remain as consistent as possible with minimal variations between observations. Considering centroid-based statistics, shifting the focus from an analysis encompassing the entire dataset to a targeted evaluation of specific files is necessary. This approach ensures that the analysis pertains solely to observations conducted on the same day, with consistent orientation and a continuous sequence of data. Therefore, this section will concentrate on the master images and associated statistics obtained during the observation period spanning from 8:31 to 9:39 on the 6th of March, 2020.

Owing to the absence of a technique to eliminate defective pixels and other artefacts, such as reflections, in the acquisition camera, the resultant master image inevitably contains a discernible level of noise stemming from the combined noise of all the telescopes involved. Despite this inherent noise, image stitching remains feasible. Consequently, it becomes possible to enhance the evaluation of the outcomes derived from the multi-frame super-resolution methods employed for individual telescope images. This is primarily attributed to the pronounced disparities observed among the master images originating from identical observations, thereby enabling a more comprehensive assessment.

5.2.1 Baseline Analysis

Upon examining the final stitched image, it becomes evident that the quality of the composite image exhibits enhancements compared to its constituent individual parts. The stars dispersed throughout the image are clearly defined, and compared, thereby contributing to an overall improved visual output. Nevertheless, an issue arises in the form of increased noise surrounding the star region. This heightened noise is attributed to the amalgamation of blurring effects around the vicinity of each star, as previously highlighted.

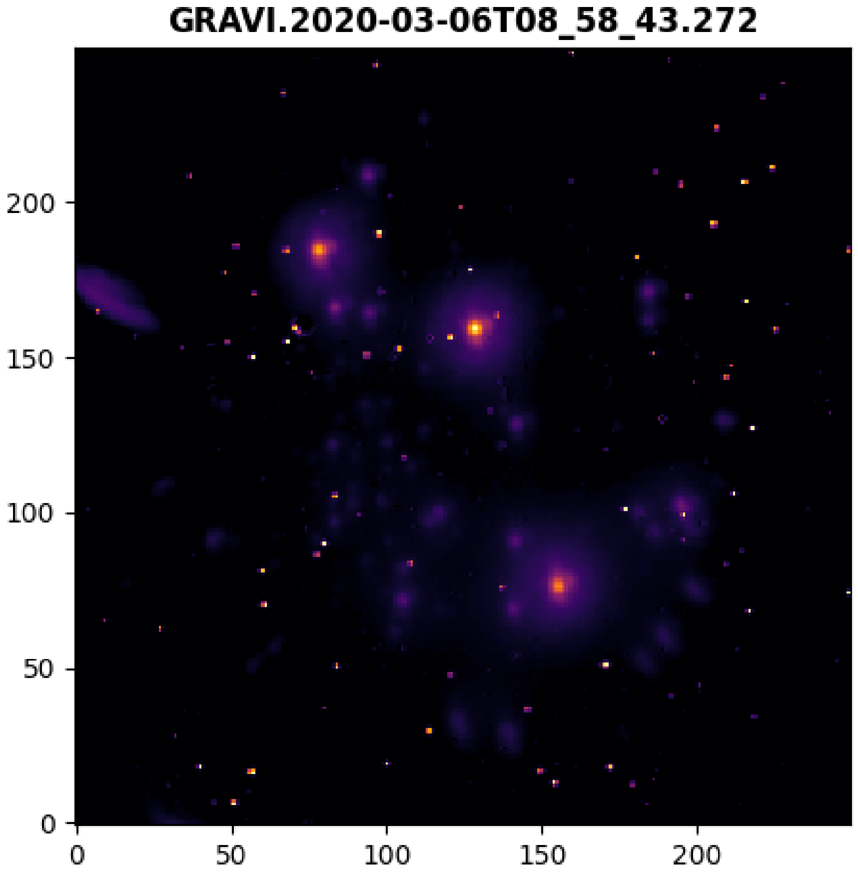

Figure 5.6: Master Image based on averaging

5.2.2 Exposition Fusion

Consistent with the unsatisfactory outcomes arising from the multi-frame image reconstruction phase, the master image does not show improvement. When it comes to high-quality observations, there is an improvement in resolution due to the better-defined features of the image. But for mid to low-quality observations, the results are inferior to the benchmark. Notably, the stars that are typically regarded as inconspicuous appear poorly defined. Only the stars surrounding the principal ones, which are usually overshadowed by their sheer brightness, exhibit improved visibility. Unfortunately, the brightest stars exhibit distorted forms, resulting from the loss of Gaussian features from the previous step.

Upon conducting a comprehensive analysis of the data, it becomes evident that the distribution of centroid-based statistics in both axes is worse compared to the baseline. Additionally, while the sigma shows a decrease, both the sigma and amplitudes seem more unstable throughout observations. Finally, in the case of the observations where the quality is subpar, these methods showed even more underwhelming results.

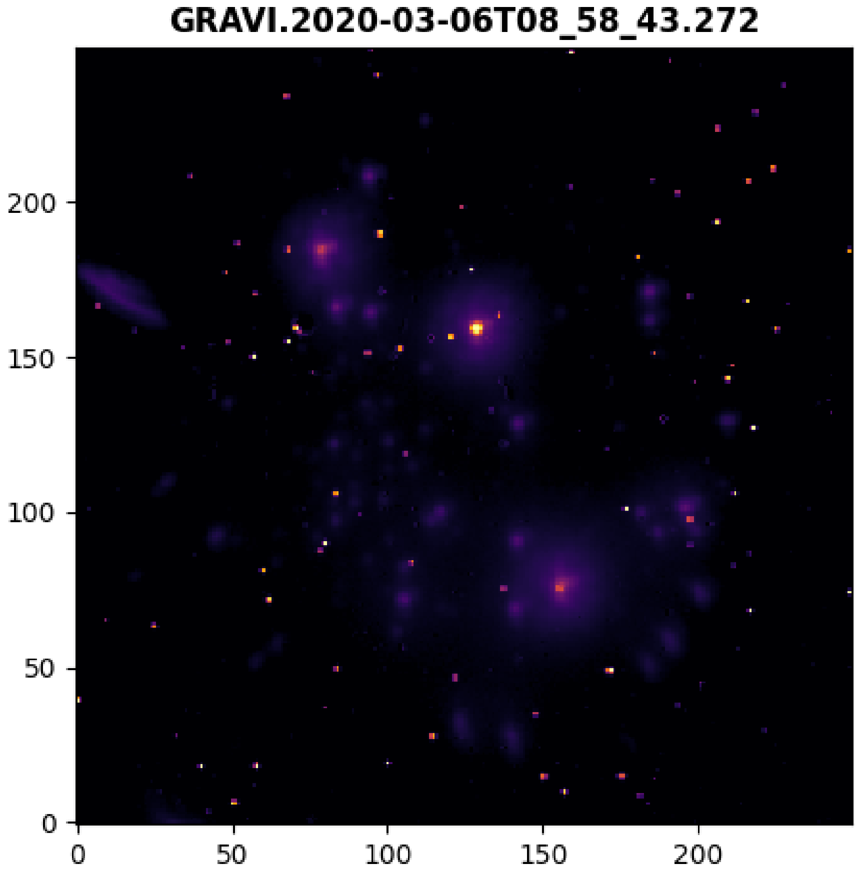

Figure 5.7: Master image based on Exposition Fusion

5.2.3 Lucky Imaging

Add-and-Shift

In contrast to the benchmark method of averaging, the add-and-shift lucky imaging technique yielded a master image characterised by an improved definition of celestial objects and reduced blurring. Notably, when considering the centroid of the reference star, the distribution in both axes and the corresponding distances and angles show an improvement. Moreover, a reduction in both the sigma and its distribution throughout the whole dataset is clear, indicating a level of progress in combating the atmospheric effects in the images.

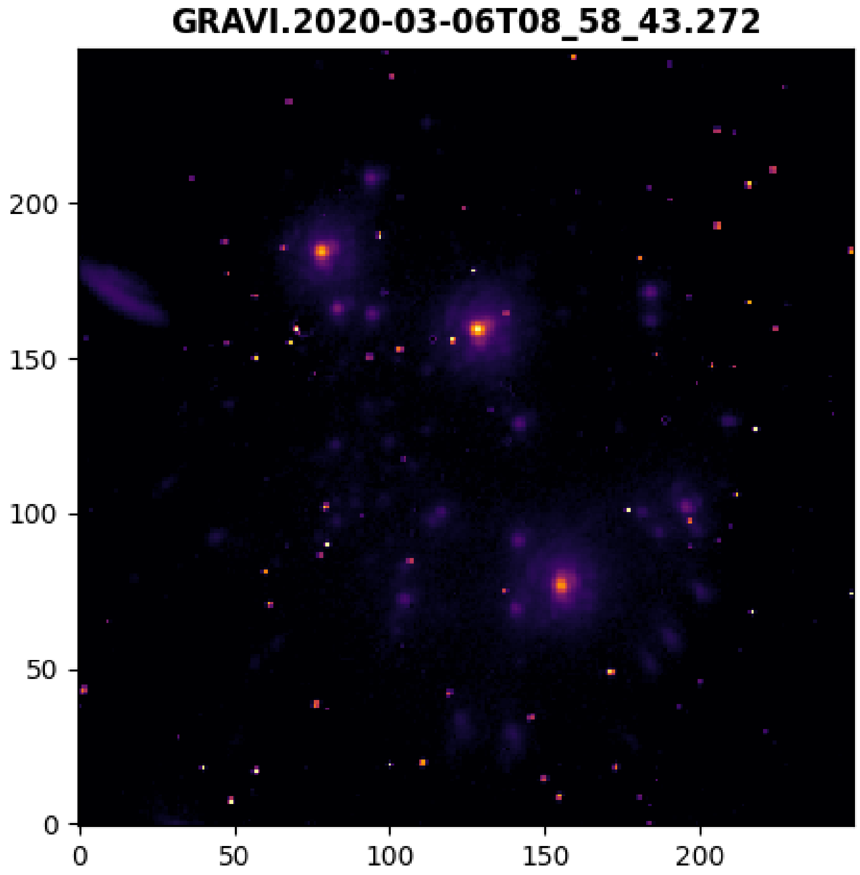

Figure 5.8: Master image based on simple lucky imaging

Weighted

In comparison to the unweighted variant of the fortunate imaging technique, the weighted version yields a master image that exhibits enhanced levels of definition of the brightest stars. Notably, the presence of blur surrounding the stars is significantly diminished, thus showcasing increased clarity and sharpness. In contrast to this, mid to low-brightness stars suffer from a reduction in definition. Also, due to the many broken pixels and the weighted shift-and-add operation, more noise is introduced with the warping of the pixels, reinforcing the necessity of a technique to correct or mask the broken pixels in the image.

Regarding statistical analysis, this methodology shows impressive results. Both sigma and centroid-based stats demonstrate a reduction in the distribution between observations compared to other methods, namely in mid to high-quality observations. For observations that have worsened quality, the results are inferior and not as consistent as other methods.

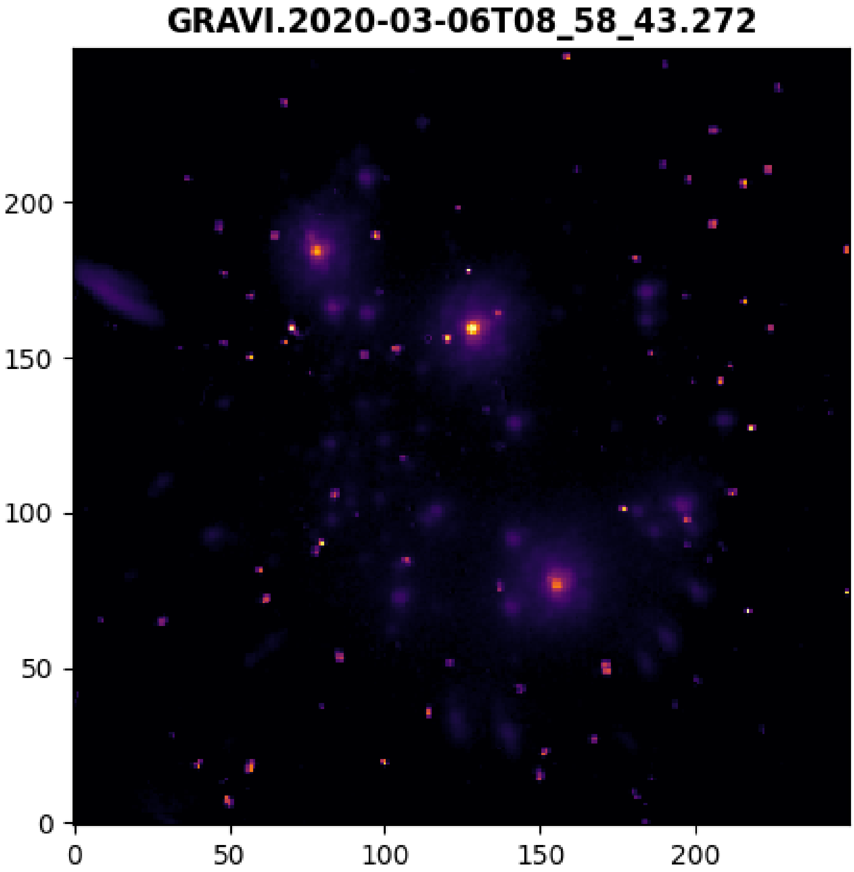

Figure 5.9: Master image based on weighted lucky imaging

5.2.4 Drizzle

The drizzle algorithm has demonstrated remarkable advancements compared to alternative methods, as evidenced by the notable enhancements observed in the resulting master image. The brightest stars are now clearly delineated, with the previously encountered haziness, caused by their luminosity significantly diminished. Additionally, despite their limited visibility in the displayed image, the faintest stars remain discernible, exhibiting substantially reduced blurring and thus showcasing improved resolution.

Furthermore, when examining the characteristics of both the image and the reference star, a commendable equilibrium is observed in the distribution of centroid-based statistics, including position, distances, and angles. These statistics are thoughtfully balanced with the sigma of the brightest star, resulting in a well-distributed flux throughout the image without excessively overwhelming the overall brightness.

Given its evident superiority among the various multi-frame image super-resolution techniques, it comes as no surprise that the master images generated through the employment of this method yield the most optimal and consistent outcomes based on the significant difference in quality between observations.

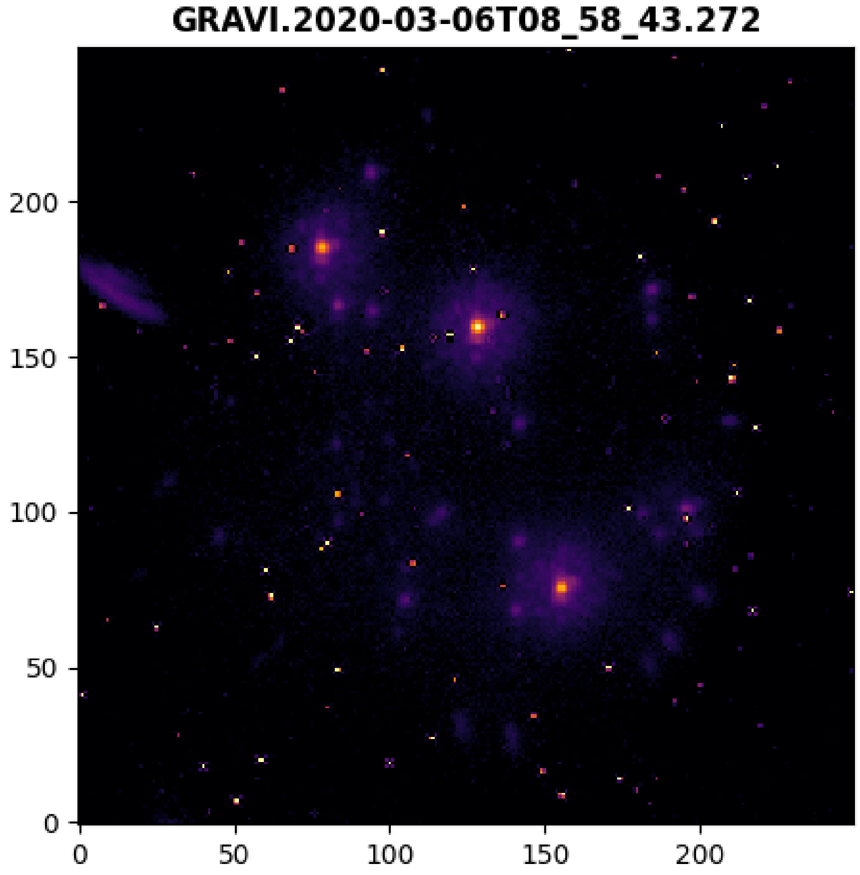

Figure 5.10: Master image based on drizzle algorithm

5.2.5 Discussion

After conducting a statistical analysis of the different methodologies employed in this dissertation, it is evident that several algorithms showed improvements in centroid-based statistics compared to the benchmark. Among them, the drizzle algorithm demonstrated the highest degree of consistency, while the exposition fusion algorithm exhibited lower consistency across varying observation qualities. The lucky imaging algorithms also displayed clear enhancements, although there was a decrease in performance for the poorest quality observations. Notably, the drizzle algorithm demonstrated a balanced reduction in sigma and consistent results across observations, whereas the exposition fusion algorithm exhibited the least consistency. Both weighted and unweighted lucky imaging techniques yielded satisfactory and consistent results.

From a subjective standpoint, the various multi-frame super-resolution methods used in this dissertation presented varying levels of success in enhancing the quality and definition of the final stitched images. The Averaging (benchmark) technique improved the visual output, particularly in star definition, but introduced increased noise due to blurring effects. Exposition Fusion enhanced the resolution and visibility of stars yet caused distortion in the main stars and yielded worse centroid-based statistics and sigma distribution compared to the baseline. Simple Lucky Imaging provided improved definition and reduced blurring, showing progress in mitigating atmospheric effects with better centroid-based statistics and decreased sigma. Weighted Lucky Imaging, compared to the unweighted variant, further enhanced definition and reduced blur, particularly in mid to better-quality observations, but displayed less consistency in lower-quality observations and worsen the noise created by broken pixels. The Drizzle algorithm showcased remarkable advancements by reducing luminosity-induced haziness and improving resolution, exhibiting commendable centroid-based statistics and sigma distribution throughout the image.

In conclusion, this dissertation's multi-telescope stitching algorithm yielded good results in most cases. However, it is important to mention that for images with the worst quality, the results were subpar.

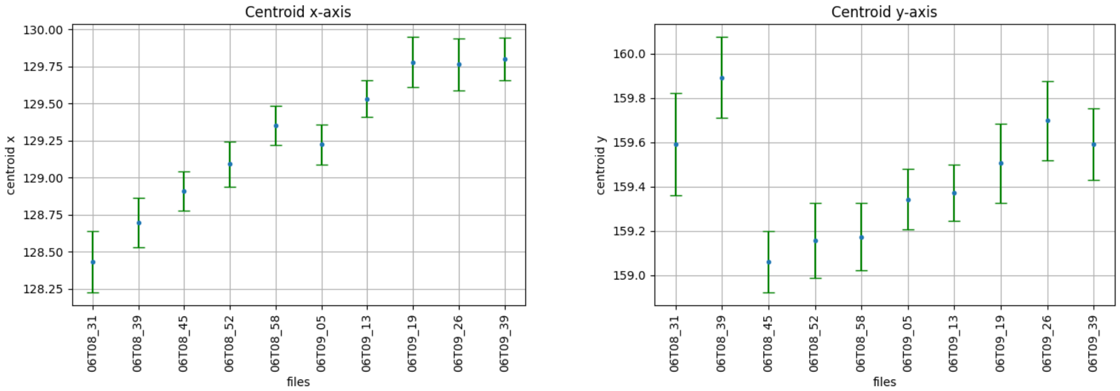

(a) Centroid x axis (b) Centroid y axis

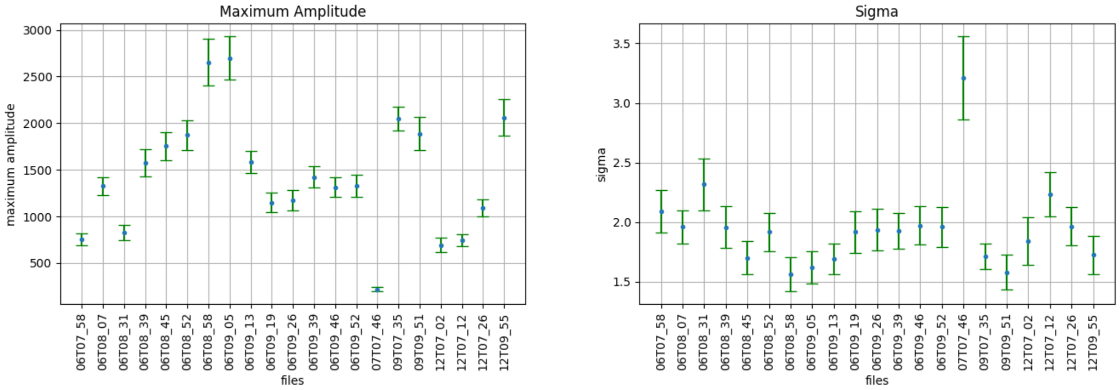

(c) Maximum Amplitude (d) Sigma

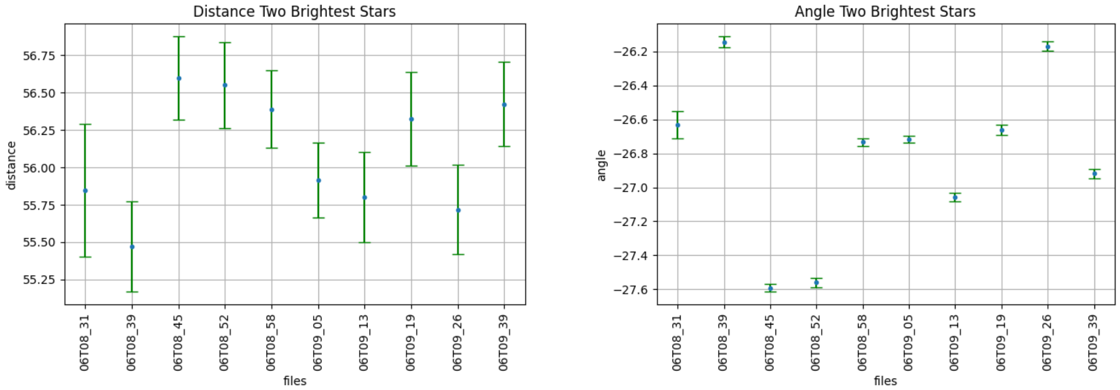

(e) Distance between the two brightest stars (f) Angle between the two brightest stars

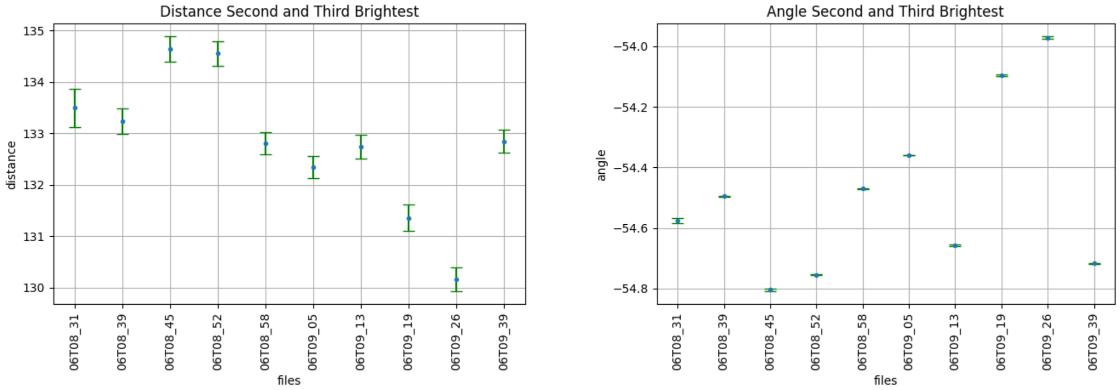

(g) Distance between the 2nd and 3rd brightest stars (h) Angle between the 2nd and 3rd brightest stars

Figure 5.11: Stats for the master image using averaging

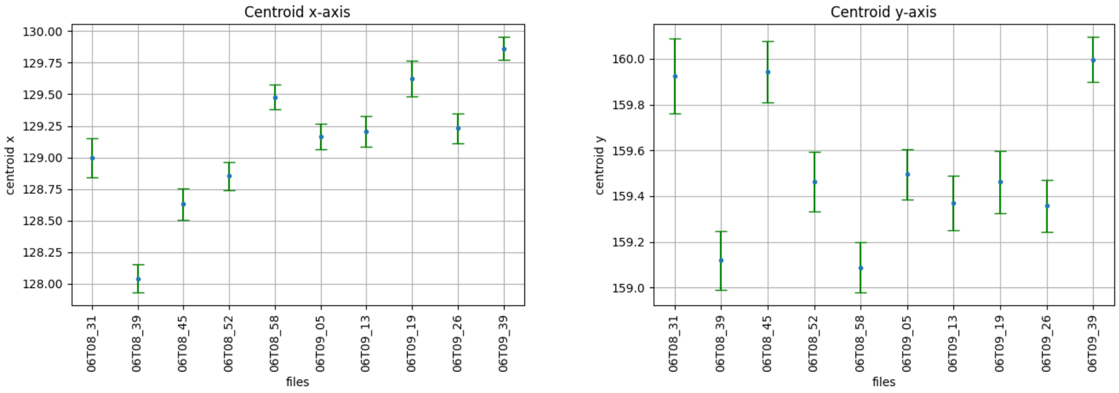

(a) Centroid x axis (b) Centroid y axis

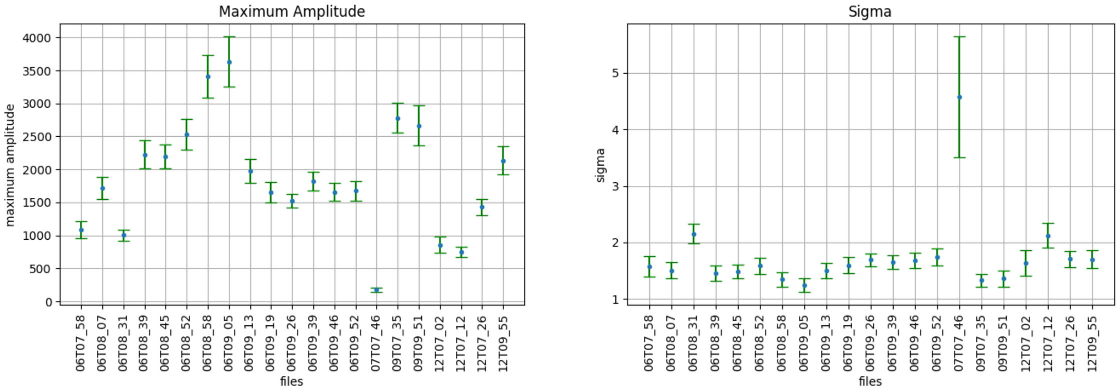

(c) Maximum Amplitude (d) Sigma

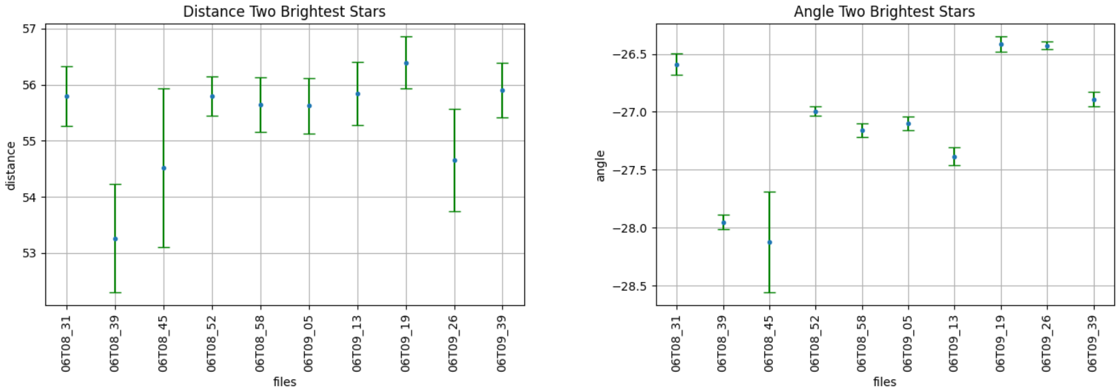

(e) Distance between the two brightest stars (f) Angle between the two brightest stars

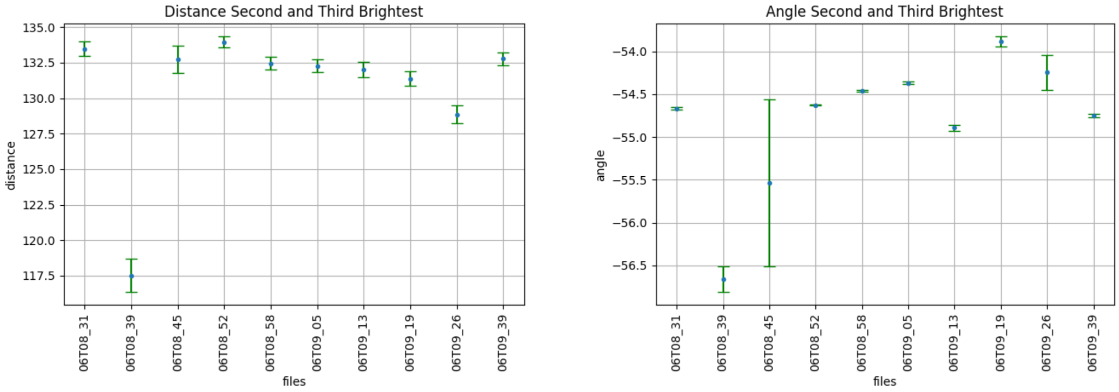

(g) Distance between the 2nd and 3rd brightest stars (h) Angle between the 2nd and 3rd brightest stars

Figure 5.12: Stats for the master image using exposition fusion

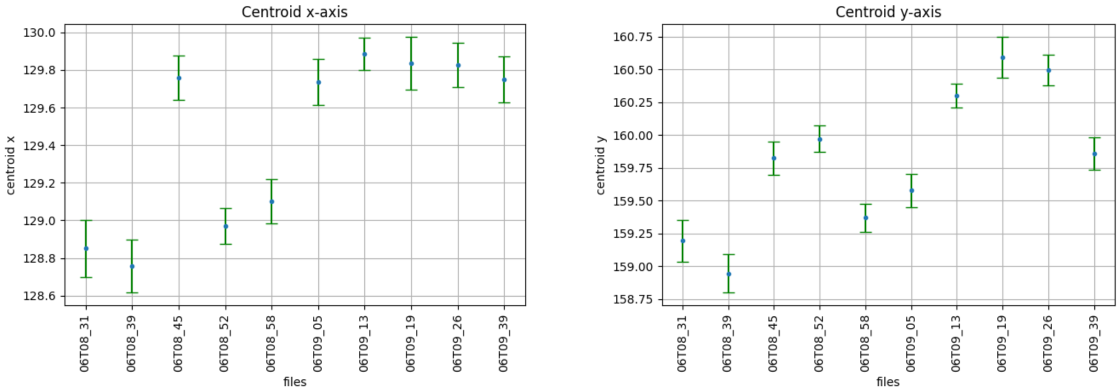

(a) Centroid x axis (b) Centroid y axis

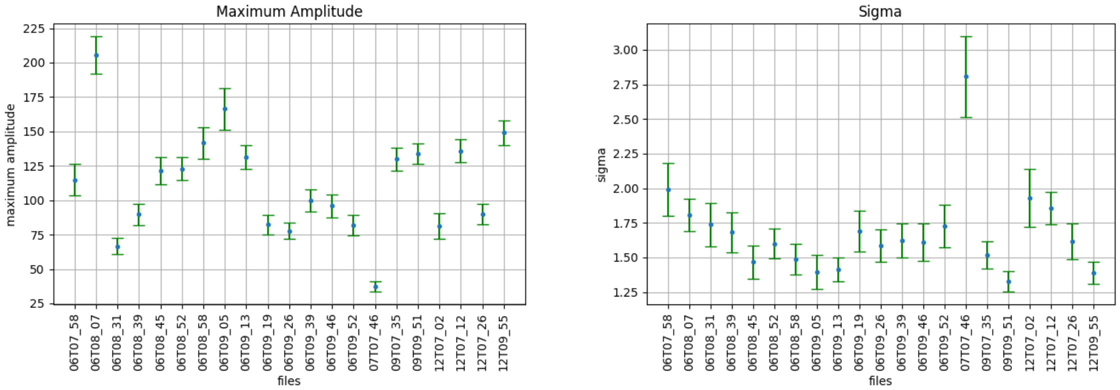

(c) Maximum Amplitude (d) Sigma

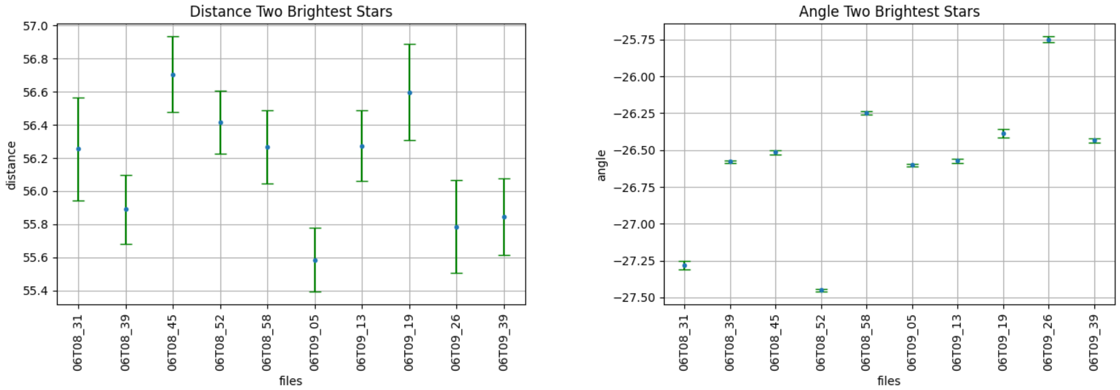

(e) Distance between the two brightest stars (f) Angle between the two brightest stars

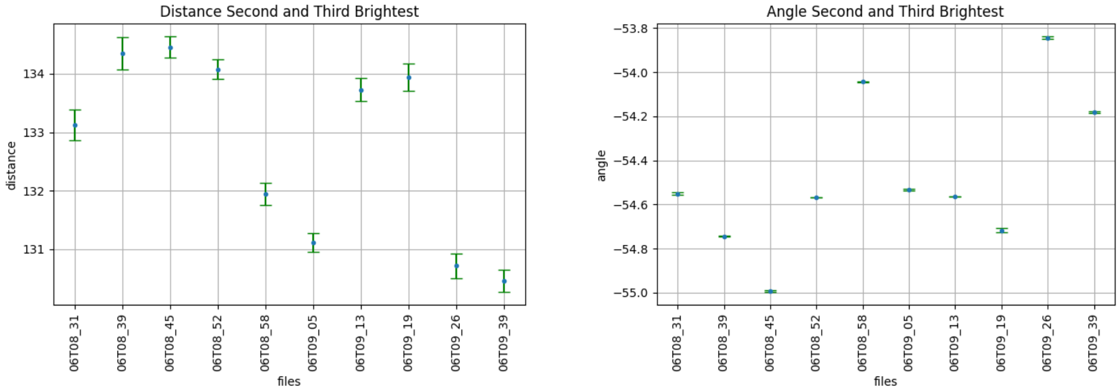

(g) Distance between the 2nd and 3rd brightest stars (h) Angle between the 2nd and 3rd brightest stars

Figure 5.13: Stats for the master image using simple lucky imaging

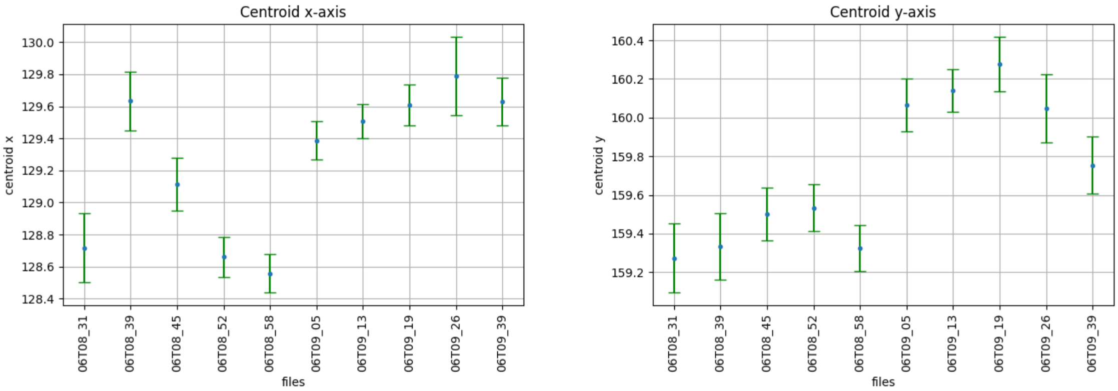

(a) Centroid x axis (b) Centroid y axis

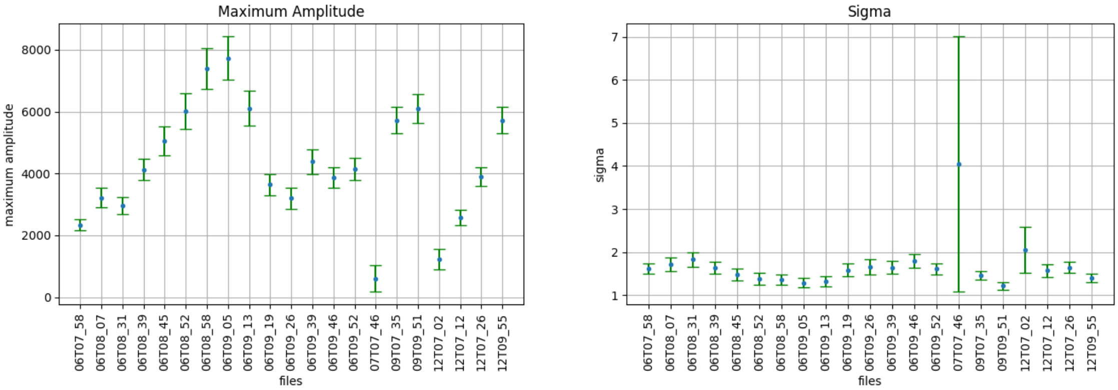

(c) Maximum Amplitude (d) Sigma

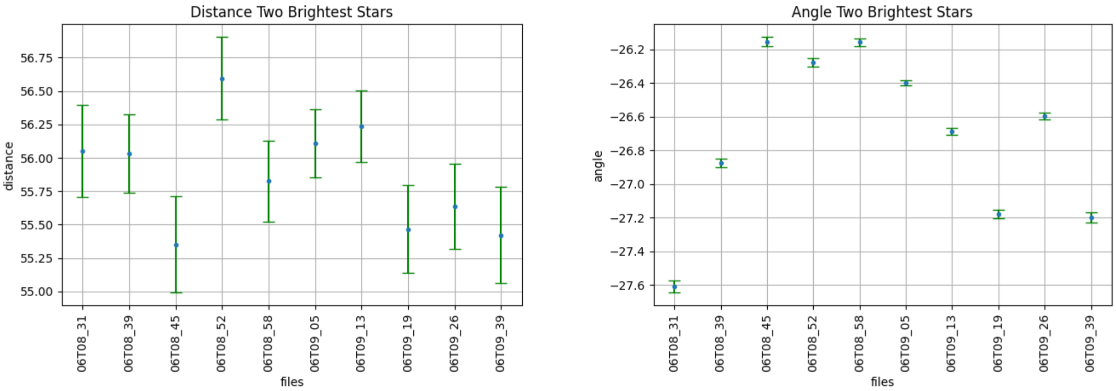

(e) Distance between the two brightest stars (f) Angle between the two brightest stars

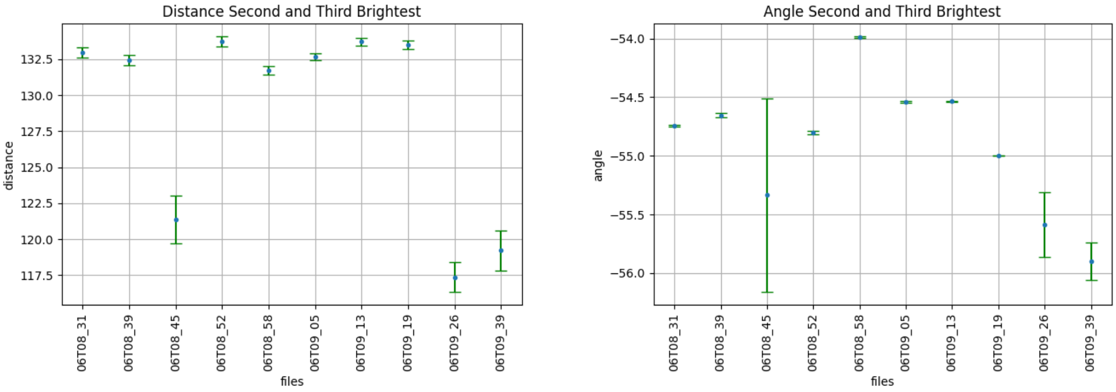

(g) Distance between the 2nd and 3rd brightest stars (h) Angle between the 2nd and 3rd brightest stars

Figure 5.14: Stats for the master image using weighted lucky imaging

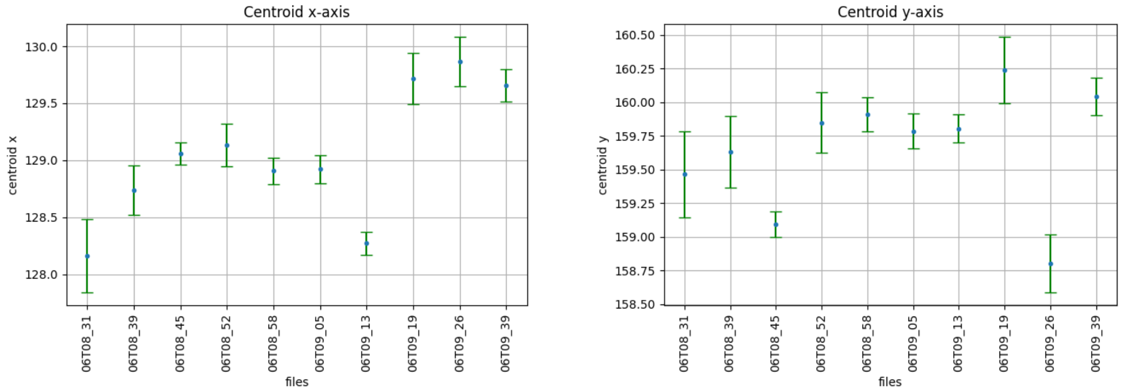

(a) Centroid x axis

(b) Centroid y axis

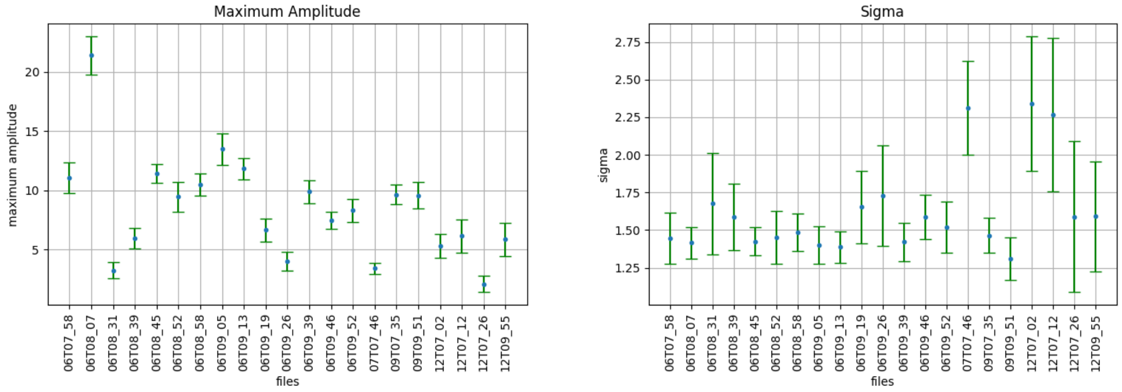

(c) Maximum Amplitude

(d) Sigma

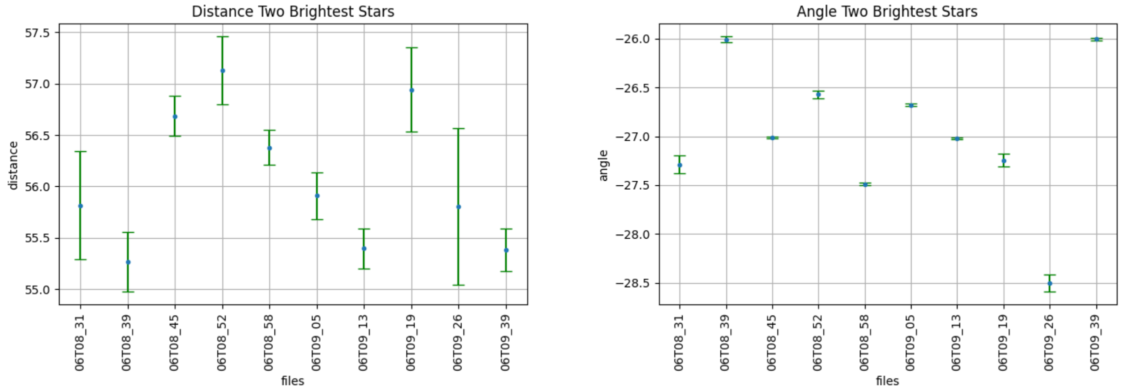

(e) Distance between the two brightest stars

(f) Angle between the two brightest stars

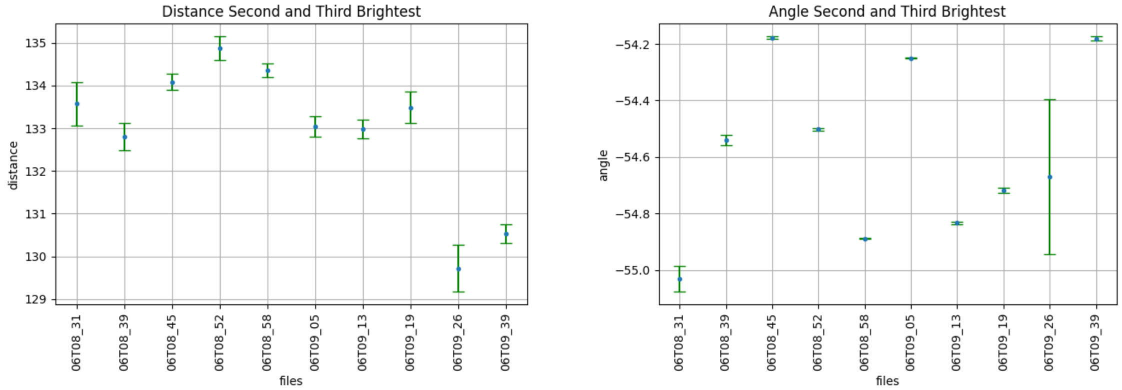

(g) Distance between the 2nd and 3rd brightest stars

(h) Angle between the 2nd and 3rd brightest stars

Figure 5.15: Stats for the master image using drizzle algorithm

Chapter 6

Conclusions and Future Work

6.1 Conclusion

The aim of this dissertation is to explore the application of machine vision techniques to enhance the quality of images affected by atmospheric effects. Specifically, the objective is to generate a master image with improved quality by mitigating the systematic effects caused by the atmosphere. To achieve this aim, several key objectives were pursued throughout the research. Firstly, various techniques for solutions for various complications were undertaken, considering both single-telescope and multi-telescope scenarios. Next, a comprehensive investigation was conducted to identify the systematic effects introduced by the atmosphere present in the dataset acquired by GRAVITY. Following this, different machine vision-based approaches were introduced and compared as possible solutions to the problem. Finally, the proposed methods were rigorously evaluated in terms of their quality and performance. Through a comprehensive assessment, the effectiveness of the developed techniques was analysed, providing insights into their strengths and limitations.

In conclusion, we are able to achieve the pre-defined goals in this dissertation:

Identify the systematic effects of the atmosphere and other artefacts on the images acquired by GRAVITY.

These effects are caused by the diffraction of light in different patches of molecules in the atmosphere. The diffraction makes the photons change direction, not allowing them to hit their intended spot. This causes for the observed light to appear to be hazed, forming a point spread function that resembles a Gaussian function, making the star also appear to change position and intensity over time. In addition, there is also the problem of broken pixels in the detector and other reflections that can prove troublesome in the feature acquisition stage.

The analysis of various factors, including centroid positions, histogram distributions, sigma values, maximum amplitudes, distances, and angles in the observed frames, provides valuable insights into the image quality and the impact of atmospheric effects on the observations. The precision of centroid estimation is more reliable in frames with better quality, while lower quality frames exhibit greater fluctuations, indicating the influence of atmospheric effects on the observations. The histogram distributions of centroid positions follow a normal distribution, suggesting that the centroid values align with the expected behaviour, with a peak around the likely true centroid position. The consistency in centroid variation across all telescopes suggests that the atmospheric distortion effect is relatively uniform among them. An inverse relationship between maximum amplitude and sigma values is observed, indicating that frames with larger amplitudes, likely due to better exposure, tend to have better-defined stars. This relationship serves as a quality metric for frame selection. Notably, Telescope 1 stands out as a potential reference telescope for image fusion due to its lower sigma values and better-defined star profiles. The sigma and maximum amplitude values can also be utilised as metrics to calculate weights, optimising the fusion process. Analysing the distances and angles between the two brightest stars provides information about their relative positions and the influence of atmospheric effects on the image. The observed normal distribution in the histogram reinforces the idea that atmospheric effects are consistent throughout the image. The consistent mean in distances and angles indicates a stable configuration of the two brightest stars, except in a subset of frames with altered orientations. The variability in the distance between the second and third brightest stars can be attributed to the lower quality or diminished visibility of the third brightest star.

Analysis of techniques for both the single-telescope and multi-telescope image stitching challenges.

Starting with the feature detection analysed techniques, the iLog method is capable of detecting blobs of varying sizes and orientations and incorporates iterative filtering, which enhances the accuracy and precision of blob detection, resulting in more reliable and consistent results and scale determination is reliable and adaptive, as it finds the value of σ that yields the highest response in scale-space. This makes it robust and adaptable to various scenarios. these are important characteristics when identifying stars in images affected by atmospheric effects. Furthermore, within the context of the state-of-the-art exploration, the Direct Linear Transform (DLT) algorithm was addressed, which plays a crucial role in calculating the homography matrix between two distinct frames or telescope images. The purpose of this algorithm is to facilitate the matching of centroids during the process of image stitching. Moreover, the investigation has explored various fusion methods available in the field of image fusion. The exploration of these diverse techniques aims to provide a comprehensive understanding of the different approaches and inspire future research endeavours.

The chapter is finalised by an analysis of different super-resolution methods. Firstly, an insight into Adaptive Optics due to the relevance in correcting aberrations and enhancing image quality, this is followed by a discussion on frequency-based super-resolution, lucky imaging and the drizzle algorithms, which showed to be good candidates for a solution to perform single telescope super-resolution. Here, the drizzle algorithm and lucky imaging methodologies emerge as promising techniques which are employed in this dissertation.

It's also worth noting that, in the research of possible solutions for both single telescope super-resolution and multi-telescope image fusion, machine learning-based methodologies were deliberately integrated, incorporating diverse elements that exhibit potential for inspiring future research.

Compare machine vision-based approaches to stitch the different images into a master image

This dissertation explores various methodologies for achieving single telescope super-resolution, while also establishing a baseline for result comparison. The four methods investigated in this study encompass exposition fusion, lucky imaging, and a hybrid approach combining elements from both aforementioned techniques. Additionally, the utilisation of the drizzle technique was also explored to enhance the resolution. The first methodology, exposition fusion, involves merging multiple exposures of the same target, each taken with slightly different settings, to produce a composite image with improved resolution and clarity. By combining these exposures, this method highlights the features of each individual frame, attributing different weights to pixels to be combined to yield a final image. The second technique examined is lucky imaging, which aims to exploit the moments of exceptional atmospheric stability to capture a sequence of rapidly acquired short exposures. Through statistical analysis, the best-quality frames are identified and subsequently aligned and combined to yield a high-resolution image. This method leverages the fortuitous instances of minimal atmospheric turbulence to overcome the limitations posed by atmospheric conditions, ultimately yielding sharper and more detailed images. In pursuit of superior results, a combination of the aforementioned methods was also explored. By integrating elements from both exposition fusion and lucky imaging, this hybrid approach aims to extract the best features of each technique, offering the potential for further enhancement in resolution and image quality. Finally, the drizzle technique was investigated as a means to further enhance resolution. Drizzle employs a pixel-reconstruction algorithm that redistributes the light gathered by each pixel over multiple adjacent pixels, effectively increasing the overall resolution. This method harnesses the potential of sub-pixel information, resulting in finer details and improved sharpness in the final image.

Once the telescope images were obtained using these methodologies, a conventional image stitching algorithm was subsequently employed to merge the images captured by the four telescopes, ultimately generating a master image.

Evaluation of the quality and performance of the proposed methods.

In conclusion, the analysis of both single telescope super-resolution and multi-telescope image stitching methodologies provides valuable insights into their effectiveness and limitations in improving the resolution and quality of astronomical images.

In terms of single telescope super-resolution, the various methods showcased unique characteristics and varying degrees of success in mitigating atmospheric disturbances. The baseline method of averaging yielded an enhancement in resolution but still exhibited blurriness around the stars. Exposition fusion refined star definition but resulted in diminished Gaussian characteristics. Simple lucky imaging showed improved resolution and reduced blurring, while weighted lucky imaging further increased resolution and reduced blurriness. However, the most remarkable outcomes were achieved with the implementation of the drizzle algorithm, which significantly enhanced resolution, produced well-defined stars, and minimised haziness. Therefore, the drizzle algorithm emerges as the most effective method in improving the resolution and quality of astronomical images among the analysed methodologies.

Regarding multi-telescope image stitching, the results showed varying degrees of success in enhancing the quality and definition of the final stitched images. The averaging (benchmark) technique improved star definition but introduced increased noise. Exposition fusion enhanced resolution and visibility but caused distortion in the main stars. Simple lucky imaging reduced blurring and mitigated atmospheric effects. Weighted lucky imaging provided enhanced definition and reduced blur in mid to better-quality observations, although it was less consistent in lower-quality observations and introduced more noise. The drizzle algorithm showcased remarkable advancements, reducing haziness and improving resolution consistently. Based on the conclusive master images and the analysed graphs, it is evident that the images with the poorest of qualities have significantly decreased performances. This is due to the poorly defined features, whereas both feature detection and matching tasks become less robust, which are employed in all shift-and-add and multi-telescope image stitching operations.

In conclusion, the drizzle algorithm emerges as the most effective method in single telescope super-resolution, producing remarkable outcomes in terms of resolution enhancement, star definition, and haziness reduction. In multi-telescope image stitching, while other techniques showed improvements in certain aspects, the drizzle algorithm outperformed them in terms of image enhancement and consistency. However, it is important to consider that the performance of the methods may vary depending on the quality of the observations.

6.2 Future Work

In the course of this dissertation, numerous ideas were thoroughly considered, although not all of them were implemented or tested. Commencing with object identification, it is imperative to emphasise the utmost significance of accurately aligning the centroid of the stars during the correction of atmospheric effects in images. To achieve this, a preliminary step of star identification and centroid determination becomes indispensable. Attaining a more precise acquisition of centroids will lead to improved image alignment, consequently resulting in more robust outcomes.

One point made when addressing the results in Chapter 5 is that "due to the absence of a technique to eliminate defective pixels and other artefacts, such as reflections, in the acquisition camera, the resultant master image inevitably contains a discernible level of noise stemming from the combined noise of all the telescopes involved.". Based on the previous statement, another future development to be done is the reduction of these artefacts. In the case of broken pixels, one could acquire a mapping of broken pixels and other detector noise by performing an observation in total darkness for all telescopes and filtering this map in a pre-processing phase for each frame. As for the random reflections, a more intricate solution is necessary and warrants further investigation.

Another prospective avenue for future development entails the exploration and evaluation of diverse image fusion algorithms, such as the Laplacian Pyramid or the Wavelet transform. These algorithms hold significant promise within the context of blending information from disparate frames captured by the same telescope or images obtained from different telescopes. By leveraging these algorithms, the fusion process can effectively enhance the overall quality and comprehensiveness of the captured astronomical data, thereby offering valuable insights into celestial phenomena.

Furthermore, as previously alluded to, in the event that these methodologies fail to yield the desired results, the field of machine learning presents viable alternatives for both multi-frame super-resolution and multi-telescope image stitching. The utilisation of machine learning techniques proves advantageous due to their ability to leverage the inherent patterns and relationships in astronomical data. By employing advanced algorithms and models, it becomes possible to reconstruct high-resolution images from low-resolution inputs and seamlessly stitch together images captured by multiple telescopes. These approaches hold great potential for enhancing the overall accuracy, resolution, and detail of astronomical imagery.

Appendix A

Appendix

A.1 Links for Repositories

All the code and results are stored in GitHub:

- https://github.com/Francisco-Sengo/dissertation

A.2 Software and Python libraries employed

Software:

PyCharm : PyCharm is an Integrated Development Environment (IDE) specifically designed for Python development. It was used for the development of the proposed methodologies.

Overleaf : Overleaf is an online collaborative Latex platform for writing and editing documents. It was used for every document writing task.

GitHub : GitHub is a web-based platform that provides version control and collaboration tools for software development. It provides a centralised platform for both student and advisor to access the code, as well as version control for the developed code

Google Drive : Google Drive is a cloud-based storage and file-sharing platform offered by Google. It was used to store meeting presentations, as well as other documents pertaining this dissertation.

Zoom : Zoom is a popular video conferencing and online meeting platform. All the meetings between student and advisors took place using this software.

Python Libraries:

NumPy : A powerful library for numerical computations in Python, providing efficient array operations and mathematical functions.

OpenCV : OpenCV is a popular open-source computer vision and image processing library.

Astropy : A versatile library for astronomy-related computations, providing tools for handling astronomical data, units, coordinates, and more.

Matplotlib : A popular plotting library in Python, enabling the creation of various types of plots, charts, and visualisations.

Photutils : An astropy-affiliated library that offers tools for detecting and analysing astronomical sources in images.

Math : A built-in Python library that provides fundamental mathematical functions and operations.

os : A module that provides a way to interact with the operating system, allowing you to perform tasks such as file and directory manipulation.

SciPy : A comprehensive scientific computing library in Python, offering a wide range of functionality, including numerical integration, optimisation, signal processing, and more.

drizzle : A library for creating high-quality, distortion-corrected mosaics from multiple astronomical images, often used in the field of astrophotography.

References

[1] Karishma C Bhataria and Bhumika K Shah. A review of image fusion techniques. pages 114–123, 2018.

[2] Hui Kong, Hatice Cinar Akakin, and Sanjay E. Sarma. A generalized laplacian of gaussian filter for blob detection and its applications. *IEEE Transactions on Cybernetics*, 43:1719–1733, 12 2013.

[3] Hassan Amerehie, Rouhollah Dianat, and Farshid Keynia. A new method to improve the difference of gaussian feature detector, 2014.

[4] Gang Wang, Carlos Lopez-Molina, and Bernard De Baets. Automated blob detection using iterative laplacian of gaussian filtering and unilateral second-order gaussian kernels. *Digital Signal Processing: A Review Journal*, 96, 1 2020.

[5] Yongju Cho, Dojin Kim, Saleh Saeed, Muhammad Umer Kakli, Soon Heung Jung, Jeongil Seo, and Unsang Park. Keypoint detection using higher order laplacian of gaussian. *IEEE Access*, 8:10416–10425, 2020.

[6] Monika Bansal, Munish Kumar, and Manish Kumar. 2d object recognition: a comparative analysis of sift, surf and orb feature descriptors. *Multimedia Tools and Applications*, 80:18839–18857, 5 2021.

[7] Yali Li, Shengjin Wang, Qi Tian, and Xiaoqing Ding. A survey of recent advances in visual feature detection. *Neurocomputing*, 149:736–751, 2 2015.

[8] Wei Lyu, Zhong Zhou', Lang Chen, and Vi Zhou. A survey on image and video stitching, 2019.

[9] Surbhi Gupta, Munish Kumar, and Anupam Garg. Improved object recognition results using sift and orb feature detector. *Multimedia Tools and Applications*, 78:34157–34171, 12 2019.

[10] MIT. 6.036 introduction to machine learning - mit canvas, notes. Chapters 8-9, 2021. Accessed in November 2022.

[11] Athanasios Voulodimos, Nikolaos Doulamis, Anastasios Doulamis, and Eftychios Protopapadakis. Deep learning for computer vision: A brief review, 2018.

[12] Lang Nie, Chunyu Lin, Kang Liao, Meiqin Liu, and Yao Zhao. A view-free image stitching network based on global homography. *Journal of Visual Communication and Image Representation*, 73, 11 2020.

[13] Laith Alzubaidi, Jinglan Zhang, Amjad J. Humaidi, Ayad Al-Dujaili, Ye Duan, Omran Al-Shamma, J. Santamaría, Mohammed A. Fadhel, Muthana Al-Amidie, and Laith Farhan. Review of deep learning: concepts, cnn architectures, challenges, applications, future directions. *Journal of Big Data*, 8, 12 2021.

[14] Elan Dubrofsky. Homography estimation. *Diplomoà pràce. Vancouver: Univerzita Britskà Kolumbie*, 5, 2009.

[15] Daniel DeTone, Tomasz Malisiewicz, and Andrew Rabinovich. Deep image homography estimation. 6 2016.

[16] Lang Nie, Chunyu Lin, Kang Liao, and Yao Zhao. Learning edge-preserved image stitching from multi-scale deep homography. *Neurocomputing*, 491:533–543, 6 2022.

[17] Youyong Zhou, Lingjie Yu, Chao Zhi, Chuwen Huang, Shuai Wang, Mengqiu Zhu, Zhenxia Ke, Zhongyuan Gao, Yuming Zhang, and Sida Fu. A survey of multi-focus image fusion methods, 6 2022.

[18] Yu Liu, Lei Wang, Juan Cheng, Chang Li, and Xun Chen. Multi-focus image fusion: A survey of the state of the art. *Information Fusion*, 64:71–91, 12 2020.

[19] Shutao Li, Xudong Kang, Leyuan Fang, Jianwen Hu, and Haitao Yin. Pixel-level image fusion: A survey of the state of the art. *Information Fusion*, 33:100–112, 1 2017.

[20] Chao Zuo, Jiasong Sun, Jiaji Li, Anand Asundi, and Qian Chen. Wide-field high-resolution 3d microscopy with fourier ptychographic diffraction tomography. *Optics and Lasers in Engineering*, 128, 5 2020.

[21] Wan-Chi Siu and Kwok-Wai Hung. Review of image interpolation and super-resolution. pages 1–10, 2012.

[22] Richard Davies and Markus Kasper. Adaptive optics for astronomy, 9 2012.

[23] Jing Tian and Kai Kuang Ma. A survey on super-resolution imaging. *Signal, Image and Video Processing*, 5:329–342, 9 2011.

[24] Kamal Nasrollahi and Thomas B. Moeslund. Super-resolution: A comprehensive survey. *Machine Vision and Applications*, 25:1423–1468, 2014.

[25] Craig Mackay. High-efficiency lucky imaging. *Monthly Notices of the Royal Astronomical Society*, 432:702–710, 2013.

[26] Law, N. M., Mackay, C. D., and Baldwin, J. E. Lucky imaging: high angular resolution imaging in the visible from the ground. *A&A*, 446(2):739–745, 2006.

[27] Jin Liang Wang, Bin Hua Li, and Xi Liang Zhang. A novel hybrid algorithm for lucky imaging. *Research in Astronomy and Astrophysics*, 21, 5 2021.

[28] A. S. Fruchter and R. N. Hook. Drizzle: A method for the linear reconstruction of undersampled images. *Publications of the Astronomical Society of the Pacific*, 114(792):144–152, feb 2002.

[29] S. L. Hoffmann, J. Mack, and et al. *The DrizzlePac Handbook*. STScI, Baltimore, 2021.

[30] Goutam Bhat, Martin Danelljan, Luc Van Gool, and Radu Timofte. Deep burst super-resolution. 1 2021.

[31] Deqing Sun, Xiaodong Yang, Ming-Yu Liu, and Jan Kautz. Pwc-net: Cnns for optical flow using pyramid, warping, and cost volume. *CoRR*, abs/1709.02371, 2017.

[32] Michel Deudon, Alfredo Kalaitzis, Israel Goytom, Md Rifat Arefin, Zhichao Lin, Kris Sankaran, Vincent Michalski, Samira E. Kahou, Julien Cornebise, and Yoshua Bengio. Highres-net: Recursive fusion for multi-frame super-resolution of satellite imagery. 2 2020.

[33] R. Abuter, M. Accardo, A. Amorim, N. Anugu, G. Ávila, N. Azouaoui, M. Benisty, J. P. Berger, N. Blind, H. Bonnet, P. Bourget, W. Brandner, R. Brast, A. Buron, L. Burtscher, F. Cassaing, F. Chapron, E. Choquet, Y. Clénet, C. Collin, V. Coudé Du Foresto, W. De Wit, P. T. De Zeeuw, C. Deen, F. Delplancke-Ströbele, R. Dembet, F. Derie, J. Dexter, G. Duvert, M. Ebert, A. Eckart, F. Eisenhauer, M. Esselborn, P. Fédou, G. Finger, P. Garcia, C. E. Garcia Dabo, R. Garcia Lopez, E. Gendron, R. Genzel, S. Gillessen, F. Gonte, P. Gordo, M. Grould, U. Grözinger, S. Guieu, P. Haguenauer, O. Hans, X. Haubois, M. Haug, F. Haussmann, Th Henning, S. Hippler, M. Horrobin, A. Huber, Z. Hubert, N. Hubin, C. A. Hummel, G. Jakob, A. Janssen, L. Jochum, L. Jocou, A. Kaufer, S. Kellner, S. Kendrew, L. Kern, P. Kervella, M. Kiekebusch, R. Klein, Y. Kok, J. Kolb, M. Kulas, S. Lacour, V. Lapeyrère, B. Lazareff, J. B. Le Bouquin, P. Lèna, R. Lenzen, S. Lévêque, M. Lippa, Y. Magnard, L. Mehrgan, M. Mellein, A. Mérand, J. Moreno-Ventas, T. Moulin, E. Müller, F. Müller, U. Neumann, S. Oberti, T. Ott, L. Pallanca, J. Panduro, L. Pasquini, T. Paumard, I. Percheron, K. Perraut, G. Perrin, A. Pflüger, O. Pfuhl, T. Phan Duc, P. M. Plewa, D. Popovic, S. Rabien, A. Ramírez, J. Ramos, C. Rau, M. Riquelme, R. R. Rohloff, G. Rousset, J. Sanchez-Bermudez, S. Scheithauer, M. Schöller, N. Schuhler, J. Spyromilio, C. Straubmeier, E. Sturm, M. Suarez, K. R.W. Tristram, N. Ventura, F. Vincent, I. Waisberg, I. Wank, J. Weber, E. Wieprecht, M. Wiest, E. Wiezorrek, M. Wittkowski, J. Woillez, B. Wolff, S. Yazici, D. Ziegler, and G. Zins. First light for gravity: Phase referencing optical interferometry for the very large telescope interferometer. *Astronomy and Astrophysics*, 602, 6 2017.

[34] European Southern Observatory. GRAVITY. `https://www.eso.org/public/teles-instr/paranal-observatory/vlt/vlt-instr/gravity/`, 2015. [Online; accessed November-2022].

[35] European Southern Observatory. Gravity user manual, 02 2016.

[36] Josedaniel Ponz, R. Thompson, and J. Munoz. The fits image extension. *Astronomy and Astrophysics Supplement Series*, 105:53–55, 04 1994.

[37] Robert D. Fiete. Modeling the imaging chain of digital cameras (spie press, 2011), 2011.

[38] Ian S. McLean. *Electronic imaging in astronomy : detectors and instrumentation*. Springer, 2008.

[39] J. N. Heasley. Point-spread function fitting photometry. *Precision CCD Photometry*, 189:56, 1999.

[40] Michael C. Roggemann, Byron M. Welsh, and Robert Q. Fugate. Improving the resolution of ground-based telescopes, Apr 1997.

[41] T. Stewart McKechnie. Atmospheric turbulence and the resolution limits of large ground-based telescopes, Nov 1992.

[42] P. Dierickx. Optical performance of large ground-based telescopes. *Journal of Modern Optics*, 39:569–588, 1992.

[43] Narsireddy Anugu, Paulo Garcia, Antonio Amorim, Erich Wiezorrek, Ekkehard Wieprecht, Frank Eisenhauer, Thomas Ott, Oliver Pfuhl, Paulo Gordo, Guy Perrin, Wolfgang Brandner, Christian Straubmeierfan, and Karine Perraut. Gravity acquisition camera: characterization results. 12 2020.

[44] M. Bigas, E. Cabruja, J. Forest, and J. Salvi. Review of cmos image sensors. *Microelectronics Journal*, 37:433–451, 5 2006.

[45] Eric R. Fossum and Donald B. Hondongwa. A review of the pinned photodiode for ccd and cmos image sensors. *IEEE Journal of the Electron Devices Society*, 2:33–43, 5 2014.

[46] Peter B. Stetson. Daophot: A computer program for crowded-field stellar photometry, mar 1987.

[47] M Annunziatella, S Cavuoti, and G Longo. Inside catalogs: A comparison of source extraction software, 2013.

[48] Larry Bradley, Brigitta Sipőcz, Thomas Robitaille, Erik Tollerud, Zé Vinícius, Christoph Deil, Kyle Barbary, Tom J Wilson, Ivo Busko, Axel Donath, Hans Moritz Günther, Mihai Cara, P. L. Lim, Sebastian Meßlinger, Simon Conseil, Azalee Bostroem, Michael Droettboom, E. M. Bray, Lars Andersen Bratholm, Geert Barentsen, Matt Craig, Shivangee Rathi, Sergio Pascual, Gabriel Perren, Iskren Y. Georgiev, Miguel de Val-Borro, Wolfgang Kerzendorf, Yoonsoo P. Bach, Bruno Quint, and Harrison Souchereau. astropy/photutils: 1.5.0, July 2022.

[49] Manolis Lourakis. A brief description of the levenberg-marquardt algorithm implemened by levmar, 01 2005.

[50] Astropy Collaboration, Adrian M. Price-Whelan, Pey Lian Lim, Nicholas Earl, Nathaniel Starkman, Larry Bradley, David L. Shupe, Aarya A. Patil, Lia Corrales, C. E. Brasseur, Maximilian Nöthe, Axel Donath, Erik Tollerud, Brett M. Morris, Adam Ginsburg, Eero Vaher, Benjamin A. Weaver, James Tocknell, William Jamieson, Marten H. van Kerkwijk, Thomas P. Robitaille, Bruce Merry, Matteo Bachetti, H. Moritz Günther, Thomas L. Aldcroft, Jaime A. Alvarado-Montes, Anne M. Archibald, Attila Bódi, Shreyas Bapat, Geert Barentsen, Juanjo Bazán, Manish Biswas, Médéric Boquien, D. J. Burke, Daria Cara, Mihai Cara, Kyle E. Conroy, Simon Conseil, Matthew W. Craig, Robert M. Cross, Kelle L. Cruz, Francesco D'Eugenio, Nadia Dencheva, Hadrien A. R. Devillepoix, Jörg P. Dietrich, Arthur Davis Eigenbrot, Thomas Erben, Leonardo Ferreira, Daniel Foreman-Mackey, Ryan Fox, Nabil Freij, Suyog Garg, Robel Geda, Lauren Glattly, Yash Gondhalekar, Karl D. Gordon, David Grant, Perry Greenfield, Austen M. Groener, Steve Guest, Sebastian Gurovich, Rasmus Handberg, Akeem Hart, Zac Hatfield-Dodds, Derek Homeier, Griffin Hosseinzadeh, Tim Jenness, Craig K. Jones, Prajwel Joseph, J. Bryce Kalmbach, Emir Karamehmetoglu, Mikołaj Kałuszyński, Michael S. P. Kelley, Nicholas Kern, Wolfgang E. Kerzendorf, Eric W. Koch, Shankar Kulumani, Antony Lee, Chun Ly, Zhiyuan Ma, Conor MacBride, Jakob M. Maljaars, Demitri Muna, N. A. Murphy, Henrik Norman, Richard O'Steen, Kyle A. Oman,

Camilla Pacifici, Sergio Pascual, J. Pascual-Granado, Rohit R. Patil, Gabriel I. Perren, Timothy E. Pickering, Tanuj Rastogi, Benjamin R. Roulston, Daniel F. Ryan, Eli S. Rykoff, Jose Sabater, Parikshit Sakurikar, Jesús Salgado, Aniket Sanghi, Nicholas Saunders, Volodymyr Savchenko, Ludwig Schwardt, Michael Seifert-Eckert, Albert Y. Shih, Anany Shrey Jain, Gyanendra Shukla, Jonathan Sick, Chris Simpson, Sudheesh Singanamalla, Leo P. Singer, Jaladh Singhal, Manodeep Sinha, Brigitta M. Sipőcz, Lee R. Spitler, David Stansby, Ole Streicher, Jani Šumak, John D. Swinbank, Dan S. Taranu, Nikita Tewary, Grant R. Tremblay, Miguel de Val-Borro, Samuel J. Van Kooten, Zlatan Vasović, Shresth Verma, José Vinícius de Miranda Cardoso, Peter K. G. Williams, Tom J. Wilson, Benjamin Winkel, W. M. Wood-Vasey, Rui Xue, Peter Yoachim, Chen Zhang, Andrea Zonca, and Astropy Project Contributors. The Astropy Project: Sustaining and Growing a Community-oriented Open-source Project and the Latest Major Release (v5.0) of the Core Package. , 935(2):167, August 2022.

[51] L. Kirkup and R. B. Frenkel. *An Introduction to Uncertainty in Measurement Using the GUM*. Cambridge University Press, 2007.

[52] Herman J. C. Berendsen. *A Student's Guide to Data and Error Analysis*. Cambridge University Press, 2011.

[53] Tom Mertens, Jan Kautz, and Frank Van Reeth. Exposure fusion, 10 2007.

[54] Wikipedia contributors. Lucky imaging. https://en.wikipedia.org/wiki/Lucky_imaging, 2023. [Online; April, 2023].

[55] Space Telescope Science Institute. DrizzlePac: HST image combining software. GitHub repository, Month Year. Accessed: March, 2023 [Online]. Available: https://github.com/spacetelescope/drizzle.